Aerodynamics Analysis of Small Horizontal Axis Wind Turbine Blades by Using 2D and 3D CFD Modelling

by

Han Cao

Thesis submitted to the University of the Central Lancashire in partial fulfilment of the requirements for the degree of

MSc (by Research)

May 2011

The work presented in this thesis was carried out in the School of Computing, Engineering and Physical Sciences at the University of Central Lancashire, Preston, England

Student Declaration

Concurrent registration for two or more academic awards

I declare that while registered as a candidate for the research degree, I have not been a registered candidate or enrolled student for another award of the University or other academic or professional institution

_____

Material submitted for another award

I declare that no material contained in the thesis has been used in any other submission for an academic award and is solely my own work

_____

Collaboration

Where a candidate's research programme is part of a collaborative project, the thesis must indicate in addition clearly the candidate's individual contribution and the extent of the collaboration. Please state below:

Signature of Candidate _____

Type of Award MSc by research_____

School School of Computing, Engineering and Physical Sciences

II

Contents

List of Figures

VI

List of Tables

Symbol

AoA   Angle of attack

AR   Aspect ratio

α   Axial induction factor

α'   Angular induction factor

c   Chord length   [m]

ρ   Fluid density   [kg/m^3]

C_L Lift coefficient

C_D Drag coefficient

C_M Moment coefficient

C_P Power coefficient

C_T Thrust coefficient

D Drag   [N]

D_0 Wind turbine diameter   [m]

D_x Wake diameter on the downwind horizontal distance between the wind turbines   [m]

F Force   [N]

F_L Lift force   [N]

F_D Drag force   [N]

k   Decay constant

L   Characteristic length   [m]

L Lift   [N]

Ma   Mach number

M Moment   [Nm]

n   Rotational speed   [rev/min]

P   Power   [kW]

Q   Torque   [n]

R   Rotor blade radius   [m]

Re   Reynolds number

S   Area of rotor blade   [m^2]

T Thrust   [N]

u_c Sound speed   [m/s]

V_∞ Velocity at infinity   [m/s]

V_0	Far field wind speed	[m/s]
V	Velocity of fluid	[m/s]
v_s	Speed of object	[m/s]
x	Downwind horizontal distance between the wind turbine	[m]
ω, Ω	Angular velocity	[rad/s]
r	Local radius	[m]
λ	Tip speed ratio	
ν	Kinematic viscosity	[m^2/s]
μ	Dynamic viscosity	[kg/m·s]
β	Initial wake expansion	
ϕ	Blockage ratio	

Acknowledgements

Firstly, I would like to thank Professor Xiongwei Liu, my Director of Studies, for his consistent support and guidance through all stages of this research project, to which he has generously devoted much time and effort.

I would like to thank my second supervisors Dr. Justin Whitty who generously devoted much time to reading the manuscript, and who made many valuable suggestions for its improvement.

I would like to thank all my friends and family, for their faithful advice, guidance, and love during my time of studying.

Abstract

Wind power is one of the most important sources of renewable energy. Wind-turbines extract kinetic energy from the wind. Currently much research has concentrated on improving the aerodynamic performance of wind turbine blade through wind tunnel testing and theoretical studies. These efforts are much time consuming and need expensive laboratory resources. However, wind turbine simulation through Computational Fluid Dynamics (CFD) software offers inexpensive solutions to aerodynamic blade analysis problem. In this study, two-dimensional aerofoil (i.e. DU-93 and NREL-S809) CFD models are presented using ANSYS-FLUENT software. Using the Spalart-Allmaras turbulent viscosity, the dimensionless lift, drag and pitching moment coefficients were calculated for wind-turbine blade at different angles of attack. These CFD model values we then validated using published calibrated lift and drag coefficients evident in the literature. Optimum values of these coefficients as well as a critical angle were found from polar curves of lift, drag and moment modelling data. These data were exploited in order to select the aerofoil with best aerodynamic performance for basis of a three-decisional model analogue. Thereafter a three-dimensional CFD model of small horizontal axis wind-turbine was produced. The numerical solution was carried out by simultaneously solving the three-dimensional continuity, momentum and the Naveir-Stokes equations in a rotating reference frame using a standard non-linear k-ω solver so that the rotational effect can be studied. These three-dimensional models were used for predicting the performance of a small horizontal axis wind turbine. Moreover, the analysis of wake effect and aerodynamic noise can be carried out when the rotational effect was simulated.

Chapter 1   Introduction

1.1 Background

Wind energy is an abundant resource in comparison with other renewable resources. Moreover, unlike the solar energy, the utilization could not be affected by the climate and weather. Wind turbine was invented by engineers in order to extract energy from the wind. Because the energy in the wind is converted to electric energy, the machine is also called wind generator. Figure 1-1 shows the growth rate of wind generator capacities, which has increased significantly in the last ten years. The total installed capacity of wind power generators was 159,213 MW at the end of 2009 (World Wind Energy Report 2009).

Figure 1-1 World total installed capacity (World Wind Energy Report 2009, p.5)

A wind turbine consists of several main parts, i.e. the rotor, generator, driven chain, control system and so on. The rotor is driven by the wind and rotates at predefined speed in terms of the wind speed, so that the generator can produce electric energy output under the regulation of the control system. In order to extract the maximum kinetic energy from wind, researchers put much efforts on the design of effective blade geometry. In the early stage, the aerofoils of helicopters were used for wind turbine blade design, but now, many specialized aerofoils have been invented and used for wind turbine

blade design. Moreover, a rotor blade may have different aerofoils in different sections in order to improve the efficiency, so the modern blades are more complicated and efficient comparing to early wind turbine blades.

In the early stage, the research on wind turbine blade design was limited on theoretical study, field testing and wind tunnel testing which need a lot of efforts and resources. Due to the development of computer aided design codes, they provide another way to design and analyse the wind turbine blades. Aerodynamic performance of wind turbine blades can be analysed using computational fluid dynamics (CFD), which is one of the branches of fluid mechanics that uses numerical methods and algorithms to solve and analyze problems of fluid flows. Meanwhile, finite element method (FEM) can be used for the blade structure analysis. Comparing to traditional theoretical and experimental methods, numerical method saves money and time for the performance analysis and optimal design of wind turbine blades.

1.2 Aims & Objectives

Aims

The research aims to evaluate the aerodynamic performance of variable-speed fixed-pitch horizontal-axis wind turbine blades through two and three dimensional computational fluid dynamics (CFD) analysis.

Objectives

The objectives of the research are to establish 2D and 3D CFD models of wind turbine blade and rotor, so as

- To analyse the aerodynamic performance of different aerofoils;
- To predict wind turbine power output at different wind speeds;
- To compare different blade roots and tips design;
- To analyse the wake effect of the rotor under operation;
- To predict the noise of wind turbine under operation.

1.3 Overview of this report

A comprehensive study of the aerofoil behaviour is implemented using 2D modelling. Unlike another aerodynamic device, wind turbine relies on the stall property to limit the power output (Carcangiu, 2008, p.4) at high wind speed, so it is necessary to know when and how the stall condition happens.

In 3D modelling, the torque and thrust force acting on the blade can be calculated using CFD packages. At different wind speeds, the optimum rotational speeds can be estimated in order to maintain either maximum power point tracking at low wind speed or constant power output at high wind speed. Meanwhile, by taking into account of the rotational effect, wake analysis and aerodynamic noise prediction can be implemented.

This dissertation consists of five chapters. The aims and objectives are introduced in Chapter 1. In Chapter 2, the theories of computational fluid dynamics and wind turbine aerodynamics are introduced. Simulation methods are introduced in Chapter 3, which includes the two- and three-dimensional modelling. In this chapter, different modelling approaches are compared so as to improve the simulation accuracy. Two- and three-dimensional simulation results are analysed in Chapter 4, aerodynamic performance of different aerofoils are estimated in two-dimensional results section and a comprehensive analysis regarding wind turbine rotor performance is addressed in three-dimensional results section. The conclusions and future work are summarized in Chapter 5.

Chapter 2   Literature Review

In this chapter, some basic theories of wind turbine aerodynamics and computational fluid dynamics are introduced. Moreover, the purposes and methods for wind turbine simulation are discussed.

2.1 Historical development of wind turbine

Wind turbine is a device, which converts the kinetic energy from the wind to electric energy via a mechanical rotor, a drive train and a generator. One of the earliest wind turbines was designed by Poul La Cour, who was a professor at an adult education centre in Denmark in 1891 (Figure 2-1). Nowadays, Enercon E-126, the world biggest wind turbine can generate up to 7 Megawatts of power under the rated wind speed. This capacity can provide the daily electricity for more than 4500 homes. Following the technology development of modern wind turbines, they can now be mounted either on the ground or on the seabed. A giant offshore wind turbine of 10 megawatts will be installed in 2011 by Enova SF in Norway. As the depletion of coal and fossil oil, wind energy will play a more and more important role in this century.
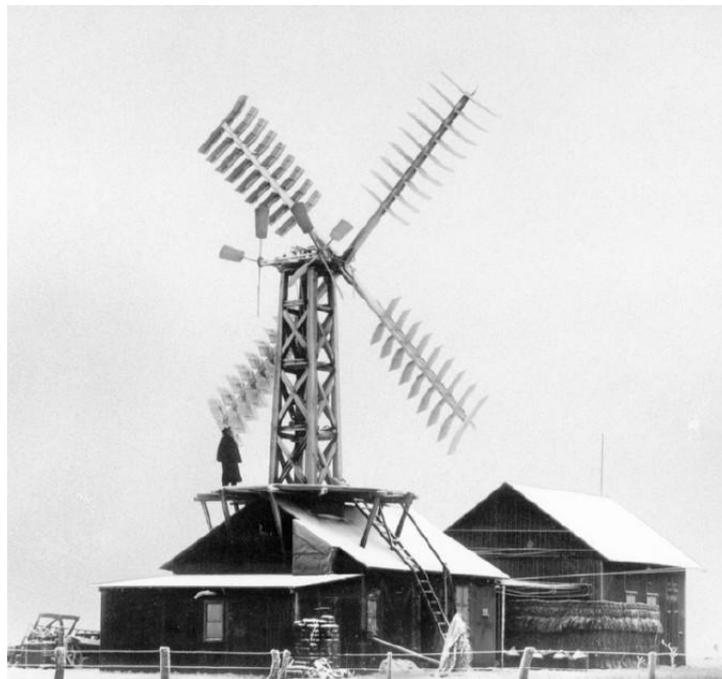
Figure 2-1 Pou La Cour's first electricity producing wind turbine in 1891 in Askov, Denmark (Golding, 1977)

2.2 Wind turbine aerodynamics

According to the different rotational orientations, wind turbines can be categorized as vertical-axis or horizontal-axis. The advantages of vertical-axis wind turbine (VAWT) are:

1. Simple structure: VAWT can work without yaw system and most of them have a blade with constant chord and no twist (Manwell, et al., 2002, p.259), which is easy to construct.
2. Easy to install: because the drive trains (gear box, brake and generator) can be located relative to the ground.

Comparing to horizontal-axis wind turbine (HAWT), stall control can only be used in VAWT as it is difficult to incorporate aerodynamics control such as variable pitch and aerodynamic brake, so the overall power efficiency is lower than HAWT.
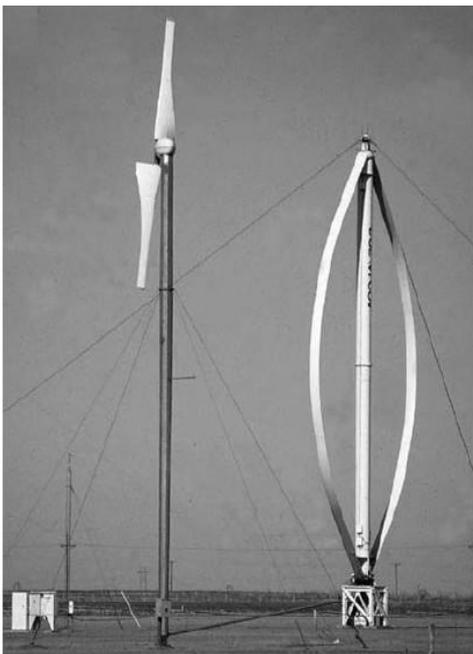
Figure 2-2 Vertical-axis wind turbine   **Figure 2-3 Horizontal-axis wind turbine**

2.2.1 Lift, drag and moment coefficients

In general, there are two forces and one moment that act upon an aerofoil; these being lift, drag and pitching moment. The definitions of those three forces are explained in this section.
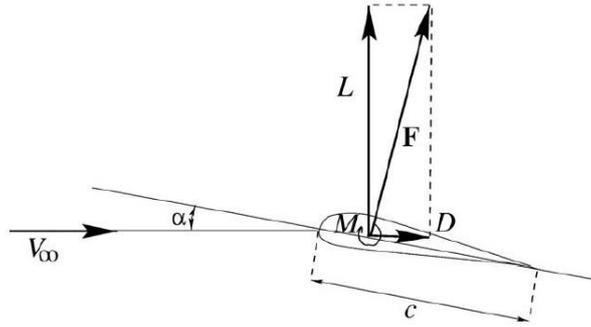
Figure 2-4 Definition of lift and drag ratio (Hansen, 2008, p. 8)

Lift is the force used to overcome gravity (Hansen, 2008, p. 8) and is defined to be perpendicular to direction of the oncoming airflow (Manwell, et al., 2002, p.96). It is formed as a consequence of the unequal pressure on the upper and lower airfoil surfaces. The drag force is defined as a force parallel to the direction of oncoming airflow. (Manwell, et al., 2002, p.96) The drag force is due both to viscous friction forces at the surface of the aerofoil and to unequal pressure on the airfoil surfaces facing toward and away from the oncoming flow. The lift is the force used to overcome gravity and the higher the lift the higher the mass that can be lifted off the ground. For an aerofoil, Hansen (2008, p.8) stated that the lift to drag ratio should be maximized. As a result, it can improve efficiency when wind turbine generates electricity. Lift and drag coefficients C_L and C_D are defined as follows.

Lift coefficient $\quad C_L = \dfrac{F_L}{1/2\rho V_0^2 c}$ $\qquad$ **(Equation 2-1)**

Drag coefficient $C_D = \dfrac{F_D}{1/2\rho V_0^2 c}$ $\qquad$ **(Equation 2-2)**

Where ρ is the air density and c is the length of the aerofoil, often denoted by the chord, unit for the lift and drag in Equations 2-1 and 2-2 is force per length (in N/m). To describe the forces completely, it is also necessary to know the pitching moment M. It has been found both experimentally and theoretically by NASA that, if the aerodynamic force is applied at a location ¼ chord back from the leading edge on most low speed airfoils, the magnitude of the aerodynamic pitching moment remains nearly constant with angle of

6

attack. In most aerofoil simulations, the pitching moment centre is set up at ¼ chord length to get an approximate value and the pitching moment coefficient is defined as follows.

Moment coefficient $C_M = \dfrac{M}{1/2\rho V_0^2 c^2}$ **(Equation 2-3)**

2.2.2 Tip speed ratio

The tip speed ratio is the ratio of the blade tip speed over wind speed. It is a significant parameter for wind turbine design and its definition is shown in Equation 2-4.

Definition of tip speed ratio $\lambda = \omega R / v_0$ **(Equation 2-4)**

ω is the angular velocity of the wind turbine rotor, R is radius of the rotor and v_0 is the wind speed. A higher tip speed ratio generally indicates a higher efficiency but is also related to higher noise levels. Generally a low speed wind turbine chooses value of tip speed ratio from 1 to 4 and a high speed wind turbine chooses its value from 5 to 9.

As a preliminary design consideration, the best range of tip speed ratios for a high speed turbine is around 7 (Burton, et al., 2001, p.207), which ensures that the wind turbine can run at near maximum power coefficient. The relationship between rotational speed and tip speed ratio is shown in Equation 2-5.

$$\lambda = \frac{2\pi n r}{60 V_0} \qquad \text{(Equation 2-5)}$$

Where n is the rotational speed of the rotor, r is the rotor radius and V_0 is the wind speed. For instance, if tip speed ratio is 8, the rotor radius is 9m and wind speed is 10m/s, then the rotational speed of the rotor should be 85rpm using Equation 2-6.

$$n = \frac{60 \lambda V_0}{2\pi r} \qquad \text{(Equation 2-6)}$$

Thus, an inverse relationship between the rotational speed and the blade span is presented in this equation. Due to the same tip speed ratio, a blade with a big span has a low rotational speed. What's more, taking into account of the structural design of blades, high rotational speed requires a highly

substantial structure, which cost too much to construct and induces enormous noise.

2.2.3 Betz limit
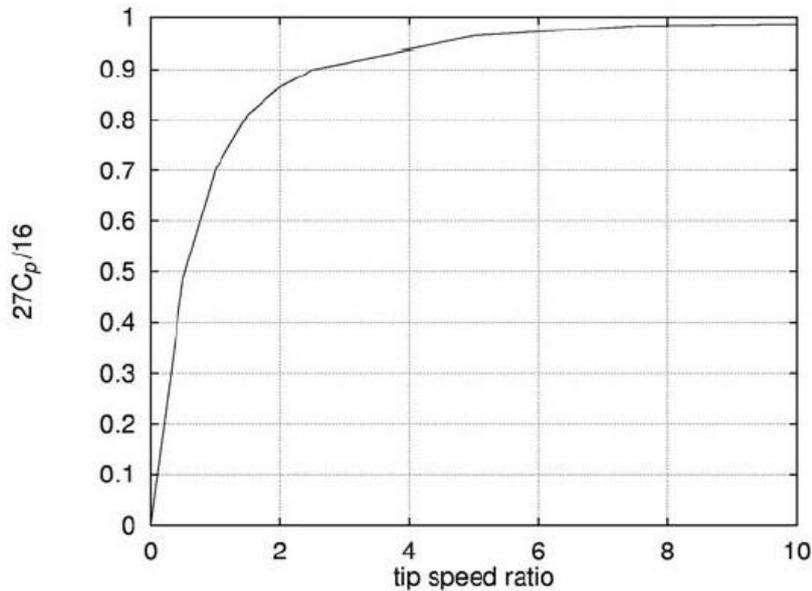
Figure 2-5 The efficiency of an optimum turbine with rotation (Hansen, 2008, p. 40)

The efficiency is defined as the ratio between power coefficient *Cp* and the Betz limit, Betz = 16/27 ≈ 0.593. This value was concluded by **Albert Betz** who was a German physicist in 1919, 0.593 is the maximum power efficiency of a wind turbine which converts the kinetic energy to mechanical energy, So efficiency $\eta = Cp / \dfrac{16}{27} = \dfrac{Cp \times 27}{16}$. Seeing from Figure 2-5, the power loss is big for a low tip speed ratio wind turbine, for instance, a running wind turbine can only achieve 85% efficiency when the tip speed ratio is 2. The system will become more and more efficient if the tip speed ratio is higher. When the tip speed ratio reaches to 6, the efficiency is approximate 96%. It indicates that wind turbines with high tip speed ratio can extract more kinetic energy from wind by comparing with low tip speed ratio wind turbines.

2.2.4 Number of blades

The number of blades greatly influences the HAWT performance. The most common formats are two-blade and three-blade machines. Some small

8

HAWTs may have more than 3 blades, and normally they are low speed wind turbines. Low speed machine operates with large torque. On the other hand, high speed wind turbines have only 2 or 3 blades can hence to achieve similar wind energy utilization with low driving torque.

2.2.5 Blade element momentum theory (BEM)

With this theory, it is possible to calculate the steady loads and also the thrust and power for different settings of wind speed, rotational speed and pitch angle. As shown in Figure 2-6, for illustration purpose, the blade is assumed to be divided into N sections or elements and the following assumptions are made:

1. Every element is independent; a variation in one element will not affect other elements.

2. The force from the blades is determined individually by the lift and drag of the airfoil shape of the blades.
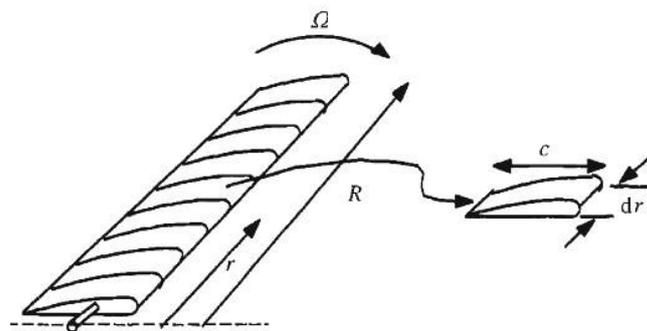
Figure 2-6 Schematic of blade elements; c, airfoil chord length; dr, radial length of element; r, rotor radius; Ω, angular velocity of rotor (Manwell, et al., 2002, p107)

In order to get good results when using BEM method, it is necessary to apply two important corrections below. (Carcangiu, 2008, p.16)

The first is called Prandtl's tip loss factor, which corrects the assumption of an infinite number of blades. The second correction is called Glauert's correction and is an empirical relation between the thrust coefficient C_T and the axial induction factor **a** when value is greater than approximately 0.3.

2.2.6 **Aerofoil Behavior**

Before introducing the aerofoil behavior, Mach number and Reynolds number need to be explained. Mach number is a ratio of speed of an object over sound and it is defined as:

$$Ma = \frac{v_s}{u_c}$$
(Equation 2-7)

Where *Ma* is mach number, v_s is object speed and u_c is sound speed. Subsonic is defined as $Mach \leq 1$, transonic is defined as $Mach = 1$, supersonic is defined as $Mach \geq 1$ and hypersonic is defined as $Mach \geq 5$.

The Reynolds number is a non-dimensional value and it is a ratio of inertial force to viscous force, defined as:

$$Re = \frac{\rho V^2 / L}{\mu V / L^2} = \frac{\rho V L}{\mu}$$
(Equation 2-8)

Aerofoil behaviour can be described into three flow regimes: the attached flow regime, the high lift/stall development regime and the flat plate/fully stalled regime (Burton, et al., 2001, p.101). In attached flow regime, flow is considered at the upper surface of aerofoil, in this situation, lift increases with the angle of attack. In high lift/stall development regime, the lift coefficient peaks as the airfoil becomes increasingly stalled. Stall occurs when the angle of attack exceeds a certain value (depending on the Reynolds number) and separation of the boundary layer on the upper surface takes place. It is indispensable to study the aerofoil behaviour: aerodynamic performances are different because of different geometry of aerofoil, and according to different aerofoil's behaviour, choosing an applicable aerofoil for wind turbine blade will improve the efficiency.

2.2.7 **Untwisted and twisted blade**

For some modern wind turbines, the blade tips are designed using a thin airfoil for high lift to drag ratio, and the root region is designed using a thick version of the same airfoil for structural support. The crucial factors for choosing airfoil are: maximum lift to drag ratio and low pitch moment. Figure 2-8 shows that: as one untwisted blade, the stall condition occurs from the spanwise station (r/R) is 16%. In order to increase the effective flow velocity at

the rotor blade from the blade root to the tip, it is better to twist blades (Hau, 2006, p.135). Note that in order to achieve the maximum lift and efficiency for some long blades, not only the chord length, thickness and twisted angle change, but also the shape of airfoil varies along the blade. Manufacturing difficulty needs to be taken into account as well. Previously, the most popular aerofoil of wind turbine blade was NACA4412 (Figure 2-7), since the lower surface of this aerofoil is flat which is easy to manufacture with glass fibre, although it does not have a good air performance. Nowadays, many practical aerofoils have been designed for different wind turbines such as NREL, DU and BE series.
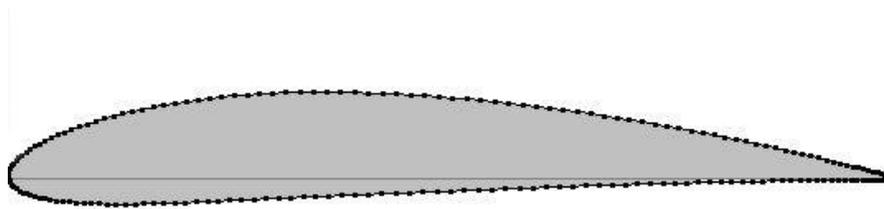
Figure 2-7 NACA4412 aerofoil cross section
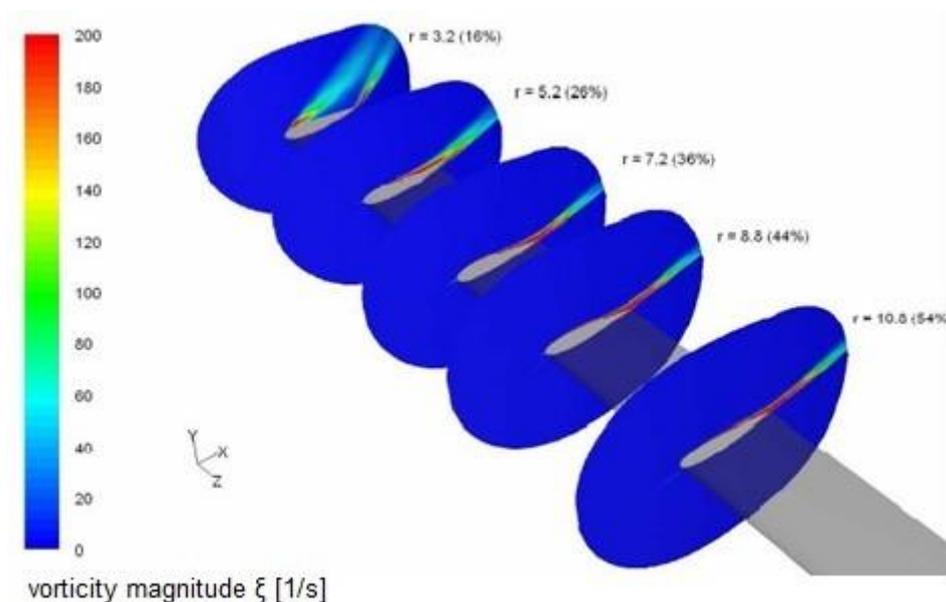
Figure 2-8 Contours of vorticity magnitude ξ [1/s] along blade span direction
(Carcangiu, 2008, p93)

2.2.8 **Aerodynamic power control**

Many small wind turbine designs using fixed pitch blades rely on power control via aerodynamic stall of the blades. Air separation is obvious under the

stall condition which leads to pressure difference between the upper and lower surface of an aerofoil to reduce. As a consequence, decrease in lift and an increase in drag. In a well designed wind turbine, the output power can be kept constant level even if the wind speed increases; this is called passive stall control. Commonly, passive stall control on HAWT produces too much power at high wind speeds which causes generator damage. In order to prevent wind turbine from destruction, the provision of aerodynamic brakes to limit overspeed are absolutely mandatory for rotors with fixed blades. Different types of aerodynamic brakes are shown below in Figure 2-9:

Tip brakes   Pitchable tips   Spoilers
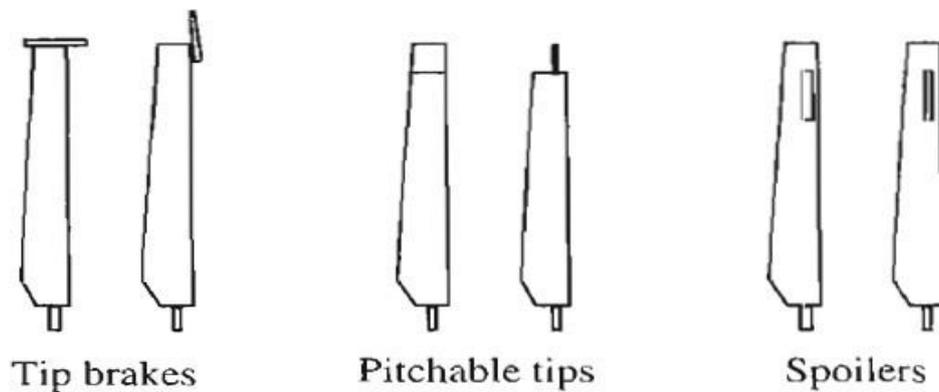
Figure 2-9 Different types of aerodynamic break (Manwell, et al., 2002, p333)

Recently, many large-scale wind turbines have used power control by rotor blade pitching. In principle, power control by changing the aerodynamic angle of attack of the rotor which can be achieved by two methods. The conventional approach is by adjusting the blade angle of attack to a smaller degree in order to reduce power output. Conversely, the power output is increased by increasing the angle of attack. The other way is to increase the blade pitch angle to a larger angle, up to the critical aerodynamic angle of attack, at which point the airflow separates at the surface of the rotor blade, thus limiting the aerodynamic input power.

When the optimum rotational speed is exceeded, the wind turbine with fixed pitch blades are used aerofoil stalls at a high angle of attack to reduce the tip speed ratio. Differently, Wind turbines with variable pitch blades can change the angle of attack by pitching blades which cause rotor aspect ratio to vary. The aspect ratio (AR) of wind turbine is defined as (Hau, 2006, p124):

$$AR = \frac{R^2}{S}$$

R is the radius of rotor blade and S is the area of rotor blade. The higher the AR is, the more the lift and drag of rotor blade will be created. (Hansen, 2008, p.95)

2.3 Computational fluid dynamics (CFD)

There are many commercial CFD softwares used in engineering, such as PHOENICS (it is the first commercial CFD software), STAR-CD, ANSYS FLUENT/CFX and so on. All CFD softwares have three main structures which are Pre-Processer, Solver and Post-Processor.

2.3.1 The principle theories relevant to CFD modelling

No matter what kind of CFD software is, the main processes of simulation are the same. Setting up governing equations is the precondition of CFD modelling; mass, momentum and energy conservation equation are the three basis governing equations. After that, Boundary conditions are decided as different flow conditions and a mesh is created. The purpose of meshing model is discretized equations and boundary conditions into a single grid. A cell is the basic element in structured and unstructured grid. The basic elements of two-dimensional unstructured grid are triangular and quadrilateral cell. Meanwhile, the rectangular cell is commonly used in structured grid. In three-dimensional simulation, tetrahedra and pentahedra cells are commonly used unstructured grid and hexahedra cell is used in structured grids. The mesh quality is a prerequisite for obtaining the reasonably physical solutions and it is a function of the skill of the simulation engineer. The more nodes resident in the mesh, the greater the computational time to solve the aerodynamic problem concerned, therefore creating an efficient mesh is indispensable. Three numerical methods can be used to discretize equations which are Finite Different Method (FDM), Finite Element Method (FEM) and Finite Volume Method (FVM). FVM is widely used in CFD software such as Fluent, CFX, PHOENICS and STAR-CD, to name just a few. Compared with

FDM, the advantages of the FVM and FEM are that they are easily formulated to allow for unstructured meshes and have a great flexibility so that can apply to a variety of geometries.

2.3.2 Turbulent models

In CFD software, wind turbines are simulated under the turbulent flows. Normally, the method of turbulent numerical simulation consists of two main parts, which are Direct Numerical Simulation (DNS) and Indirect Numerical Simulation (INS). Although DNS has a precise calculated result, but the whole range of spatial and temporal scales of the turbulence must be resolved which requires a very small time step size, hence this is not suitable for CFD simulation. There are three different types of simulated methods under the Indirect Numerical Simulation which are large eddy simulation (LES), Reynolds-averaged Navier-Stokes (RANS) and detached eddy simulation (DES). In order to simulate turbulent flows, theoretically, the computational domain should be big enough to contain the biggest eddy. Meanwhile, the mesh should be small enough to find out the smallest eddy. But the current grid was too coarse to catch the small eddies. Hence large eddy simulation (LES) is a technique which filters small eddies while conserving large energy eddies. This method requires a more refined mesh than RANS model, but a far coarser mesh than DNS solutions. The equation of Reynolds-averaged Navier-Stokes (RANS) is defined as:

$$\rho \frac{DU_i}{Dt} = \frac{\partial P}{\partial X_i} + \frac{\partial}{\partial X_i}\left[\mu\left(\frac{\partial U_i}{\partial x_j} + \frac{\partial U_j}{\partial x_i}\right) - \rho\overline{u_i'u_j'}\right] \quad \textbf{(Equation 2-9)}$$

It is the oldest and most common approach to turbulence modelling; the left hand side of the equation describe the change in mean momentum of fluid element and the right hand side of the equation is the assumption of mean body force and divergence stress. $\rho\overline{u_i'u_j'}$ is an unknown term and called Reynolds stresses, named after the person who proposed the equation (Sahini, 2004, p.47). The RANS equation is not closed due to the presence of stress term, so it requires a turbulence model to produce a closed system of solvable equation. The turbulence model contains one and two equations model. The famous one equation "Spalart-Allmaras" model and two equations

14

"standard k−ε" models are widely used in most CFD softwares. The transport equation of Spalart-Allmaras model can be described as:

$$\frac{\partial}{\partial t}(\rho \tilde{v}) + \frac{\partial}{\partial x_i}(\rho \tilde{v} u_i) = G_v + \frac{1}{\sigma \tilde{v}}\left[\frac{\partial}{\partial x_j}\left\{(\mu + \rho \tilde{v})\frac{\partial \tilde{v}}{\partial x_j}\right\} + C_{b2}\rho\left(\frac{\partial \tilde{v}}{\partial x_j}\right)^2\right] - Y_v + S_{\tilde{v}}$$ **Equation 2-10**

$\tilde{v}$ is the turbulent kinematic viscosity, G_v is the production of turbulent viscosity and Y_v is the destruction of turbulent viscosity. $\sigma \tilde{v}$ and C_{b2} are constants and v is the molecular kinematic viscosity. $S_{\tilde{v}}$ is a user-defined source term (Fluent 6.3 User's Guide 12.3.2, 2006).

In k−ε model, the first transported variable is turbulent kinetic energy, k. The second transported variable in this model is the turbulent dissiation, ε. In standard k−ε model, the turbulent kinetic energy k can be described as:

$$\frac{\partial}{\partial t}(\rho k) + \frac{\partial}{\partial x_i}(\rho k u_i) = \frac{\partial}{\partial x_j}\left[\left(\mu + \frac{\mu_t}{\sigma_k}\right)\frac{\partial k}{\partial x_j}\right] + P_k + P_b - \rho \varepsilon - Y_M + S_k$$ **Equation 2-11**

The turbulent dissiation ε can be described as:

$$\frac{\partial}{\partial t}(\rho \varepsilon) + \frac{\partial}{\partial x_i}(\rho \varepsilon u_i) = \frac{\partial}{\partial x_i}\left[\left(\mu + \frac{\mu_t}{\sigma_\varepsilon}\right)\frac{\partial \varepsilon}{\partial x_j}\right] + C_{1\varepsilon}\frac{\varepsilon}{k}(G_k + C_{3\varepsilon}G_b) - C_{2\varepsilon}\rho\frac{\varepsilon^2}{k} + S_\varepsilon$$ **Equation 2-12**

The eddy viscosity is given by:

$$\mu_t = \rho C_\mu \frac{k^2}{\varepsilon}$$ **Equation 2-13**

The production of the turbulence kinetic enery is given by:

$$P_k = \mu_t S^2$$ **Equation 2-14**

In these equations, G_k and G_b are the generation of turbulence kinetic energy. Y_M is the dilatation dissipation term which is the contribution of the fluctuating dilatation in compressible turbulence to the overall dissipation rate (Fluent 6.3 User's Guide 12.4.1, 2006). The empirical constants $C_{1\varepsilon}$=1.44, $C_{2\varepsilon}$=1.92, C_μ =0.09, σ_ε=1.3 and σ_k=1.0. In ANSYS-Fluent, S_ε and S_k are the user-defined terms.

Hybird LES/RANS approaches, such as detached eddy simulation (DES), (Carcangiu, 2008) represent an attractive compromise between computing

costs and accuracy. The DES technique has recently been applied on the NREL Phase VI wind turbine blade under parked conditions. (Sorensen, et al., 2004)

2.3.3 **Solutions methods**

- Standard k−ε model: it has a nice stability and precision for high Reynolds number turbulent flow but it is not suitable for some simulation with rotational effect.

- RNG k−ε model: it can used for low Reynolds number flow, as considering the rotational effect, the simulated accuracy will be enhanced in rapidly strain flow.

- Realizable k−ε model: it is more accurate for predicting the speeding rate of both planar and round jets but it will produces non-physical turbulent viscosities when the simulated model includes both rotating and stationary fluid zone (Fluent 6.3 User's Guide 12.4, 2006).

- Standard k-ω model: it contains the low-Reynolds-number effects, compressibility and shear flow spreading. It has a good agreement with measurements with problems of far wake, mixing layers and plane, round, and radial jets.

- Shear-stress transport (SST) k-ω model: because it absorbs both the property of good accuracy in the near-wall region of standard k-ω model and nice precision in the far field region of k−ε model (Fluent 6.3 User's Guide 12.5, 2006), it is more accurate and reliable for a wider class flow than the standard k-ω model.

- Reynolds stress model: Abandoning the eddy-viscosity hypothesis, the Reynolds stress model (RSM) calculates the Reynolds stresses directly. Theatrically, it is much more accurate than k−ε and k-ω model, but five additional transport equations in 2D flows and seven additional transport equations in 3D flows (Fluent 6.3 User's Guide 12.7, 2006) seize huge resources in computer and a long simulated time.

2.4 HAWT CFD modelling objectives

Nowadays, CFD modelling has been widely used in wind turbine analysis. In 2D modelling, it can be used to evaluate the lift, drag and moment value and estimate the separation point. Meanwhile, it can be used in 3D simulation to determine the design parameters and wind farm optimization.

1. Try to achieve an accurate lift, drag and momentum coefficient during aerofoil simulation is the one of the objectives. The Figure 2-10 shows a comparison between 2D DU 93-W-210 aerofoil numerical simulations and Delft university wind tunnel test. A reliable result can in fact replace the wind tunnel test and reduce the overall testing time needed. Figure 2-10 shows that CFD software has a nice precision under the angles of attack from -10° to 10°. Based on the reliable result, aerofoil can be simulated under a wide range of angles of attack (-20° to 90°), in order to observe the optimum and critical angle of attack.

   The critical angle of attack is defined as an angle which can produce maximum lift, above the critical angle of attack, a stall condition occurs as air flow becomes fully separated. This means that when angle of attack increases further, wind turbine blade will get into fully stalled regime. When wind turbine blades are working on the stall condition, noise will be increased significantly and wind turbine vibration may happen. It is valuable to investigate the critical angle of attack, because, in principle, change the blade pitch angle to the so-called critical aerodynamic angle of attack leads the aerofoil into fully stalled position so that limits the aerodynamic power output. The optimum angle of attack is where lift to drag ratio has the maximum value and it can be found by plotting the lift to drag ratio.
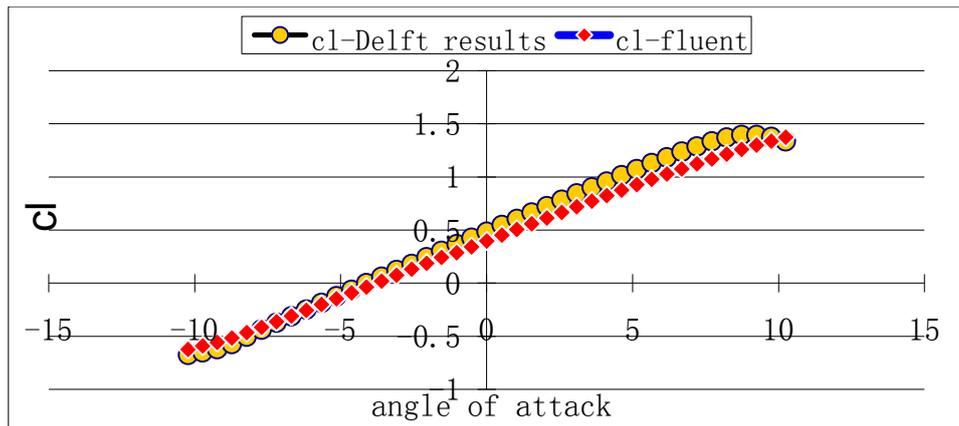
Figure 2-10 Lift coefficient of DU93 from -10° to 10°

2. Separation point is where the fluid passing over a body separates from the surface of the body. It is sometimes followed by reattachment of the flow. In ANSYS Fluent, the separation point can be found by observing where the wall shear stress vanishes. Stall will begin when the separation point has moved forward to the leading edge. The transition point is where boundary layer changes from laminar to turbulent. As speed and angle of attack increases, the upper surface transition point also tends to move forward. In order to capture the point along the chord where the transition changes from a laminar to a turbulent boundary layer in ANSYS-Fluent, the computational region can be split into laminar flow and turbulent flow domains. The disadvantage of this approach is that the accuracy of the simulation depends on one's ability to accurately guess the transition location and a new grid must be generated if someone wants to change the transition location.

3. In three-dimensional simulations, different blade and hub geometries can be simulated to evaluate which one has a highest power output. These parameters are of the utmost importance for engineers in order to improve the performance of wind turbine blades. Mechanical power is the most important parameter for performance evaluation and definition is shown in Equation 2-15:

$$p = \omega Q \quad \text{(Equation 2-15)}$$

In steady CFD simulations, a wind turbine has a unique rotational speed, so the torque can be calculated when simulated results converge. Therefore, the power can be calculated by using the equation above. Two approaches have been used in three-dimensional wind turbine simulations. One is full scale simulation which put wind turbine (neither the ground nor tower is included into the model) into a cylindrical computational domain (Carcangiu, 2008, p71). However, this method requires large memory inside the computer. In order to simulate models using personal computers, the 120 degrees periodicity of the rotor has been exploited with computational domain, it only allows to mesh the volume around a single blade. The remaining two blades were included in the computations using periodic boundary condition.

4. Onshore wind farms usually consist of a number of horizontal axis wind turbines which are mounted with a close space. Various models have been developed in the past to estimate the wake effect and optimize the sitting of a wind farm (Makridis & Chick, 2009). Computational Fluid Dynamics (CFD) has been a useful tool towards the understanding of wake behaviour on different terrains such as wind turbine mounted on plains and hills. By using CFD code to study the wake interaction, the optimum distance between adjacent wind turbines can be predicted in different terrains.

2.5 Fluid structure interaction (FSI)

In order to simulate blade rotational effect, rotational reference frame, sliding mesh and dynamic mesh technologies can be used in ANSYS-Fluent which is one of the most famous CFD commercial software. The rotational reference frame model is used in steady-state solution (FLUENT 6.3 User's Guide). For wind turbine simulation, it requires the rotational speed to remain constant. Sliding mesh model is used in unsteady-state simulation. Normally, it has been adopted to solve periodic problem such as rotation wake and flow separation, but this approach requires large memory and high performance CPU. As the dynamic mesh is based on the moving objects, it can automatically rebuild the mesh in the computational domain, hence can be

used to solve the unsteady-state problem and will seize a large number of computational resources. The precondition of solving fluid structure interaction problem is using dynamic mesh.

FSI is the interaction of some movable or deformable structures with an internal or surrounding fluid flow. It is the cutting edge of wind turbine simulation. Under the interaction of computational fluid dynamics (CFD) and computational structure dynamics (CSD), the rotor rotational speed, pressure distribution and dynamic stress distribution on the blade can be evaluated in a particular wind speed. Normally, ordinary CFD software can simulate wind turbine rotation in a steady condition which means the wind speed is constant and rotational speed needs to be set up manually, this method requires rotational speed to be adjusted with an applicable value, the wind speed and wind turbine rotational speed are both independent so that they could not affect each other. By using fluid structure interaction technology, wind turbine model starts to rotate if an appropriate moment of inertia is given under a specified wind speed. Wind speed affects the rotational speed and torque of the blades, which can give feedback to flow field simultaneously. The results are stable when the iterations of fluid dynamics and structure dynamics converge; the simulated result can be used in an aeroelastic analysis.

2.6 Issues in wind turbine simulation using CFD software

A confident result of aerofoil simulation was achieved in two dimensional simulations (section 2.2), but it was difficult to get a reliable results for three dimensional simulations. Initially, the air flow passing through a rotating HAWT blade is much more complicated than that of a 2D simulation because the changing angles of attack vary along the aerofoil span. Moreover, under high winds, stall of the system can take place from the root sections. There are also centrifugal forces along the blade due to rotor rotation. On the other hand, accuracy of simulation is affected because of the limitation of CFD software: firstly, no matter what kind of turbulent model is used, it is extremely hard to simulate the turbulence in physical reality. Additionally, a fine mesh is a prerequisite in order to simulate full scale wind turbines; which are very

memory restrictive inside the computer meaning the simulation cannot be carried out using personal computers with low configuration. In order to reduce the mesh size, normally, neither the tower nor the ground are included into the model. Finally, geometry of wind turbine blades is difficult to mesh with quality. Most wind turbine blade tips are designed using a thin airfoil for low induced drag and the root region is using a thick version for structural support, the size difference between tip and root leads to mesh scales difficult to control.

Chapter 3   Methods

Two-dimensional (2D) aerodynamic models and three-dimensional (3D) wind turbine models are explained in this chapter. Different modelling strategies are exploited in order to address the accuracy of the modelling presented in this and other chapters.

3.1 Two-dimensional aerofoils modelling

GAMBIT is the pre-processor of ANSYS-Fluent. A simulation model can be created in GAMBIT directly or imported from other CAD software packages, such as SolidWorks and Pro/Engineer®. In this section, aerofoils DU93-W-210 and NREL S809 are modelled.

3.1.1 DU93-W-210 modelling

Figure 3-1 depicts the profile of DU-93-W210 aerofoil, and Figure 3-13 depicts the profile of NREL S809 aerofoil.

Structured and unstructured grids are used in aerofoil modelling for comparing the accuracy of the simulation result. In Figure 3-1 and 3-13, the red line is the mean camber line and is located at a point halfway between the upper and lower surface of the aerofoil. Both Figure 3-1 and 3-13 demonstrate the fact that neither geometry is symmetry. This is because of the curvature of mean camber line, which allows lift to be generated when the angle of attack is 0°.
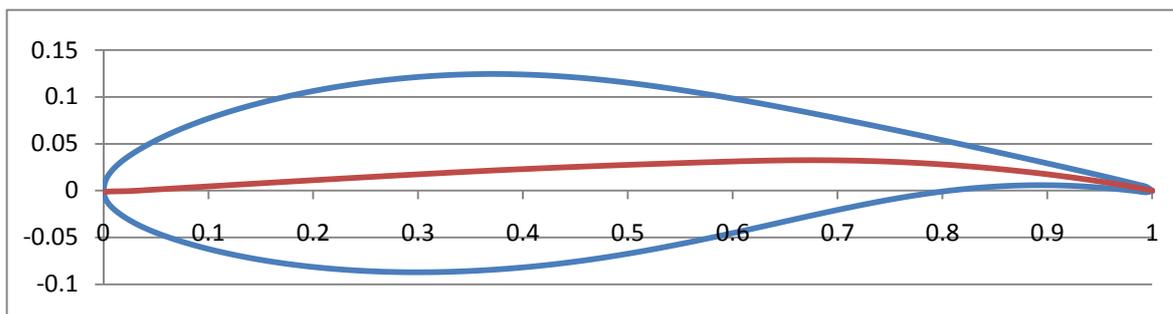
Figure 3-1 The profile of DU93-W-210

To allow the air flow to be fully expanded, the length of computational domain using structured grid is determined at 32.5 times that of chord length, and the width is determined at 25 times that of chord length, as shown in Figure 3-2.
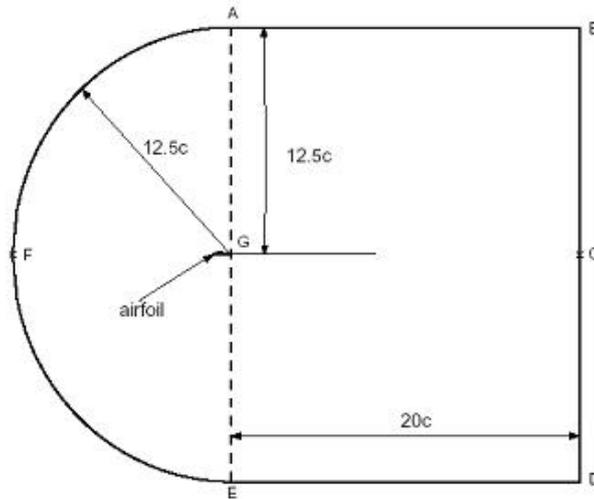
(Note that: c is chord length)

Figure 3-2 Computational Domain of DU93-W-210 by using structured grid

The mesh consists of 50,000 quadrilateral cells, of which, 300 are on the aerofoil. A large number of grids around the aerofoil surface is used to capture the pressure gradient accurately at the boundary layer. This is because the adverse pressure gradient induces flow separation. Stall will occur when separation region extends. In the far-field area, the mesh resolution can become progressively coarser since the flow gradients approach zero. The meshing overview is shown in Figure 3-3.
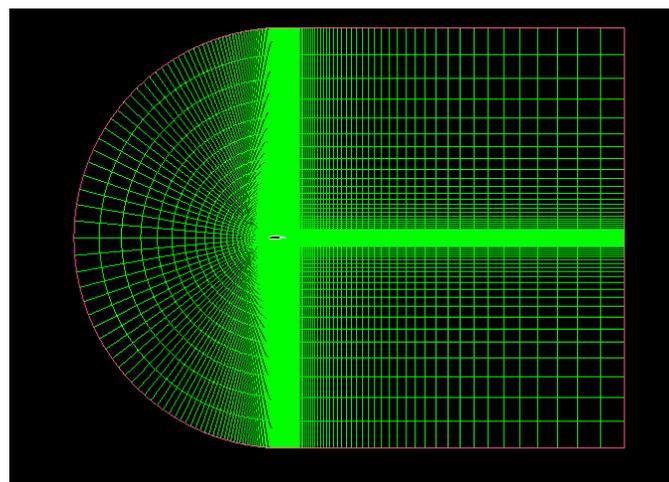
Figure 3-3 DU93-W-210 meshing by using structured grid

In Figure 3-4, close to the aerofoil surface, the most grids should be located near the leading and trailing edges since these are critical areas with the

23

steepest gradients. It is better to transit the mesh size smoothly, because the large and discontinuous transition may decrease the numerical accuracy.
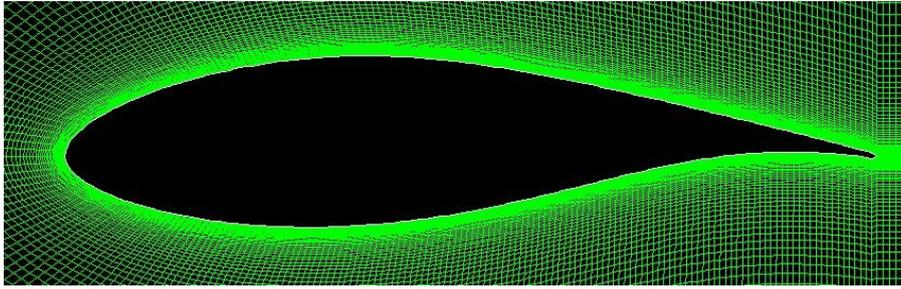
Figure 3-4 Mesh around DU93-W-210 by using structured grid

With an unstructured grid, the length of computational domain is set at 20 times that of the chord length and the maximum width is set at 24 times that of the chord length, as shown in Figure 3-5. The mesh consists of 147472 triangular cells, 300 cells are on the aerofoil surface.
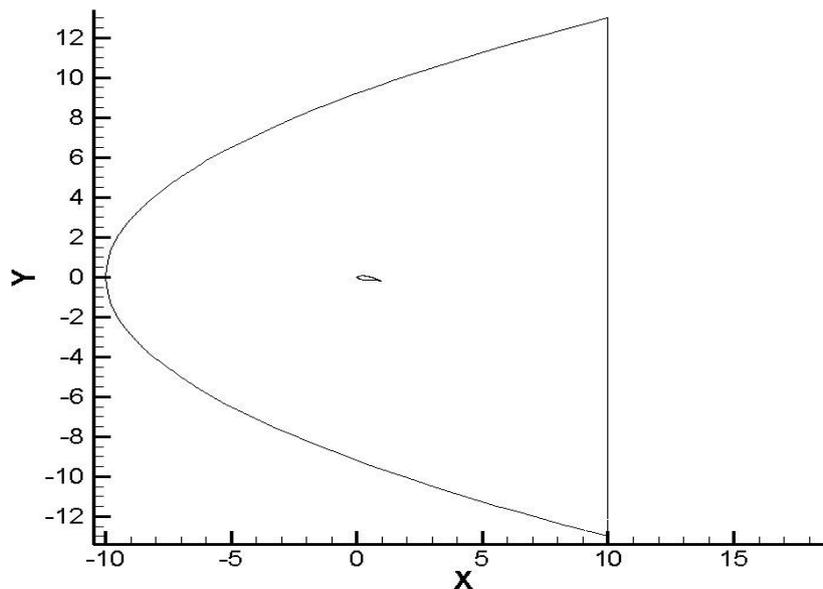
Figure 3-5 Computational Domain of DU93-W-210 by using unstructured grid

When the identical mesh strategy was used in unstructured grid: close to the aerofoil surface, the most grids should be located near the leading and trailing edges to capture the pressure and velocity gradient, and use coarser mesh in the far-field area. The overviews of unstructured grid are shown in Figure 3-6 and 3-7.

24
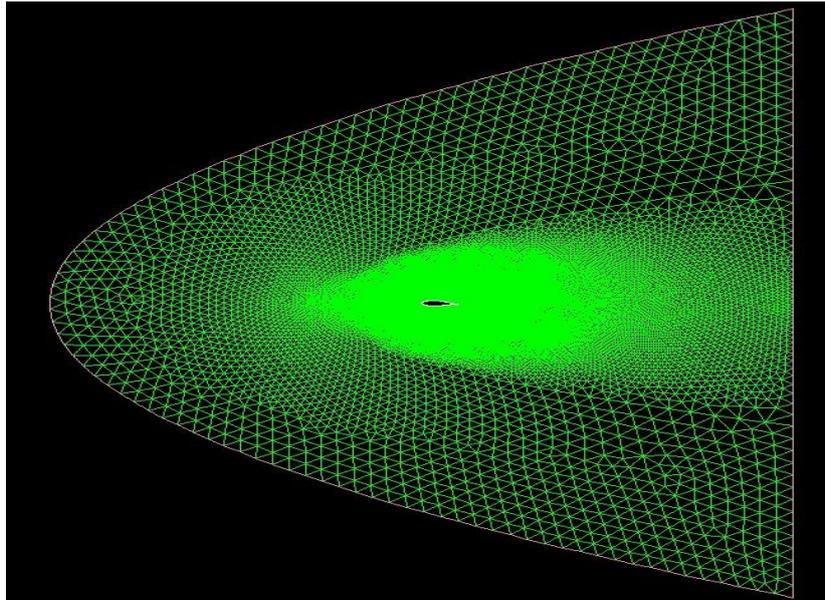
Figure 3-6 DU93-W-210 meshing by using unstructured grid
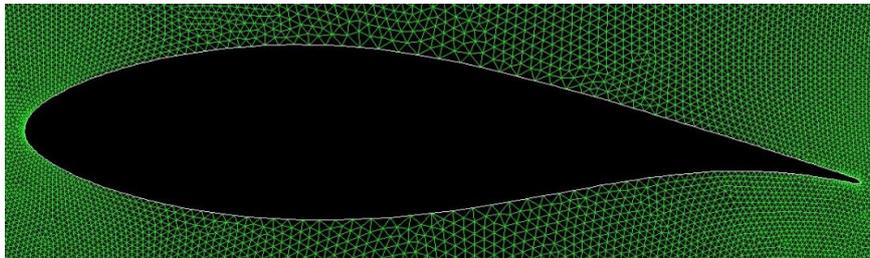
Figure 3-7 Mesh around DU93-W-210 by using unstructured grid

Pressure far-field boundary condition was used in both meshing methods as the computational domain is large enough. Aerofoil is treated as stationary wall condition with no slip shear condition. The computational condition is seen in Table 3-1:

Aerofoil	DU93-W-210
Simulation Type	Steady Simulation
Fluid Material	Air
Temperature	300 K
Kinematic Viscosity	1.4607×10^{-5} m^2/s
Reynolds Number	1,000,000
Density	**1.2** kg/m^3
Pressure	101325 pa
Wind Speed	23.8 m/s

CFD algorithm	SIMPLE (default option)
Turbulent model	Spalart-Allmaras
Interpolating scheme	Pressure (Standard)
	Density (Second Order Upwind)
	Momentum (Second Order Upwind)
	Modified Turbulent Viscosity (Second Order Upwind)
Boundary condition	Pressure far field
	Stationary wall with no slip shear condition

Table 3-1 Computational conditions of aerofoil simulation

In order to compare the experimental data with the simulation outcome under the same testing condition, the Reynolds number was set up as 1,000,000 and wind speed is 23.8 m/s. By using Equation 2-8, aerofoil chord length can be calculated which is 0.61 meter.

Spalart-Allmaras model will be used for turbulent modelling because it is designed specifically for aerospace application, which involves wall-bounded flow and has been shown good results for boundary layers subjected to adverse pressure gradients. Before running the simulation, lift, drag and pitching moment coefficients need to be monitored in ANSYS-Fluent and will be used to estimate the convergence of calculation. Lift coefficient is defined to be perpendicular to the direction of oncoming airflow; drag coefficient is defined to be parallel to the direction of oncoming airflow and the pitching moment centre is set at 1/4 chord length from the leading edge.
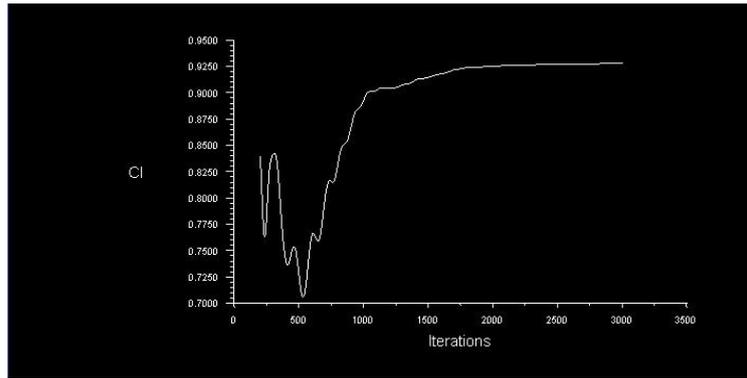
Figure 3-8 The value of lift coefficient

Figure 3-8 is the polar curve of the lift coefficient: the horizontal-axis is the value of iteration times and the vertical-axis represents the value of the lift coefficient. Initially, the value of lift coefficient was going down, the lowest value is 0.71 when the simulation was iterated 500 times. Then, it climbs to 0.925 and keeps at a stable level after 2500 iterations. This means the simulated results are converged. From Figure 3-8 to 3-10, it is obvious that the drag and pitching moment coefficients are converged earlier than the lift coefficient.
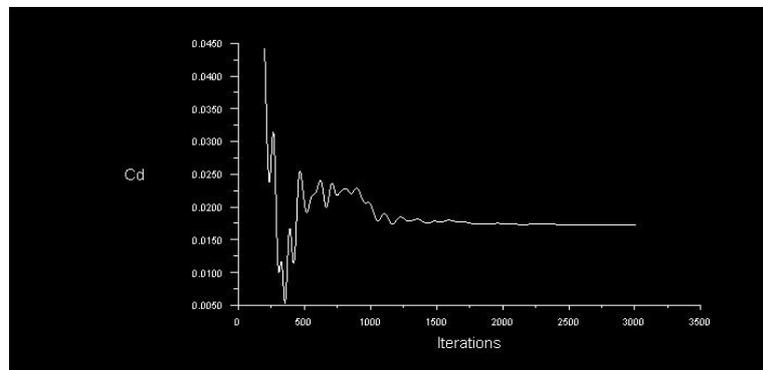
Figure 3-9 The value of drag coefficient
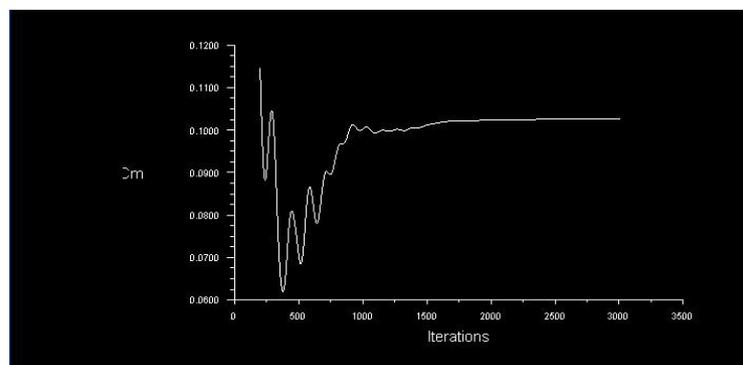
Figure 3-10 The value of moment coefficient

27

Pressure and velocity distributions can be displayed when the simulations are finished. For instance, Figure 3-11 shows the pressure on the lower surface of DU93 which is greater than the upper surface when the angle of attack is 3.6°. It also shows that the maximum static pressure, which is 300 Pascal, locates at the leading and trailing edge areas of the lower surface. The minimum static pressure is distributed on the upper surface. As shown in Figure 3-12, air flow is attached to the aerofoil and it is obvious to see that the air passes through the upper surface, which is faster than the lower surface and the maximum air velocity is 34 m/s.
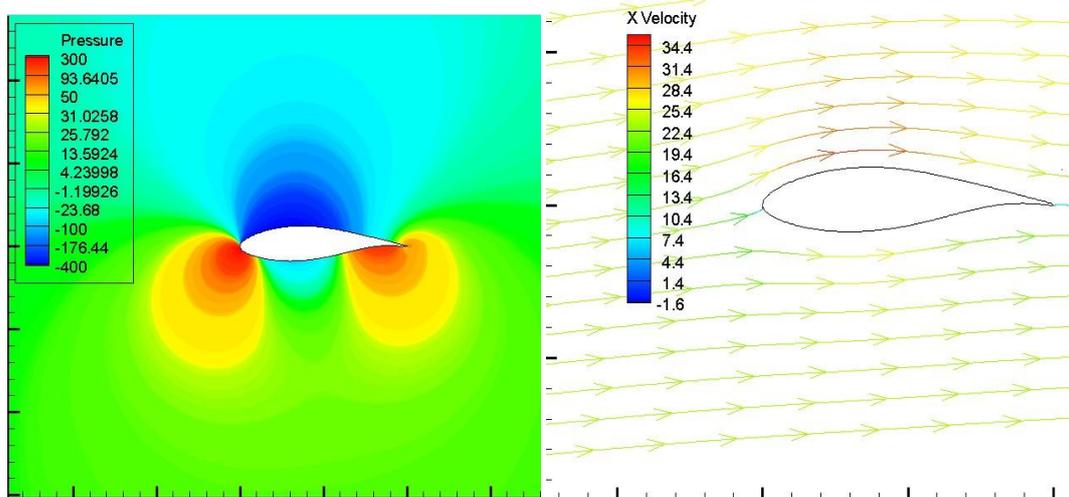
Figure 3-11 Static pressure contour at 3.6°   Figure 3-12 Stream line of x-velocity at 3.6°

3.1.2 NREL S809 modelling

Figure 3-13 is the profile of NREL S809 airfoil. We use the same meshing methods for the Modelling the NREL S809. Here the length of computational domain for the structured grid was 32.5 times that of chord length and width was 25 times the chord length. The mesh consists of 50,000 quadrilateral cells, of which 300 are on the aerofoil control surface. For an unstructured grid, the length of computational domain was 20 times of chord length and maximum width was 24 times that of chord length. The mesh consists of 147472 triangular cells, 300 cells are on the aerofoil surface. By using identical boundary and computational conditions, the pressure and velocity distributions were obtained by the software.
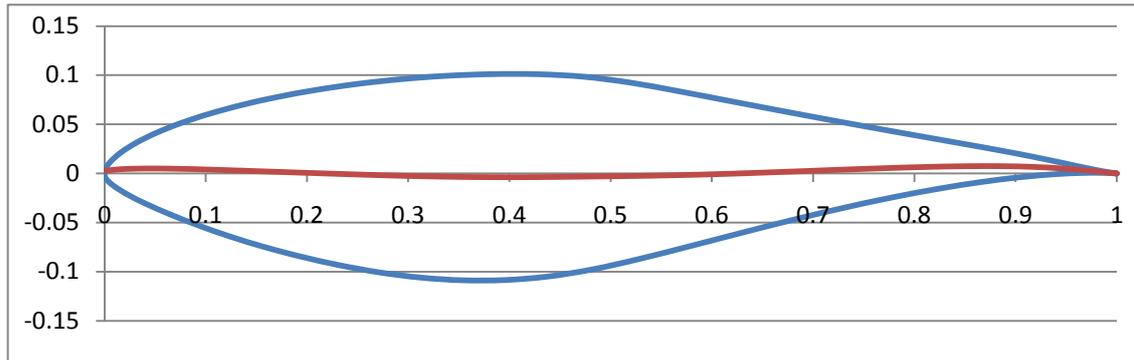
Figure 3-13 The profile of NREL S809
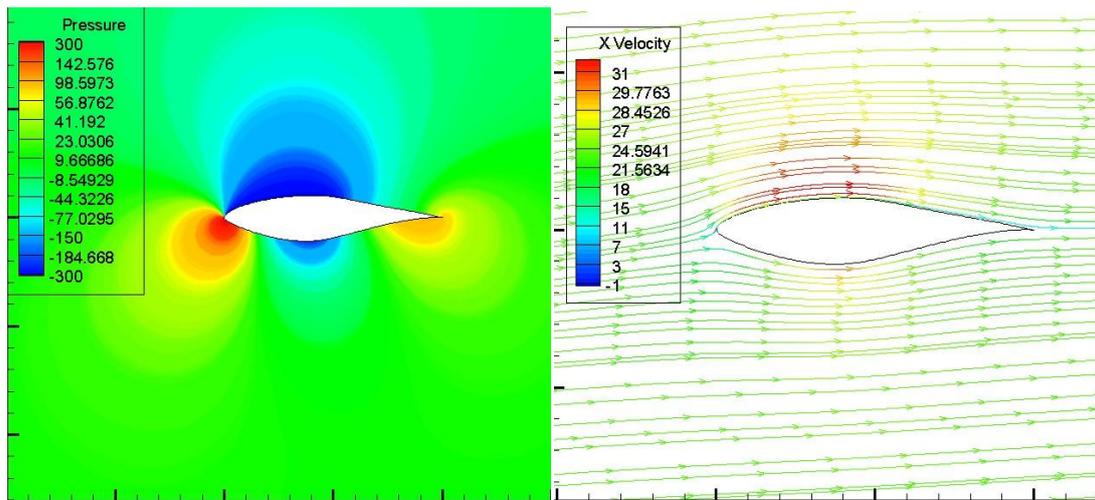
Figure 3-14 Static pressure contour at 3.6°   Figure 3-15 Stream line of x-velocity at 3.6°

The maximum static pressure on S809 was also 300 Pascal, too, which located at the leading and trailing edge area of lower face. But the minimum static pressure was smaller than DU93. As a consequence, it can be seen from Figure 3-15, the maximum velocity of air was 31 m/s which was slower than DU93.

3.2 Aerofoil modelling using structured and unstructured grid

Compared with a structured grid, an unstructured grid has good adaptability for simulating models with a complicated boundary condition, and also where the mesh density is difficult to control. In order to find out the most accurate simulated approach with DU93, both structured and unstructured grids were utilized under the identical computational condition.

AoA	Lift Coefficient				
	Experiment data	Structured grid	% error	Unstructured grid	% error
0°	0.485	0.3969	-18.16%	0.42521	-12.33%
5°	1.072	0.92765	-13.47%	0.92959	-13.28%
10°	1.337	1.374657	2.81%	1.200537	-12.70%

Table 3-2 Lift coefficient between structured and unstructured grid

AoA	Drag Coefficient				
	Experiment data	Structured grid	% error	Unstructured grid	% error
0°	0.00874	0.01245	42.45%	0.003413	-61%
5°	0.0102	0.017303	69.63%	0.008877	-13%
10°	0.02223	0.028798	30.00%	0.026864	20.85%

Table 3-3 Drag Coefficient between structured and unstructured grid

AoA	Moment Coefficient				
	Experiment data	Structured grid	% error	Unstructured grid	% error
0°	-0.1249	-0.10586	-15.24 %	-0.11074	-11.33%
5°	-0.132	-0.10261	-22.30 %	-0.109658	6.87%
10°	-0.1029	-0.09173	10.90 %	-0.083392	-19%

Table 3-4 Moment Coefficient between structured and unstructured grid

Compared with experimental data, the structured grid shows better results under a small angle of attack (Tables 3-2, 3-3, and 3-4). While increasing the angle of attack, lift, drag and moment coefficient with both grids begin to oscillate, this is because under the high angle of attack, around the trailing edge area, vortex shedding occurs periodically.
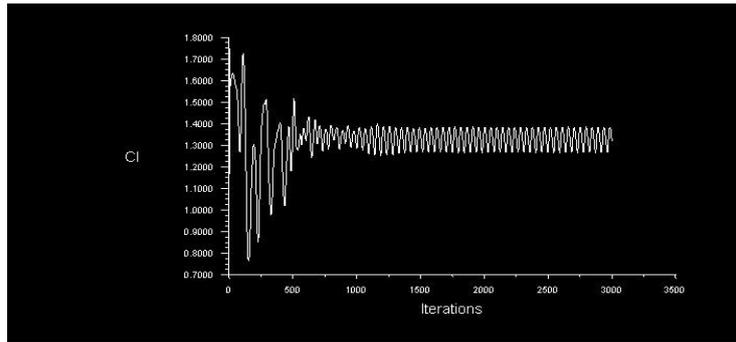
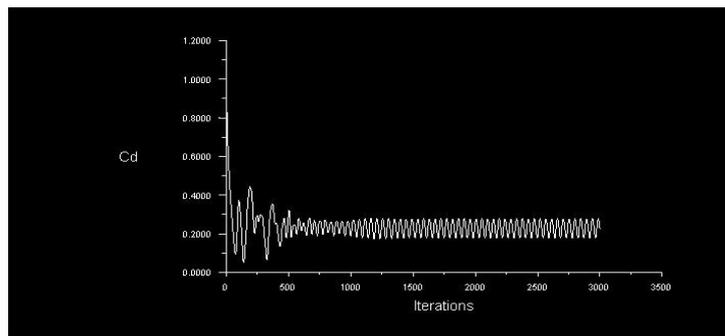**Figure 3-16 Lift coefficient of unstructured grid at 22°**

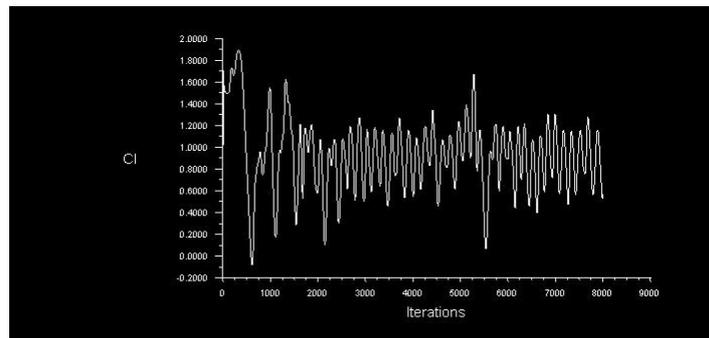**Figure 3-17 Drag coefficient of unstructured grid at 22°**

Figure 3-18 Lift coefficient of structured grid at 22°
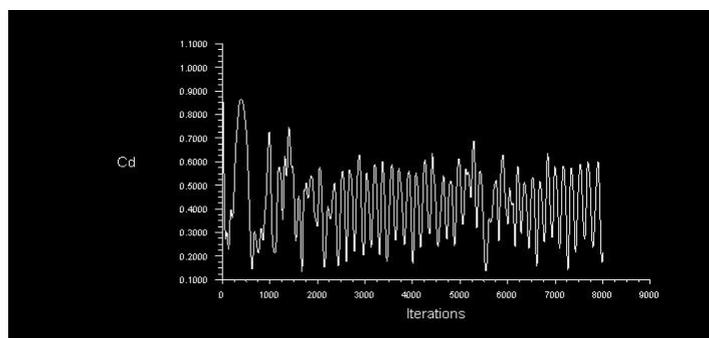
Figure 3-19 Drag coefficient of structured grid at 22°

Figures 3-16 and 3-17 are the lift and drag coefficients of unstructured grid at

31

22°, Figures 3-18 and 3-19 are the lift and drag coefficients of structured grid at 22°. Comparing with unstructured grid, lift and drag coefficient in structured grid oscillate considerably. This is because when using a structured grid to model the aerofoil, different angles of attack are simulated by changing the velocity vector and keeping the aerofoil in a horizontal direction, grid would not be aligned with the flow anymore when suffers a high AoA. For the unstructured grid, different angles of attack are simulated by pitching the aerofoil which likes real wind tunnel testing. In order to reduce the oscillation and obtain more reliable results, the structured grid is used for low angles of attack (-10° to 10°) and unstructured grid is for angles outside this range.

3.3 Aerofoil CFD modelling using pressure and density-based solver

In ANSYS Fluent, the pressure-based solver is suitable for low-speed (Ma<1) incompressible flow and density-based solver is mainly used for high-speed compressible flows. In the pressure-based approach, pressure and pressure correction equations are used for the calculation of pressure fields. In the density-based approach, continuity equation is used to obtain the density field. The velocity field can be obtained from the momentum equation in both solvers (Fluent user's guide, 2006). Due to the low Mach number (normally Ma≤0.3); density does not change when pressure varies, so air can be treated as incompressible flow. By using a structured grid and unified boundary condition, the simulation results are shown in Tables 3-5 to 3-7:

AoA	Lift Coefficient				
	Experiment	Density Based	% error	Pressure Based	% error
0°	0.485	0.3969	-18.16%	0.400876	-17.35%
5°	1.072	0.92765	-13.47%	0.936198	12.67%
10°	1.337	1.374657	2.81%	1.38703	3.70%

Table 3-5 Lift coefficient between pressure based and density based solver

AoA	Drag Coefficient				
	Experiment	Density Based	% error	Pressure Based	% error
0°	0.00874	0.01245	42.45%	0.011369	30%
5°	0.102	0.017303	69.63%	0.014942	47%
10°	0.02223	0.028798	30.00%	0.024751	11.34%

Table 3-6 Drag coefficient between pressure based and density based solver

AoA	Moment Coefficient				
	Experiment	Density Based	% error	Pressure Based	% error
0°	-0.1249	-0.10586	-15.2 %	-0.106715	-14.53%
5°	-0.132	-0.10261	-22.30%	-0.104268	-21.00%
10°	-0.1029	-0.09173	-10.90%	-0.094409	-8.25%

Table 3-7 Moment coefficient between pressure based and density based solver

It can be seen from Tables 3-5 to Table 3-7 that pressure based solvers is more reliable than density based solver, especially for calculations of drag coefficient. For both solvers, the simulated results are closer to the experimental data when AoA increases. The comparisons of different solvers and meshing strategies imply that, the final approach of 2D simulation is using pressure based solver and structured grid to simulated aerofoil in small angles of attack (-10°≤AoA≤10°), beyond this range, an unstructured grid will be implemented.

3.4 Three-dimensional wind turbine modelling

Basic parameters		
Power	P / W	**9518**
Wind velocity	m/s	**8.8**
Number of blades	z	**3**
Optimal Tip speed ratio	Lambda	**8**
Air density	kg/m^3	**1.2**
Radius of the rotor	R / m	**4.5**
Generator RPM	rpm	**150**
Aerofoil		**DU93W210**

Table 3-8 Basic parameters of rotor blade

Table 3-8 shows the basic parameters of wind turbine, this wind turbine consists of 3 blades and optimal tip speed ratio is 8, the nominal rotational speed is 150 rpm when wind speed has reached to 8.8 m/s, under this condition, the power output of generator is 9518 w.
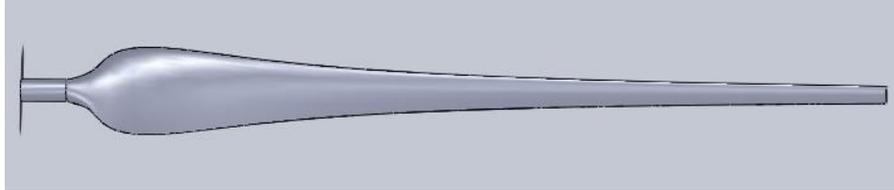
Figure 3-20 Original blade with rectangular tip

The original blade wingspan is 4.5 m and DU93 is used as the aerofoil of this blade. Chord length of the blade tip is 0.097 m and while root is 0.421 m; twisted angle varies along the wingspan. This blade is shown in Figure 3-20.
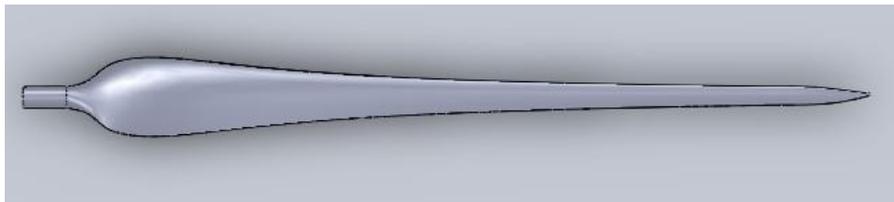
Figure 3-21 Original blade with tapered tip

Figure 3-21 is the original blade with tapered tip, the blade tip is sharper than rectangular tip, and the aerodynamic noise can be reduced by using this design. The performance of noise reduction for those two tips will compare in the following chapter.
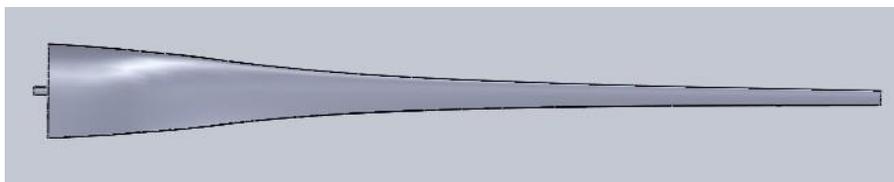
Figure 3-22 New blade with innovated root

The innovated root blade is formed by remaining the twisted angle of original blade, but only extending the chord length of root to 0.6 m. it can be seen in Figure 3-22.
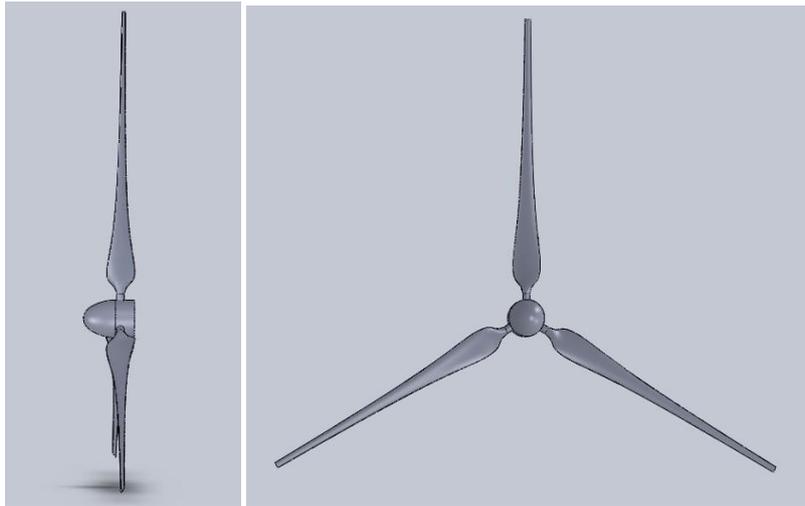
Figure 3-23 Wind turbine with original blades (rectangular tip)
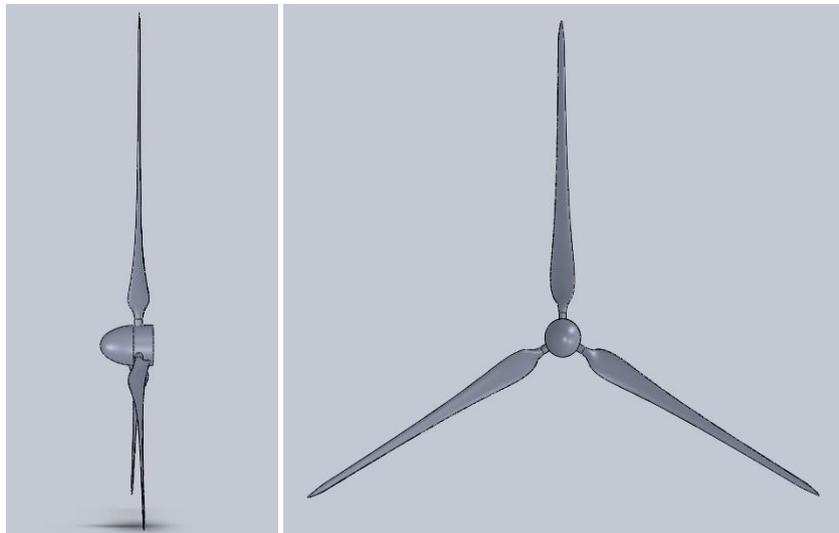
Figure 3-24 Wind turbine with original blades (tapered tip)

Wind turbine consists of 3 blades and 1 hub, seeing from Figures 3-23 and 3-24, original rotor blades with rectangular and tapered tip use the same hub which the length is 0.8 m and diameter is 0.6 m.
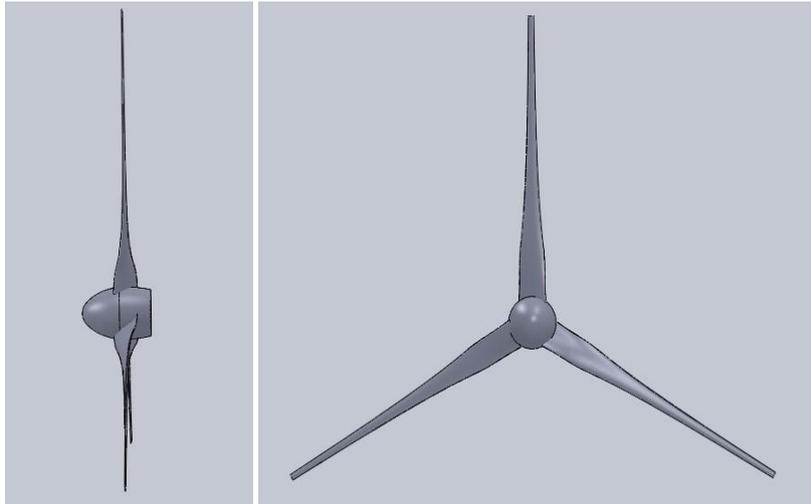
Figure 3-25 Wind turbine with new blade (new hub and rectangular tip)

Comparing with original blade, the new blade has a bigger root area; hub needs to redesign in order to content the root area. The length of hub is 1.1 m and diameter is 0.84 m. All rotor blades and wind turbine models were modelled using Solidworks 2009. After that, the wind turbine model was imported to GAMBIT once modelled in Solidworks. In Chapter 4; using the same meshing approach, different geometry of blade roots and tips will be compared under the different wind for predicting the power output.
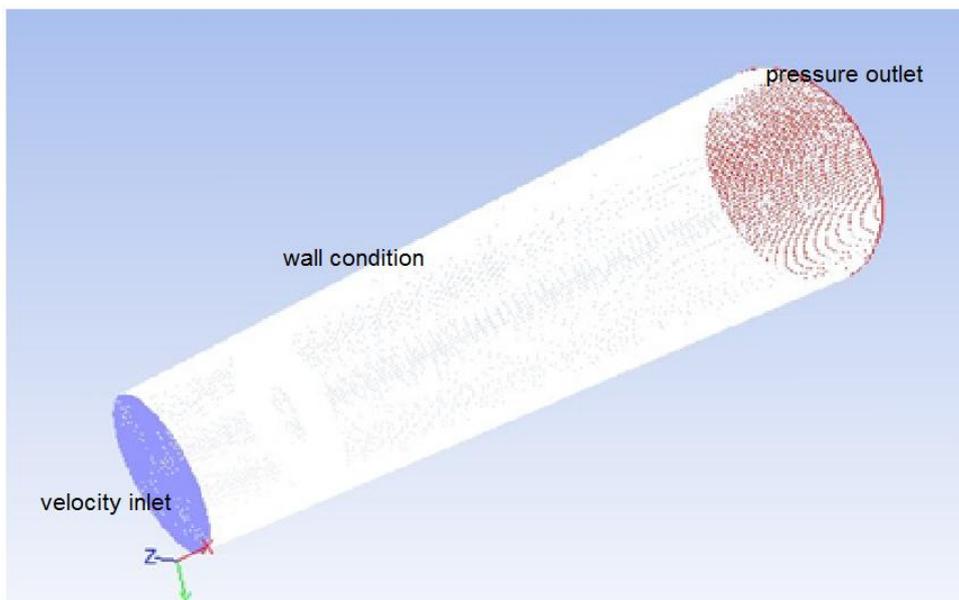
Figure 3-26 Computational domain of wind turbine simulation

The computational domain was designed as a conical shape to reduce the model size; it was extended in the axial direction about 2 diameters upstream and 15 diameters downstream of the rotor (Figure 3-26). This was to make sure the air flow could be fully extended. The radius of inlet is 2 times that of rotor blade and the radius of outlet is 4 times that of blade. The blockage ratio is difeined as $\phi = \dfrac{h}{H}$, where h is the diameter of wind turbine and H is the height of computational domain. Blockage will cause flow characteristics to differ from those expected in full scale situations without wall constraints (Cheung and Melbourne, 1980). So in the wind tunnel test or CFD simulation, a smaller blockage ratio means it is closer to the field testing. Carlo (2008, p. 36) states in the plane of the rotor, the height of computational domain was five times that of the rotor which means the blockage ratio is 20%. Considering the configuration of computer, the blockage ratio is increased to 33% for this wind turbine simulation. The boundary condition was set up as velocity inlet. Pressure outlet and wind turbine was treated as wall condition. Wind turbine rotational effect can be simulated by using sliding mesh.
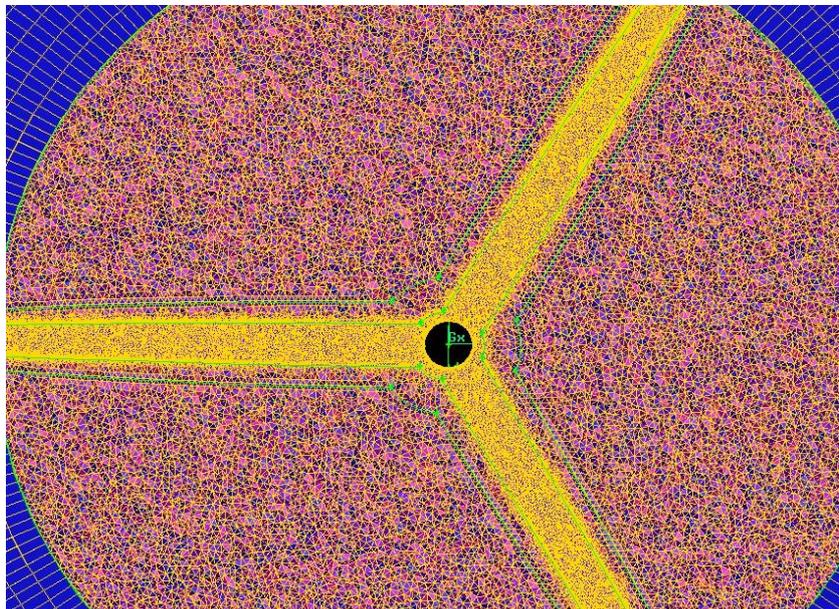
Figure 3-27 Wind turbine meshing by using unstructured grid

The air flow passing through a rotating and twisted HAWT blade is much more complicated due to the angles of attack varying along the aerofoil span. In order to reduce the meshing difficulty, an unstructured grid was used to mesh

37

the wind turbine as it has a nice adaptability. A structured grid was used to mesh the remaining of the computational domain as it has a nice meshing quality. Figure 3-27 shows that unstructured grids are located in rotational area and structure grids are utilized beyond that range. Moreover, in order to improve the accuracy of simulation, the mesh size is small and intensive around the wind turbine.
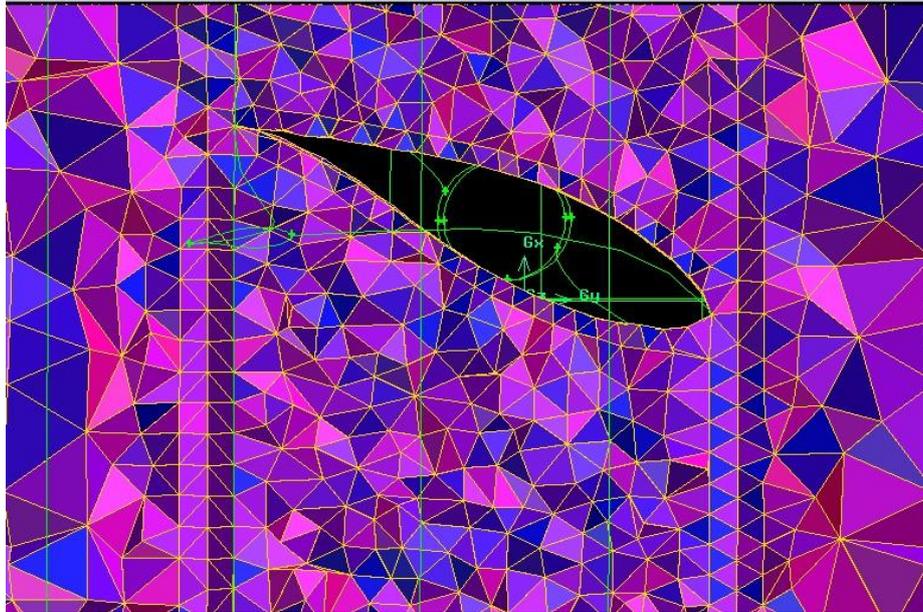
Figure 3-28 Blade section meshing by using unstructured grid

Figure 3-28 shows that the mesh is denser near the wind turbine and gets coarser when the mesh approaches towards the boundaries. This meshing approach is able to capture the boundary layer near the wind turbine (Digraskar, 2010, p.31).
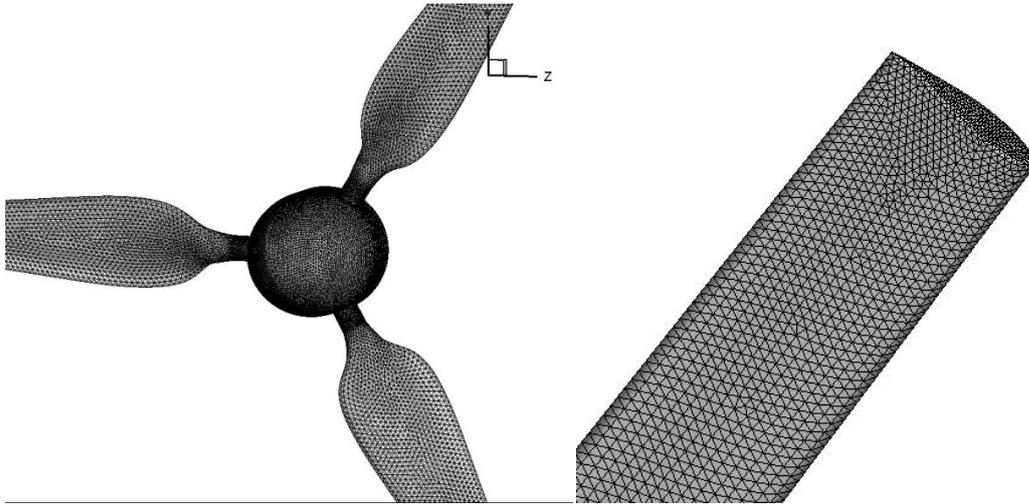
Figure 3-29 Wind turbine with original blades meshing (rectangular tip)
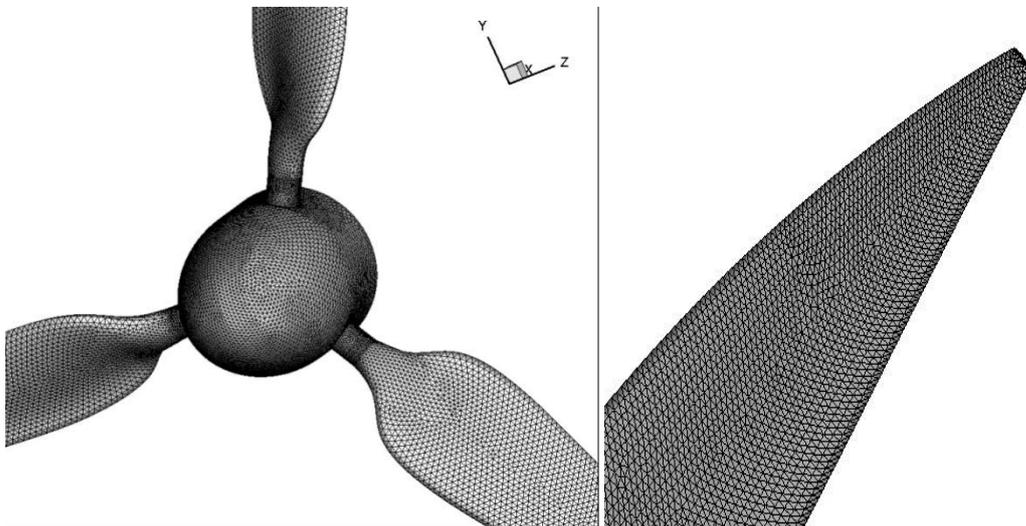
Figure 3-30 Wind turbine with original blades meshing (tapered tip)
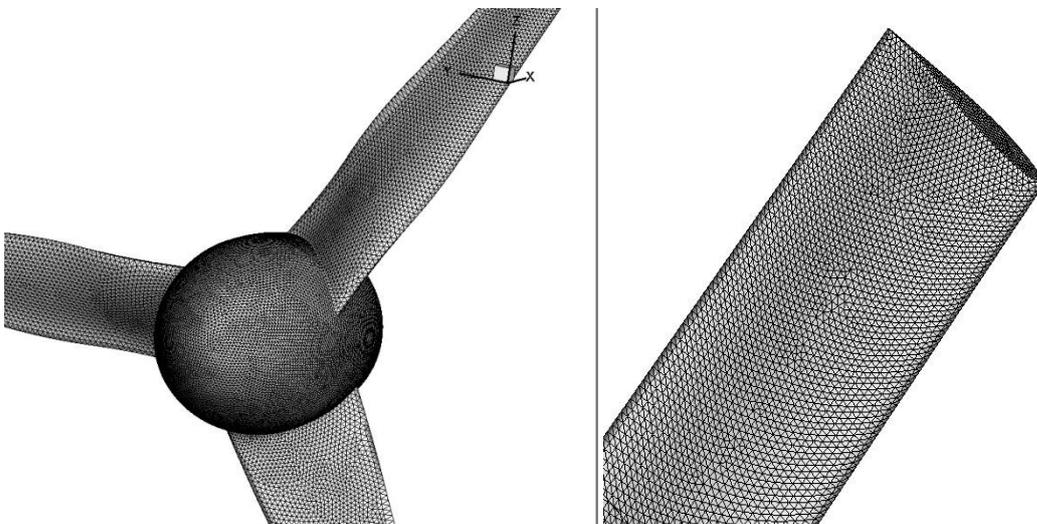
Figure 3-31 Wind turbine with innovated root meshing (new hub and rectangular tip)

Figures 3-29, 3-30 and 3-31 are the surface meshing of the wind turbine rotors, in order to capture vortices wake, many cells were assigned around the blade tips. After finishing the meshing process, wind turbine mesh was imported to ANSYS-Fluent and the boundary condition is seen below:

Blade	10kW@8.8m/s wind turbine blade design using DU93W210 aerofoil
Simulation Type	Transient Simulation
Fluid Material	Air
Flow Type	Incompressible flow
Temperature	300 K
Kinematic Viscosity	1.4607×10^{-5} m^2/s
Pressure	101325 pa
Wind Speed	2.4~18 m/s
Pitch Angle	4.75°
CFD algorithm	SIMPLE
Turbulent model	SST k-ω
Interpolating scheme	Pressure (Standard) Density (Second Order Upwind) Momentum (Second Order Upwind) Modified Turbulent Viscosity (Second Order Upwind)
Boundary condition	Velocity Inlet and Pressure Outlet Moving wall with no slip shear condition
Mesh cells	5804232

Table 3-9 Computational conditions of three-dimensional simulation

In Ansys-Fluent, Pressure-based solver and transient solution were used for wind turbine modelling. SST k-ω model was used because Carcangiu (2008, p.26) states that it includes a number of features that make it more accurate

40

and reliable for a wider class flows (e.g., adverse pressure gradient flows and aerofoil). When simulation is over, torque (Figure 3-32) and thrust can be displayed and mechanical power will be calculated by using the value of torque.

```
Reading "D:\New folder\new blade  different pitch\25-07 old root smal
Parallel variables...
Done.

Moments - Moment Center (1 0 0)
                         Moments (n-m)
Zone                     Pressure
wind_turbine             (748.7569 -7.1526184 -40.438721)
----------------------   ------------------------------------------
Net                      (748.7569 -7.1526184 -40.438721)

Moments - Moment Center (1 0 0) Moment Axis (1 0 0)
                         Moments (n-m)
Zone                     Pressure        Viscous          Total
wind_turbine             748.7569        -21.670578       727.08632
----------------------   --------------  --------------   -----------
Net                      748.7569        -21.670578       727.08632
```

Figure 3-32 Torque calculation by using ANSYS-Fluent with 8.8 m/s wind speed

An appropriate step size is indispensable in achieving different simulated purposes for three-dimensional models. Using larger time step is acceptable, if a steady state solution wants to be obtained to calculate the torque and thrust of wind turbine. Small time step size will be used when transient solution is desired, for instance vortex shedding and wind turbine wake. The smaller the time step, then, the more detail of the flow will be obtained. Also, if simulated model is not encountering high velocities, then using segregated solver will definitely improve speed of computation. Four different time step sizes which are 0.01, 0.005, 0.002 and 0.001s were used for comparison in order to test how they influence the simulated result. Because the rated rotational speed is 150 rpm when wind speed is 8.8 m/s, a complete revolution takes 0.4s which means 40, 80, 200 and 400 time steps will take when time step sizes were 0.01, 0.005, 0.002 and 0.001s.

Time step size (s)	Simulated torque (n-m)	Theoretical torque (n-m)	Error %	Time step	Simulation time
0.01	1112.4054	739.90	50.88%	40	3 hours
0.005	747.4973	739.90	1.08%	80	7 hours
0.002	720.12349	739.90	-2.57%	200	18 hours
0.001	727.08632	739.90	-1.73%	400	40 hours

Table 3-10 Comparison of different time step size

The theoretical torque was calculated by using BEM theory. In order to simplify the model, the tip loss factor was not taken into account. seeing from Table 3-10, it is obvious that a big time step size leads a coarse result but a short time to simulate. It will take a long time to calculate if the time step size is too small, although a nice simulated result can be obtained. Several cases need to be calculated for predicting the wind turbine output power, in order to save time, using 0.005s as a fixed time step size.

3.5 Three-dimensional wind turbine noise Modelling using Gambit and ANSYS Fluent

The computational domain was designed as cylindrical shaped (Figure 3-33), extending in the axial direction about 7.5 diameters upstream and 15 diameters downstream of the rotor to make sure the air flow can be fully extended. In the plane of inlet and outlet, the radius of domain is 1.5 times of rotor blade. In order to predict the aerodynamic noise, two approaches are used in ANSYS-Fluent (Fluent 6.3 User's Guide, 2006); using the Flowcs Williams and Hawkings Model for predictions of near- to far-field noise and using broadband noise source method for predicting aerodynamic noise of the wind turbine.
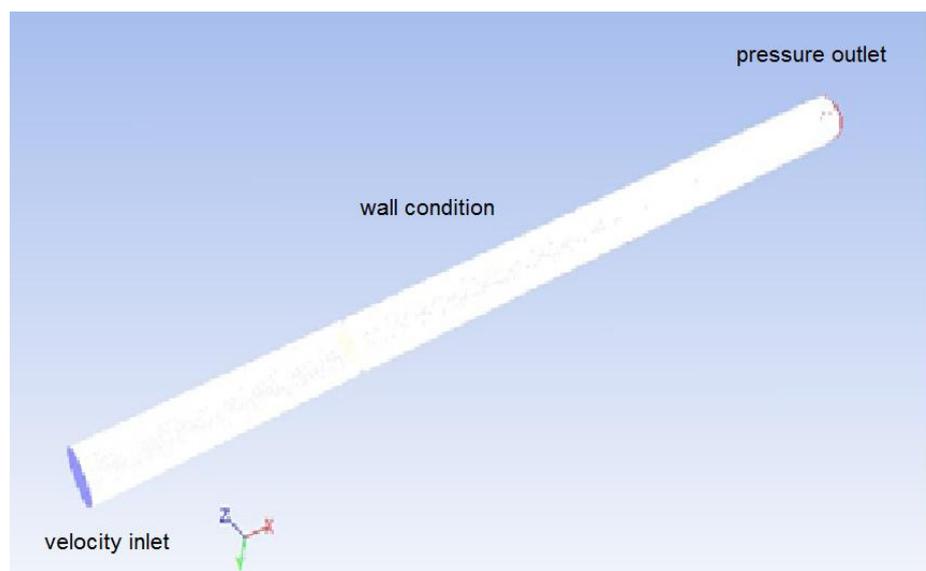

Figure 3-33 Computational domain of noise prediction
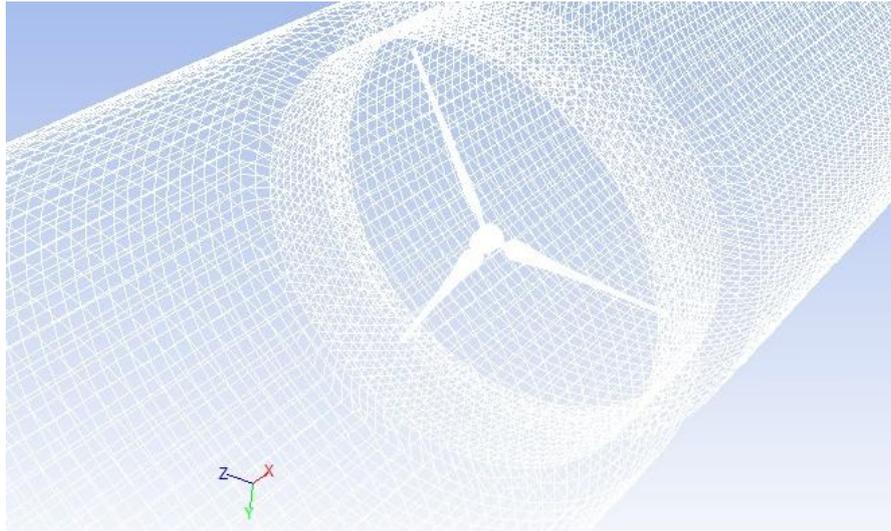
Figure 3-34 Wind turbine meshing

3.5.1 Using Fflows Williams and Hawkings acoustic model to predict the near- to far field noise

The procedure for computing sound using the FW-H (Ffowcs Williams and Hawkings) acoustics model in ANSYS-Fluent consists of two steps. In the first step, a time-accurate flow solution is generated, so the relevant variables (e.g., pressure, velocity and density) on the selected source surface are obtained (ANSYS-Fluent 6.3 User's Guide). In the second step, sound pressure signals which are set by the users are computed using the source data. FW-H acoustics model requires a statistically steady transient solution, this means that the unsteady flow which includes the major flow variable, has become fully developed so that its statistics do not change with time. In this model, the LES turbulence model is recommended for aeroacoustic simulations because it resolves all eddies with scales larger than the grid scale (Modelling Flow-Induced Noise Problems Using Fluent) and resolves the noise generating eddies over a wide range of length scales in engineering application. Therefore, wide band aeroacoustic noise can be predicted using LES simulation.

43

Blade	10kW@8.8m/s wind turbine blade design using DU93W210 aerofoil
Simulation Type	Transient Simulation
Fluid Material	Air
Flow Type	Incompressible flow
Temperature	300 K
Kinematic Viscosity	1.4607×10^{-5} m^2/s
Pressure	101325 pa
Wind Speed	3.5m/s, 6m/s and 8.8m/s
Pitch Angle	4.75°
CFD algorithm	SIMPLE
Turbulent model	LES
Interpolating scheme	Pressure (Standard) Momentum (Second Order Upwind)
Boundary condition	Velocity Inlet and Pressure Outlet Moving wall with no slip shear condition
Mesh cells	5348232

Table 3-11 Computational conditions of near- to far-filed aerodynamic noise predicting
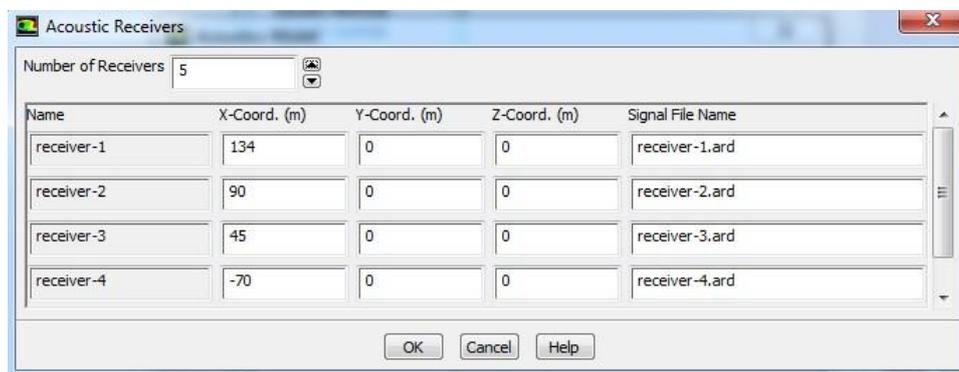

Figure 3-35 Locations of 5 acoustic receivers

Setting wind turbine as acoustic sources and specifying 5 acoustic receivers to predict the noise from near-to far-field when using FW-H acoustic model. The location of receivers can be seen from Figure 3-35 and distance between wind turbine and 5 receivers separately are 134m, 90m, 45m, 0m and -70m. In order to make sure enough simulation time will get a statistically steady transient solution, 1000 time steps with 0.005 time step size was chosen in this simulation and computational condition can be seen from Table 3-11.
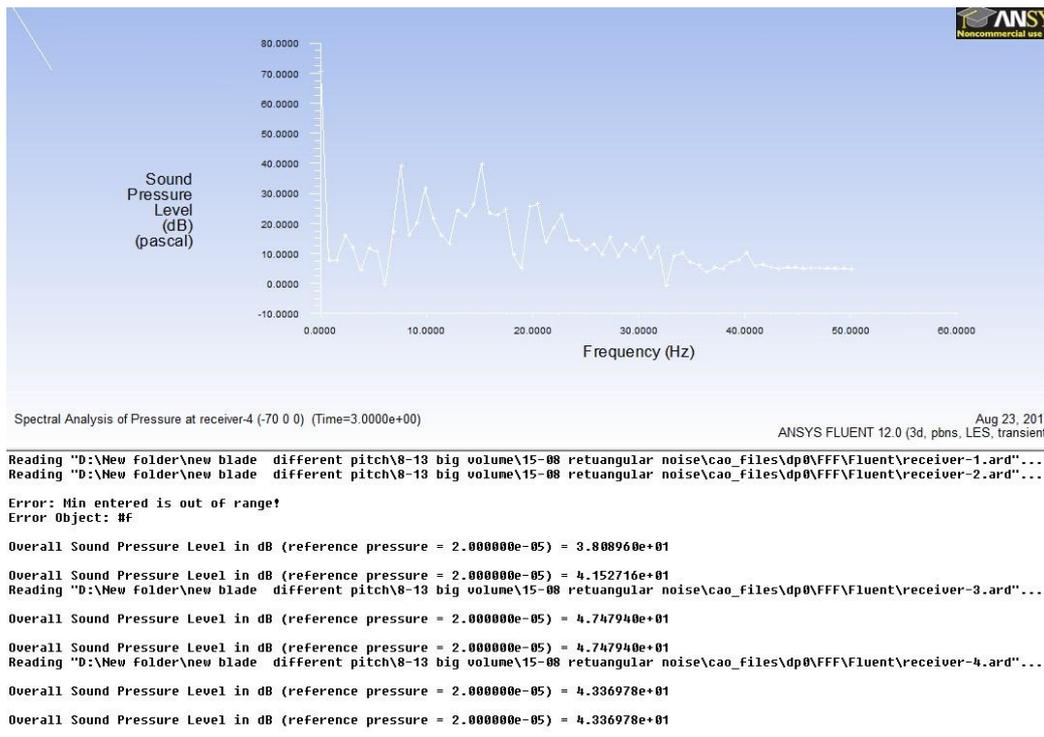
Figure 3-36 Sound pressure level of one acoustic receiver

When the simulation is completed, every receiver can be used with Fast Fourier Transform (FFT) analysis to interpret the spectral distribution of sound pressure level, the value of aerodynamics noise can be displayed in the console panel in ANSYS-Fluent (Figure 3-36).

3.5.2 **Using broadband noise source method for predicting aerodynamic noise of wind turbine**

Unlike the FW-H integral method, the broadband noise source models do not require transient solution and the typical RANS models can be used in this

45

model. Therefore, the use of broadband noise source models requires the least computational resources.

In steady state simulation, using Moving Reference Frame (MRF) to model wind turbine rotation and using the same computational domain and boundary condition in Table 3-11 to predict the wind turbine aerodynamic noise, 1000 interactions make sure the result is converged. Two different tip designs (Figure 3-37 and Figure 3-38) are tested under the wind speeds are 3.5m/s, 6m/s and 8.8m/s.

Figure 3-37 Tapered tip   **Figure 3-38 Rectangular tip**

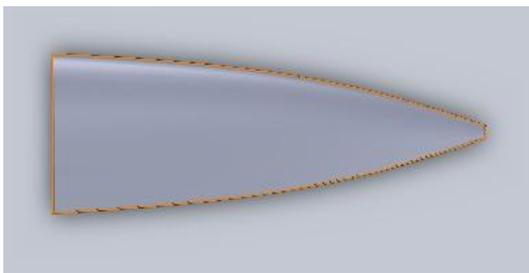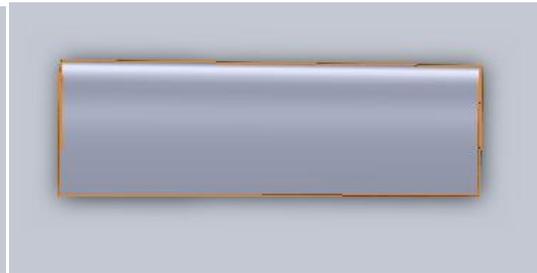# Chapter 4   Results and Discussions

In this chapter, aerodynamic analysis of aerofoils and rotor blades will be conducted in two-dimensional simulation using ANSYS Fluent. DU93-W-210 and NREL S809 aerofoils will be compared in order to find out which one has a better aerodynamic performance. In three-dimensional simulation, different blade geometries will be compared for predicting the rotor power and operation noise.

4.1 Aerodynamic performance evaluation of NREL S809 and DU93-W- 210 aerofoils

Lift and drag coefficients are the crucial values for aerodynamic performance evaluation. The critical and optimum attack angles can be estimated by plotting the lift and drag coefficient polar curves.

4.1.1 Aerodynamic performance evaluation of DU93-W- 210 aerofoil

Simulated results need to be verified with experimental data before implementing the evaluation of aerodynamic performance. From -10° to 10°, the lift and drag coefficients are shown below.

Figure 4-1 DU93 comparison of lift coefficient between experiment and Fluent

Figure 4-1 shows ANSYS Fluent simulation is fairly accurate when calculating the lift coefficient of DU93 from -10° to 10°. From -3.1° to -4.1°, the simulated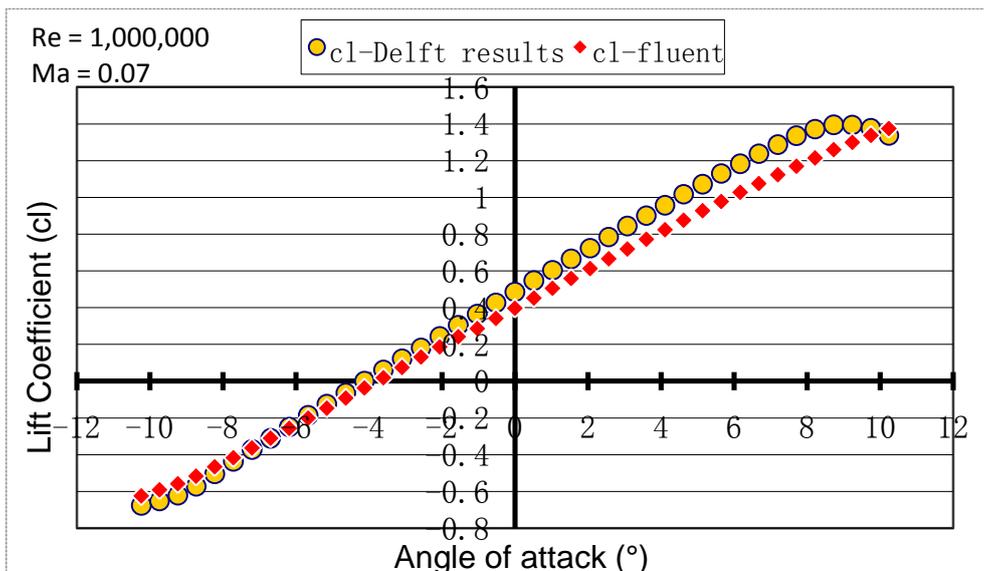 results are 35% to 45% lower than the Delft university wind tunnel test. The biggest error occurs at -4.6°, where the simulated lift coefficient is 45.37% lower than the experimental value. Beyond that range, errors of lift coefficient can be controlled less than 25%. Figure 4-1 also indicates that, from -10° to 10°, lift coefficient of DU93 increases when the angle of attack increases.
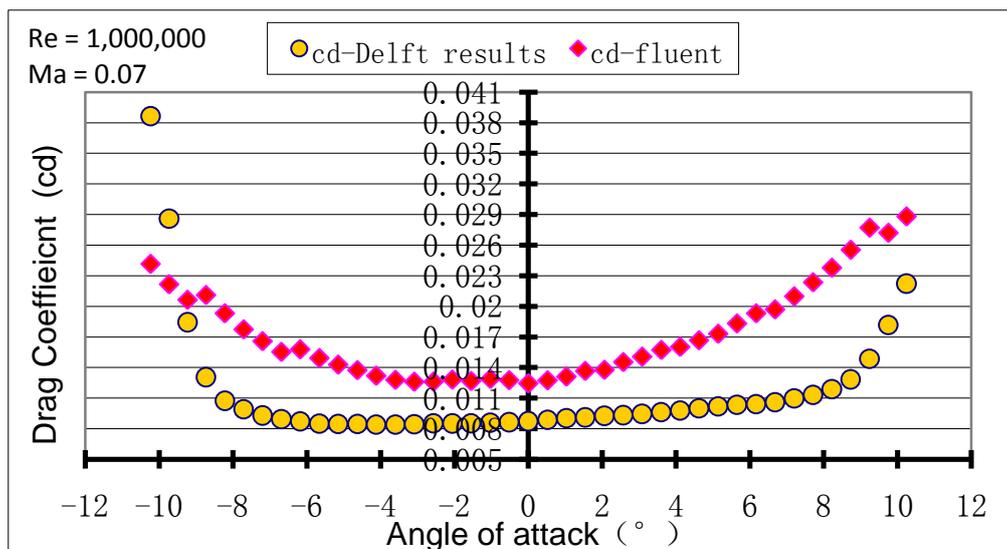
Figure 4-2 DU93 comparison of drag coefficient between experiment and Fluent

Figure 4-2 shows the corrections between the simulation and experiment are poorer by using structured grid when compares the modelling and Delft university wind tunnel test with regards to the drag coefficient. The simulated drag coefficients are 30% to 85% higher than the experimental results. This is due to the fact that the values of drag coefficient are very small from -10° to 10°, ANSYS-Fluent may not have a good ability to predict it precisely at low angles of attack.

It is interesting to observe from Figures 4-1 and 4-2 that: for most angles of attack, the simulated lift coefficients are smaller than experimental data; conversely, simulated drag coefficients are bigger than experiments. Wolfe and Ochs (1997) stated the overprediction of lift and drag coefficient is due to the actual aerofoil having laminar flow over forward half, but in the CFD

modelling, simulations are running under the fully turbulent model which may influence the prediction of lift and drag coefficient.

4.1.2 **Aerodynamic performance evaluation of NREL S809 aerofoils**

From -20° to 26°, the comparison between calculated and experimental data can be plotted by using the S809 experimental data from OSU (Ohio State University- USA).

Figure 4-3 S809 comparison of lift coefficient between experiment and Fluent

The biggest error occurs at 0° where simulated lift coefficient is 51.61% higher than the experimental value. Beyond this point, errors can be limited less than 35%, and the smallest error occurs at 4°, where simulated result is 0.74% lower than the experimental value.
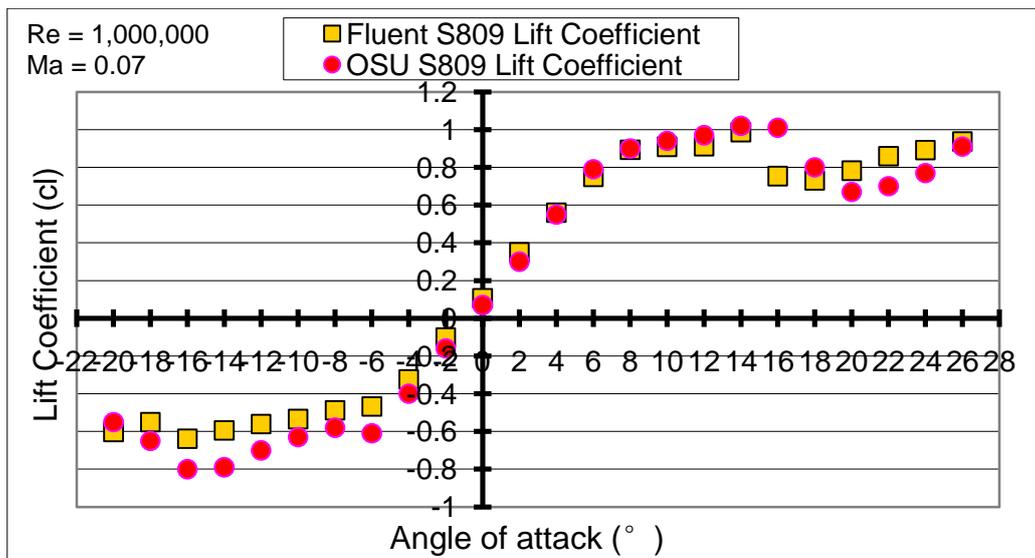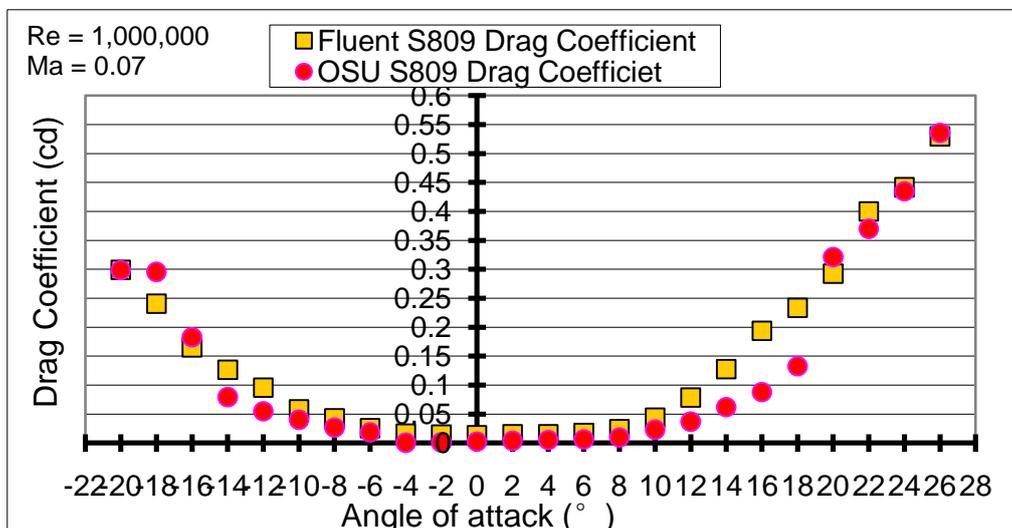
Figure 4-4 S809 comparison of drag coefficient between experiment and Fluent

In Figure 4-4, ANSYS-Fluent shows fair correlation with OSU values. However, the error is quiet big at small angles of attack. From 0° to 8°, the simulated results are 145% to 413% higher than the experimental values. The biggest error occurs at 0° where simulated result is 413.55% higher than experiment. Firstly, the major error may be caused by the very low experimental drag coefficient at that range. OSU values indicate that the drag coefficient is 0.0022 when angle of attack is 0°, and for ANSYS-Fluent, it is difficult to capture such a precise value during the simulation. Secondly, this may be due to the defining coordinates give insufficient definition of the S809 aerofoil. This is because DU93 aerofoil consists of 200 coordinates and most of them are used for defining the leading and trailing edge. Comparing this with DU93 aerofoil; only 50 coordinates were used to define the profile of S809 aerofoil which leads to inaccuracies in the leading edge radius. The inaccurate aerofoil profile may influence the drag prediction and larger errors may occur at some angles of attack which have a low drag coefficient. Beyond that range of angles of attack, errors of drag coefficient can be controlled to be less than 85%.

4.2 Aerodynamic performance comparison between NREL S809 and DU93-W- 210

Based on previous results, aerofoils were simulated between a wide range of angles of attack (-20° to 90°) to observe the optimum and critical angle of attack. The critical angle of attack is defined as the angle of attack which produces maximum lift. Below the critical angle of attack, lift increases when angle of attack increases.
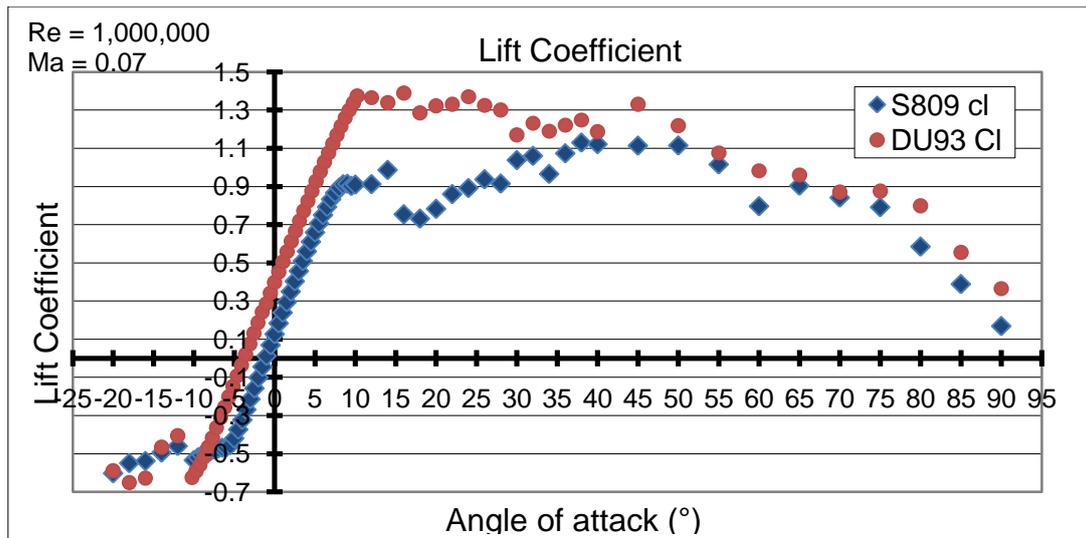
Figure 4-5 Comparison of lift coefficient between S809 and DU93

Figure 4-5 shows that for both aerofoils, lift coefficient is negative at -20°, and then it is increased due to the AoA increasing. The lift coefficient is zero when angles of attack are at -3.6° and -0.5° for the DU93 and S809 aerofoils, respectively. Lift coefficient keeps growing until it reaches to the critical angle of attack. The critical angles of attack are 14° of the S809 aerofoil and 16° of the DU93 aerofoil, respectively. Beyond this angle, the polar curve of lift coefficient has an obvious drop. When the AoA increases, aerofoils begin to stall. Moreover, if wind turbine blades are still in this stall condition, noise is increased significantly and wind turbine vibration occurs. After a sharp decline, the lift coefficients of both aerofoils raise again. After 45° for the DU93 aerofoil and 50° for the S809 aerofoil, the lift coefficient drops down all the way.

It is obvious that DU93 aerofoil always has a higher lift coefficient and lower drag coefficient than S809 under the same AoA. This is because a high curvature of mean camber line leads an increased airflow on upper face, so under the same AoA, DU93 aerofoil has a higher lift coefficient than the S809 aerofoil.
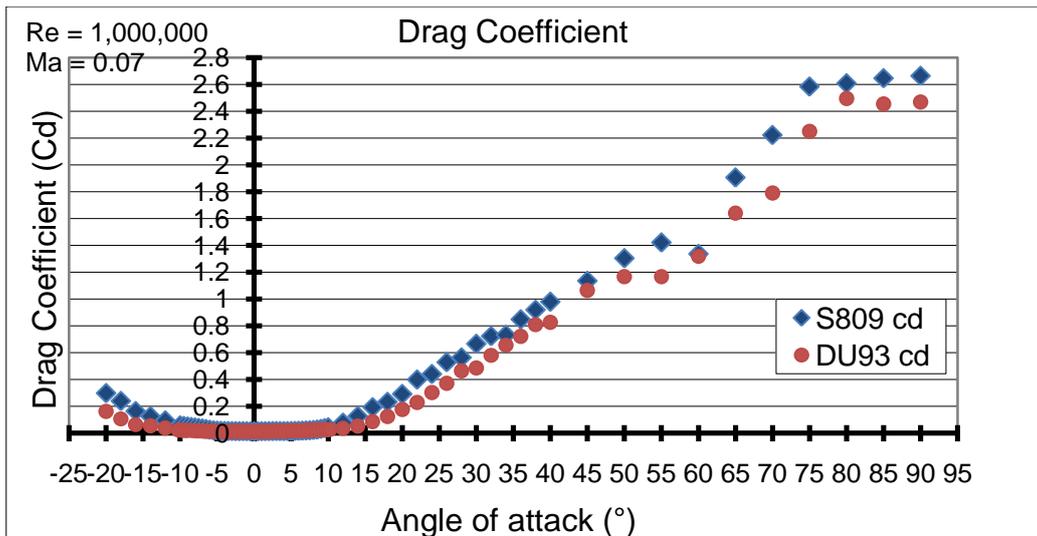
Figure 4-6 Comparison of drag coefficient between S809 and DU93

Figure 4-6 shows when the angle of attack is increased from -20° to 0°, the drag coefficient of both aerofoils decreases. Thereafter, the values increase as the AoA increases in positive direction. For both aerofoils, the minimum drag coefficient of both aerofoil is nearly zero when the angle of attack is 0°. From 15°, the value increases significantly. The maximum drag coefficient for S809 is 2.665 and DU93 is 2.47, it also happens at the same angle of attack which is 90°.

Figure 4-6 shows that from -10° to 15°, the drag coefficient maintains in a low value level before it rises dramatically. At the same time, before aerofoil gets into the stall condition, the lift coefficient always maintains a high value where the optimal angle of attack can be found by plotting the lift to drag ratio.

Figure 4-7 Relationship between lift to drag ratio and angle of attack

The optimal angle of attack is where C_L/C_D (lift and drag coefficient) has the maximum value. Figure 4-7 shows the optimal AoA of the DU93 aerofoil is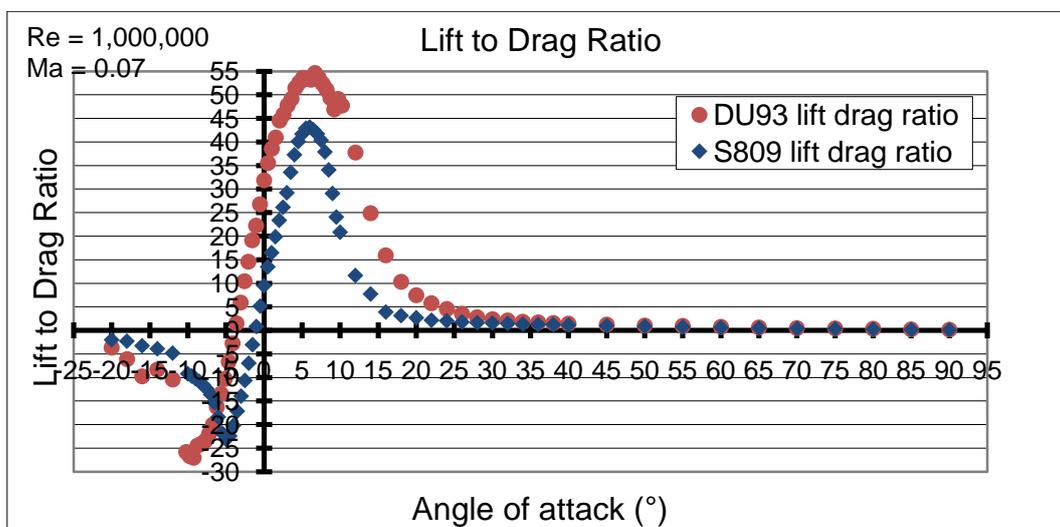 7.2° where lift to drag ratio is 54.62 and the S809 aerofoil is 6° where lift to drag ratio is 43.17. Comparing the two polar curves in Figure 4-7, the region of high lift to drag ratio of the DU93 aerofoil is wider than the S809 aerofoil, which means high lift can be generated in a wider range of angles of attack, and for wind turbine blades (especially a stalled control blade), it can delay stall and produce a high wind energy utilization coefficient.

In order to compare the stall performance, two aerofoils were mounted at the same angle of attack to see which one has a earlier air separation than the other. The simulated angles of attack were -10°, 0°, 10°, 14° and 30°.
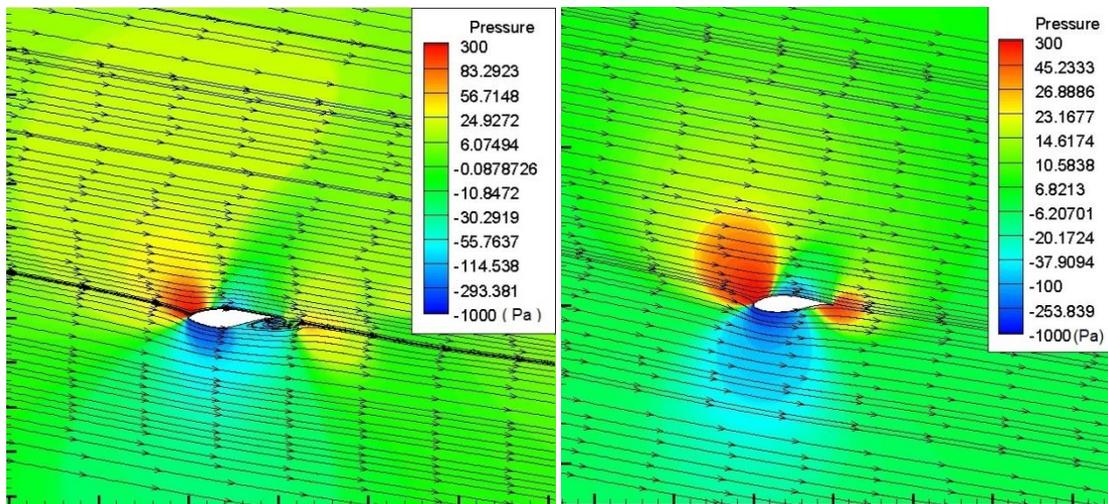
Figure 4-8 S809 pressure contour at -10°   **Figure 4-9 DU93 pressure contour at -10°**

Figures 4-8 and 4-9 show when AoA is as low as -10°, air flow becomes separated on the lower surface near the trailing edge of the S809 aerofoil, but it still attaches to the surface of the DU93 aerofoil. The maximum pressure locats near the leading edge of upper face on both aerofoils.
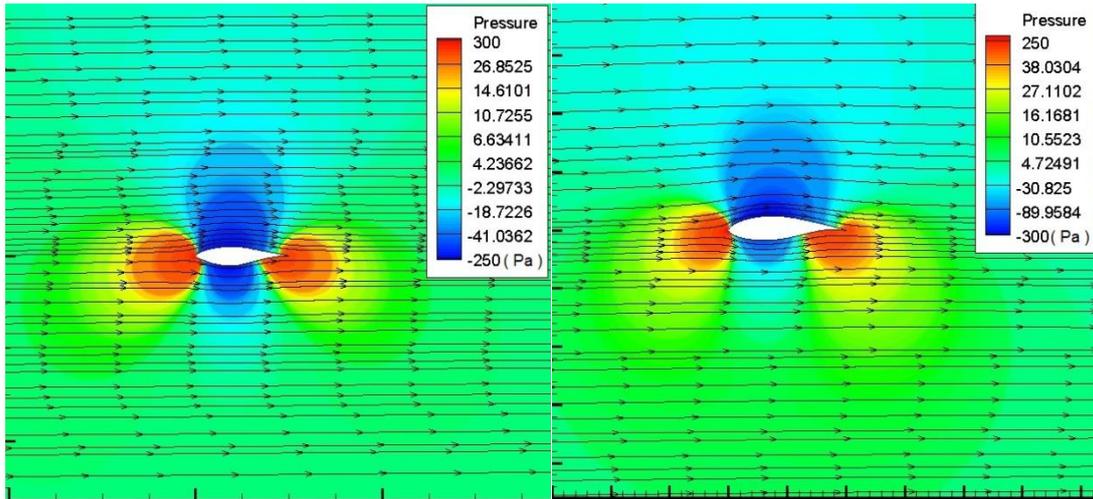
Figure 4-10 S809 pressure contour at 0°   **Figure 4-11 DU93 pressure contour at 0°**

Figures 4-10 and 4-11 show when AoA is 0°, the air flow attaches to both aerofoil surfaces and the maximum pressure is located at the leading and trailing edges.
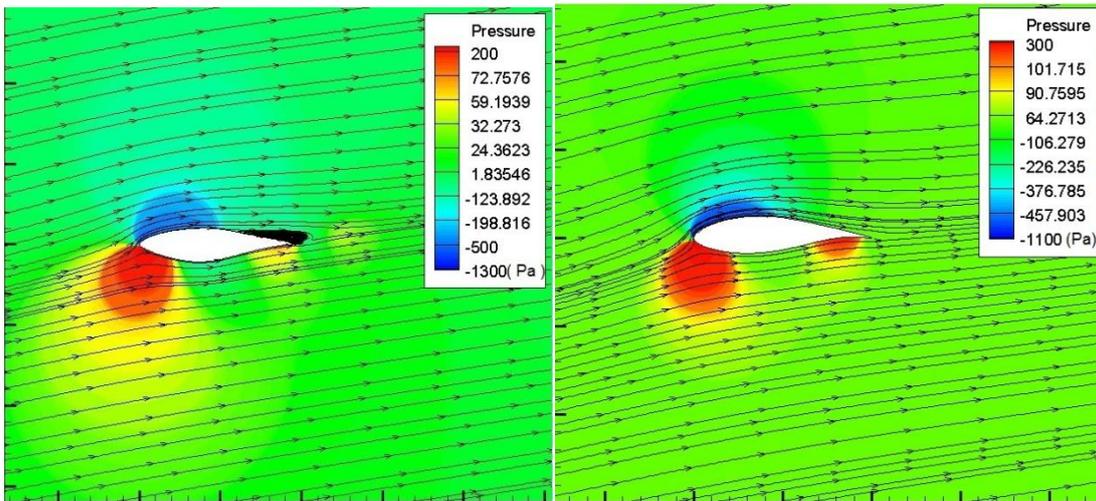
Figure 4-12 S809 pressure contour at 10°   **Figure 4-13 DU93 pressure contour at 10°**

Figures 4-12 and 4-13 show when AoA is pitched to 10°, the separation point occurs at the trailing edge of the S809 aerofoil but air flow is still attached to the surface of the DU93 aerofoil. Comparing this with Figures 4-8 and 4-9, the maximum pressure point moves to near the leading edge of lower face on both aerofoils.
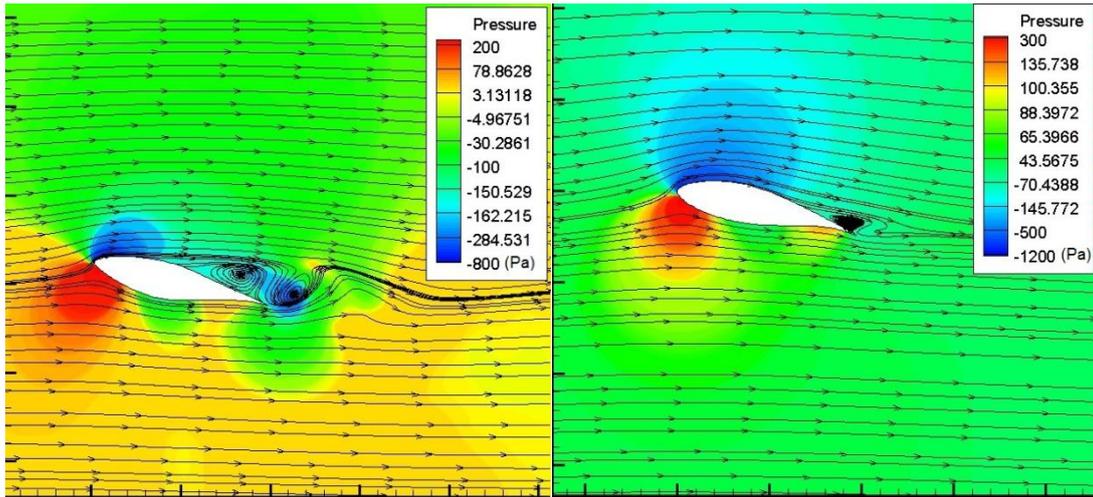
Figure 4-14 S809 pressure contour at 14°   Figure 4-15 DU93 pressure contour at 14°

Figures 4-14 and 4-15 show when AoA is increased to 14°, the separation point in the S809 aerofoil moves forward to the leading edge, at the same time; vortex shedding happens on the trailing edge. In contrast, on the trailing edge of the DU93 aerofoil only separated flow occurs.
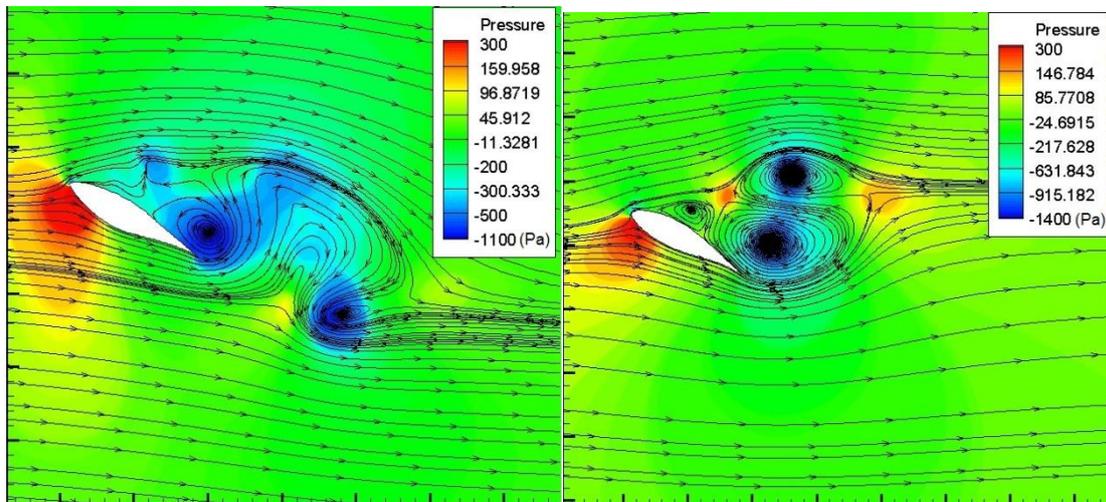
Figure 4-16 S809 pressure contour at 30°   Figure 4-17 DU93 pressure contour at 30°

Figures 4-16 and 4-17 shows vortex shedding occurs near the leading edge at 30°. This leads the air flow not to be attached to the upper face of the aerofoils anymore. Aerofoils have already reached the stall condition at this angle. From Figure 4-8 to 4-17, it is clear to see the air flow separation on the DU93 aerofoil is slower than the S809 aerofoil.

In AYSYS-Fluent, separation point can be found by showing the wall shear stress. It takes place when airflow on the surface leaves the aerofoil.
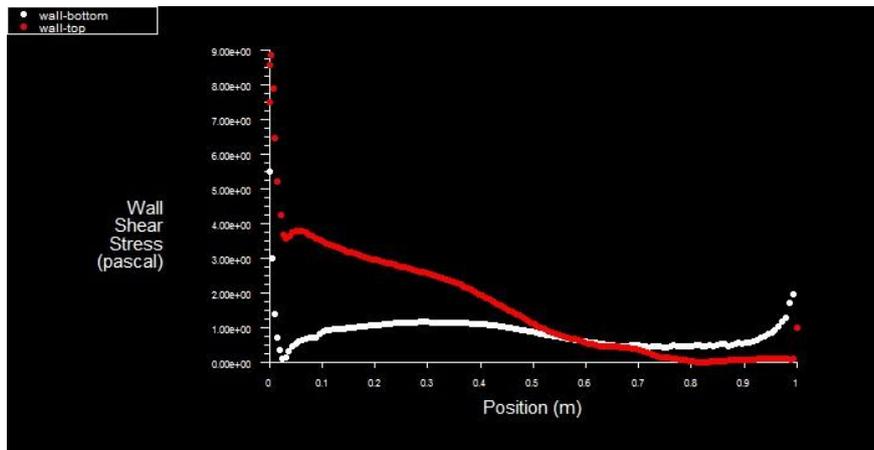
Figure 4-18 Wall shear stress of DU93 at 10°

Figure 4-18 shows that the separation point takes place when wall shear stress vanishes. Moreover, when the angle of attack is 10°, separation point occurs on the upper face of the aerofoil and locates at approximately 80% chord length from leading edge.
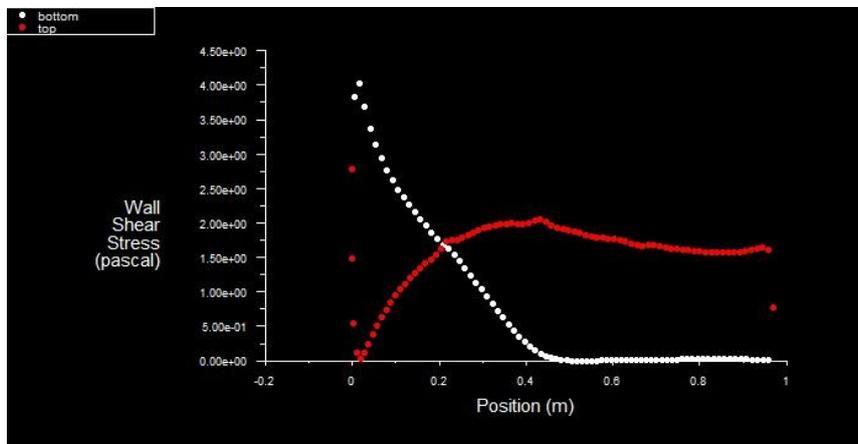
Figure 4-19 Wall shear stress of DU93 at -14°

Conversely, it occurs on the lower face when angle of attack is negative, Figure 4-19 shows when the angle of attack is -14°, separation point locates at approximately 50% chord length from leading edge.

Figures 4-18 and 4-19 indicate that the separation point changes with the variation of angle of attack. Based on this point, separation points on DU93

aerofoil and S809 aerofoil can be compared to see which one has a better stall performance.
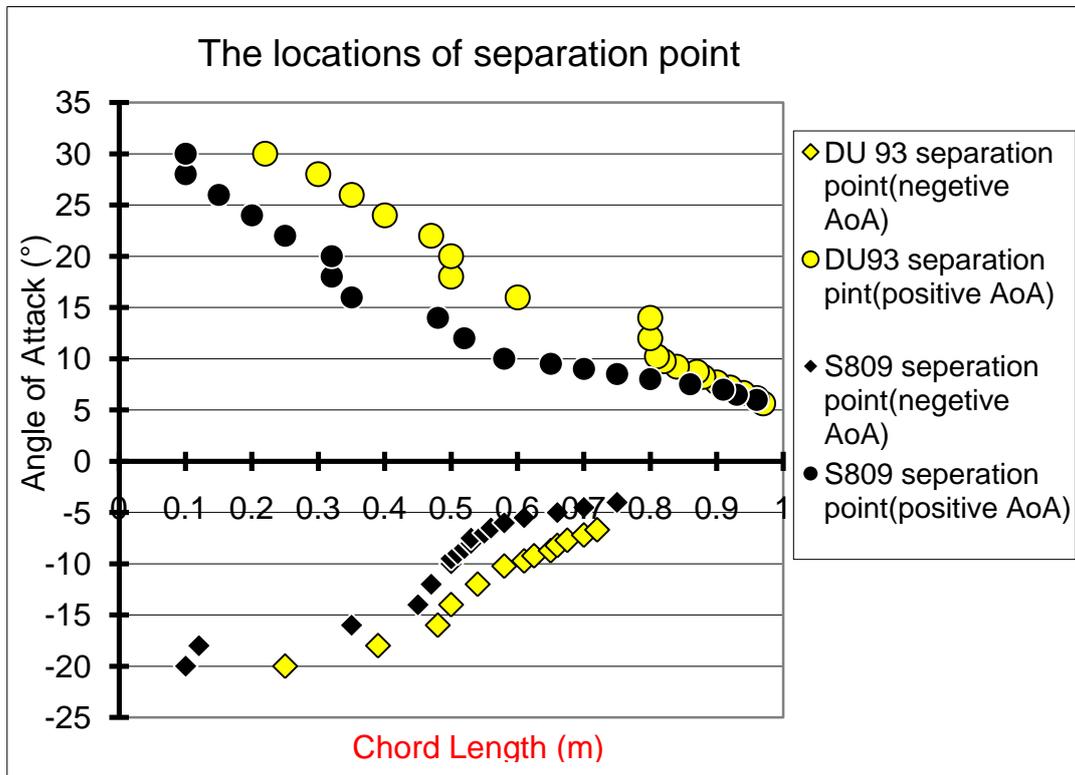
Figure 4-20 Separation point locations of S809 and DU93

Figure 4-20 shows the locations of the separation point on S809 and DU93 aerofoil, respectively. It occurs on the lower face when AoA is negative and on the upper face when AoA is positive. When the angle of attack is positive, the airflow separation occurs at 8° on both aerofoils. From 14° to 16°, the separation point move rapidly on both aerofoils. At 14°, separation point locates at the upper face and 80% chord length of the DU93 aerofoil. It also locates at the upper face but 48% chord length of the S809 aerofoil. At 16°, separation point moves forward from 80% to 60% chord length on the DU93 aerofoil and from 48% to 34% chord length of the S809 aerofoil. Based on the prediction of lift coefficient, it is known that both aerofoils get into the stall condition at 16°, so under this condition; not only the lift coefficient drops dramatically but also the airflow separation points moves significantly. When the AoA is 30°, the separation point locates at approximately 10% chord length of the S809 aerofoil but 24% chord length of the DU93 aerofoil. However, when the angle of attack is negative, separation point occurs at -5°

on S809 but -8° on DU93, when AoA is -20°, separation point moves to approximately 10% of the chord length on the S809 aerofoil and 22% on the DU93 aerofoil.

By observing the airflow pass these aerofoils, it is clear to see DU93 has a better stall performance by comparing than the S809 aerofoil, because the stall condition will begin when the separation point is moving forward to the leading edge. Figure 4-20 shows the separation point on the DU93 aerofoil moves slower than the S809 aerofoil, so the critical angle of attack of DU93 aerofoil is higher than S809 aerofoil.

4.3 Wind turbine power output prediction

There is a power loss when the mechanical power transfers to the generator power. Mechanical power can be calculated by using the equation from ANNEX XIV report (Thumthae and Chitsomboom (2006, p.2):

$$P_{Generator} = 0.78 P_{Mechanical}$$ (Equation 4-1)

Duque N.P., $\mathrm{et.al}$ (2000) found that this equation is not perfectly correct. They proposed a new correlation which is:

$$P_{Generator} = 0.9036 P_{Mechanical} - 0.847$$ (Equation 4-2)

Compared with original correction, the better accuracy has been proved with Thumthae and Chitsomboom (2006, p.3). The nominal generator power of the simulated wind turbine is 10 kW, in order to keep it in a stable value, mechanical power should be limited between the ranges of 11.5 kW to 12 kW.

To validate the numerical model, the overall performances of wind turbine are computed and compared to BEM theoretical calculations. Figure 4-21 and Figure 4-22 show the torque and mechanical power as a function of the wind velocity.
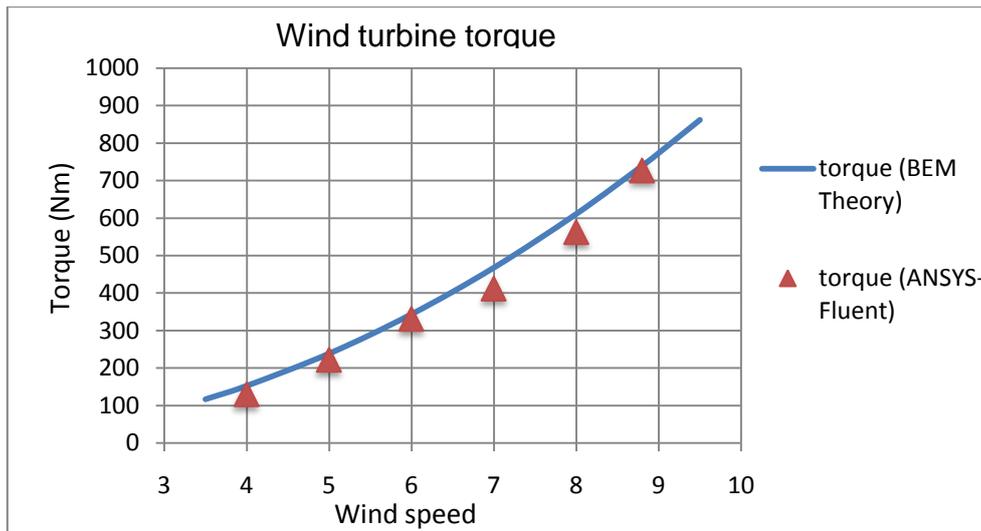
Figure 4-21 Torque errors between theory and ANSYS-Fluent for different wind speed
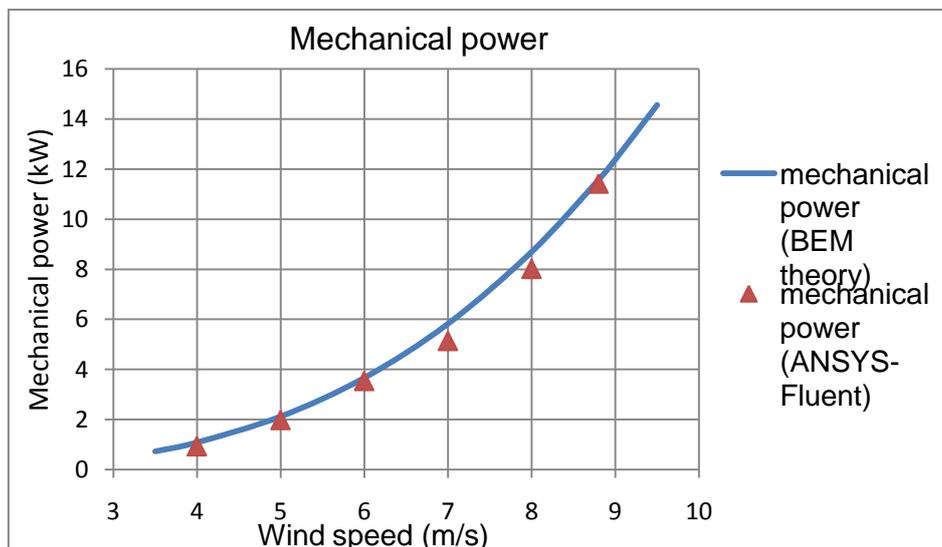
**Figure 4-22 Mechanical power comparisons between theory and CFD calculations
under different wind speeds**

ANSYS-Fluent has a good correlation with theoretical value for different wind velocities. The mechanical power is increased dramatically while wind speed changes from 8 to 8.8 m/s. When wind velocity reaches 9.5 m/s, theoretical mechanical power is 14.56 kW. By using Equation 4-2, the generator output power would be 12.31 kW. High rotational speeds and output power may lead to a high temperature in the generator. It may catch fire when the generator runs with a high rotational speed for a long time. The efficient way to control the output power is reducing the rotational speed of blade.

59

Wind speed (m/s)	Rotational speed (rpm)	Tip speed ratio	Torque (Nm)	Mechanical Power (kW)
9.5	162	8	867.458	14.716
9.5	140	6.94	788.512	11.7

Table 4-1 Tip speed ratio variations

It is clear to see from Table 4-1; under the same wind speed, torque is reduced by decreasing the tip speed ratio. Hence, tip speed ratio variations can be used to change the rotor output power and thereby the rotor torque. According to Equation 2-7, torque and rotational speed have an inverse relationship under a fixed mechanical power; decreasing the rotational speed will keep a constant output power. In order to predict the wind turbine output power, simulation is carried out under a wide wind speed range (from 3 to 18 m/s).
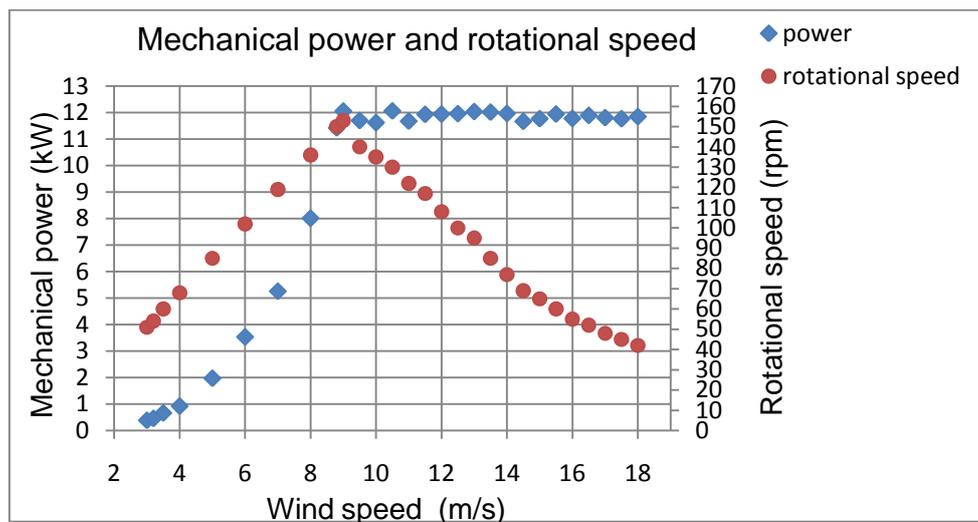
Figure 4-23 Diagram of mechanical power and rotational speed

Based on Equation 2-4, before nominal wind speed, rotational speed of rotor blade has to increase in order to maintain the constant tip speed ratio. Figure 4-23 indicates that the maximum rotational speed is 150 rpm when wind speed is 8.8 m/s, after that, a reasonable decrease of rotational speed can retain the 12 kW power output. The minimum rotational speed is 40 rpm when wind speed is 18 m/s.
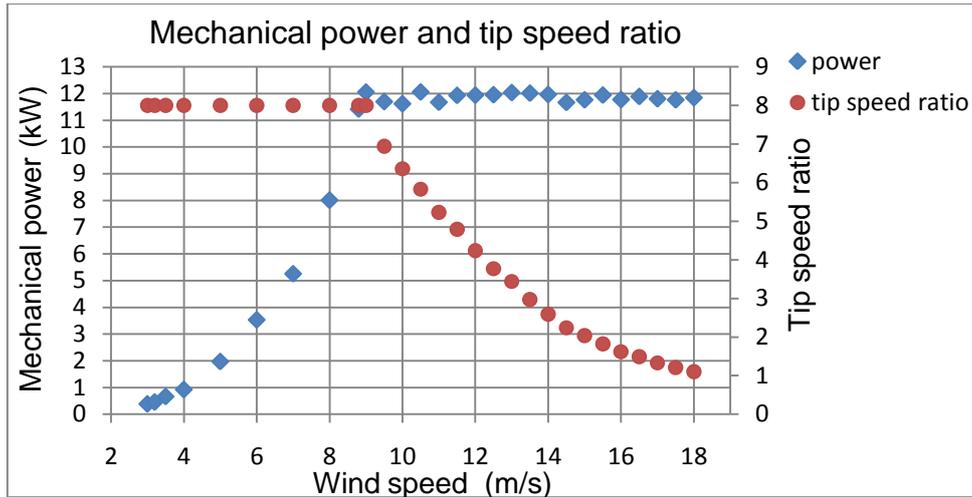
Figure 4-24 Diagram of mechanical power and tip speed ratio

Figure 4-24 shows the diagram of mechanical power and tip speed ratio. Before it reaches to the rated wind speed (8.8 m/s), the mechanical power increases as the wind speed increases. The tip speed ratio is kept constant at 8. After that, the decrease of rotational speed leads a declination of tip speed ratio curve. The minimum tip speed ratio is 1.1 when wind speed is 18 m/s.
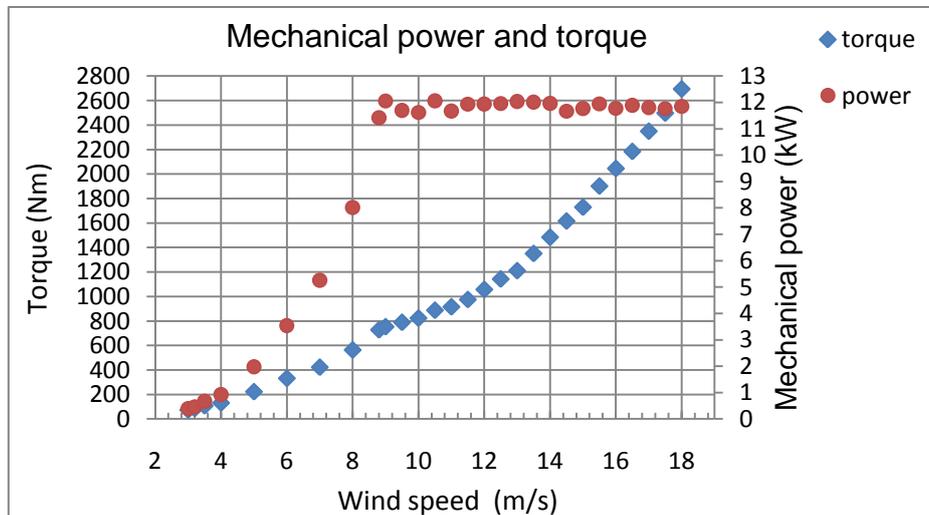
Figure 4-25 Diagram of power and torque

Figure 4-25 shows although the mechanical power can be kept constantly when wind speed exceeds over 8.8 m/s, yet the torque is still increasing. This phenomenon can be explained by using Equation 2- 15: in order to achieve a stable power output, the decrease of rotational speed leads the increase of torque.

61

The power coefficient Cp (Equation 4-3) is one of the crucial factors in wind turbine design; a high power coefficient means wind turbine can extract more energy from the wind (R.Lanzafame and M.Messina, 2006).

$$C_p = \frac{P}{\frac{1}{2}\rho Vo^3 \pi R^2}$$ **(Equation 4-3) (Varol, et al., 2001)**
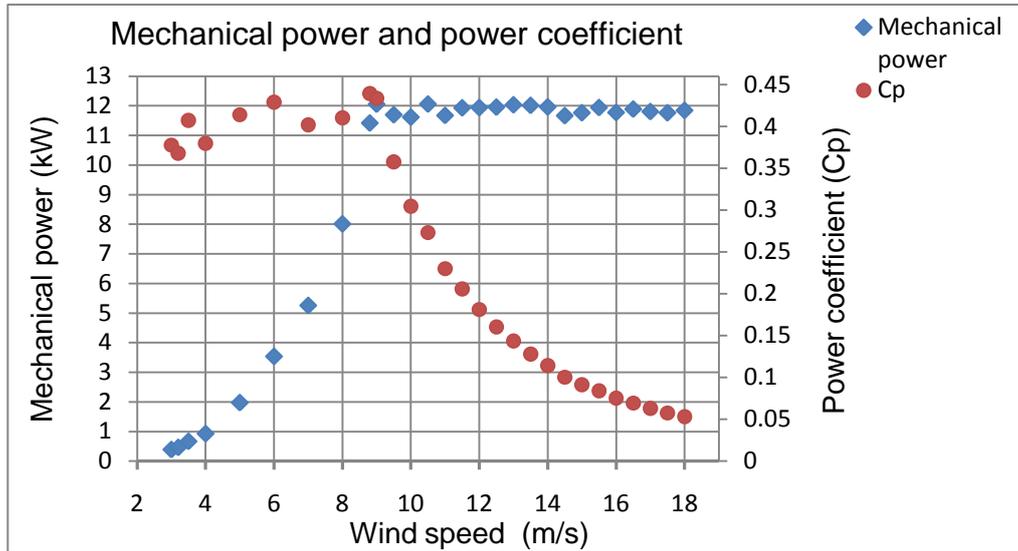
Figure 4-26 Diagram of mechanical power and power coefficient

Figure 4-26 shows the maximum power coefficient is 0.439 where the wind speed is 8.8 m/s, the power coefficient drops dramatically once the tip speed ratio decreases. When wind speed reaches to 18 m/s, the value of power coefficient is only 0.053

4.4 Rotational effect of wind turbine with original blade

As the wind turbine rotates, vortexes shed from hub and blade tips which form a helical vortex wake; the spin in the wake is opposite to the torque of the rotor in order to maintain the angular momentum (Hau, 2006, p.105). Tip and hub losses will occur when the wake happens, so the power coefficient of the turbine must be smaller than the Betz limit. In general, the extra kinetic energy in the wind turbine wake will be higher if the generated torque is higher (Manwel el al., 2002, p.89), so with the same output power, wind turbine with high tip speed ratio can extract more kinetic energy from wind comparing with low tip speed ratio wind turbine and this phenomenon is shown in Table 4-2.

$\lambda = \omega R/V_o$	$27C_p/16$
0.5	0.486
1.0	0.703
1.5	0.811
2.0	0.865
2.5	0.899
5.0	0.963
7.5	0.983
10.0	0.987

Table 4-2 Glanert's comparison of the computed optimum power coefficient including wake rotation with the Betz limit

Table 4-2 indicates that when the tip speed ratio is increased, the power coefficient approaches to the Betz limit. What's more, the power loss is small when tip speed ratio reaches to 5.

The expansion of the wake behind a wind turbine can be described as:

$$D_x = (\beta^{n/2} + k \times s)^{1/n} D_0 \quad \text{(Equation 4-4)} \quad \text{(Méchali, et al., 2004)}$$

Where $s = x/D_0$, the solution for n has been suggested as 3 by e.g. Schlichting (1968), k is the decay constant, according to the Wind Atlas Analysis and Application Program (WAsP)'s experience, the default value k = 0.075 is reasonable in most land-cases, for off-shore cases, WAsP recommend to use a lower limit of k = 0.04. β is the initial wake expansion and described as:

$$\beta = \frac{0.5 \times (1 + \sqrt{1 - C_T})}{\sqrt{1 - C_T}} \quad \text{(Equation 4-5)}$$

$$C_T = \frac{2T}{\rho \frac{\pi}{4} D_0^2 V_0^2} \quad \text{(Equation 4-6)}$$

Wind speed (m/s)	x (m)	Dx (m)	Wind speed (m/s)	x (m)	Dx (m)
3.5	10	10.55	8.8	10	10.79
	20	10.73		20	10.99
	30	10.95		30	11.18
	40	11.41		40	11.36
	50	11.33		50	11.54
	60	11.51		60	11.71
	70	11.68		70	11.88
	80	11.85		80	12.04
	90	12.01		90	12.20
	100	12.17		100	12.36

(Note that: x is downwind horizontal distance between the wind turbine, Dx is wake diameter on the downwind horizontal distance between the wind turbines)

Table 4-3 wake expansion under the different wind speeds

The wake expansion can be calculated by using Equation 4-4, Table 4-3 shows that wake diameter is proportional to the downwind distance between the wind turbine. When the downwind distance between wind turbine is 100 m, the wake diameter is 12.17 m at 3.5 m/s. Meanwhile, the wake diameter is 12.36 m at 8.8 m/s.

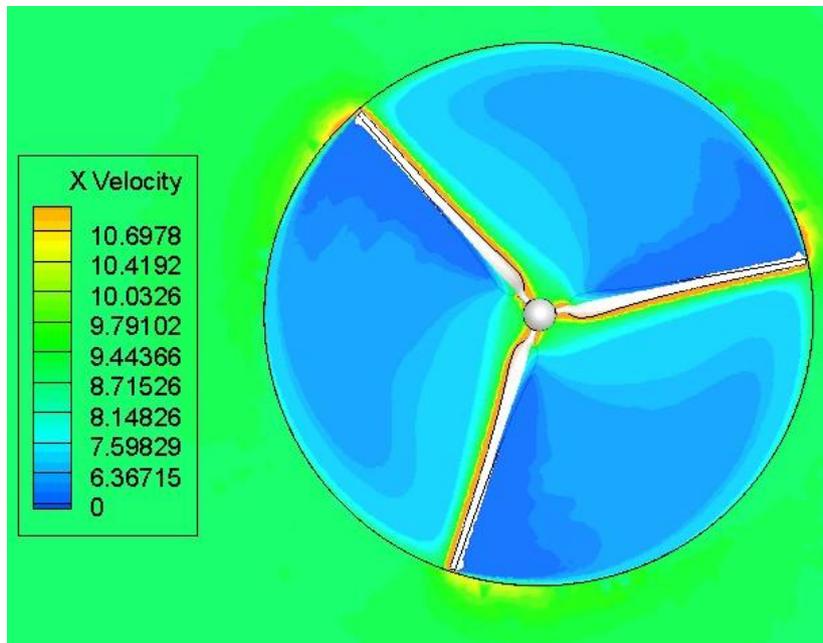**Figure 4-27 Contour of axial velocity in wind turbine rotational plane at 8.8 m/s wind speed**

Figure 4-27 shows the leading edge has a high axial velocity when rotor blades begin to rotate. Meanwhile, a low axial velocity is located behind the trailing edge. The wake cylinder is formed once the wind turbine blades rotate.
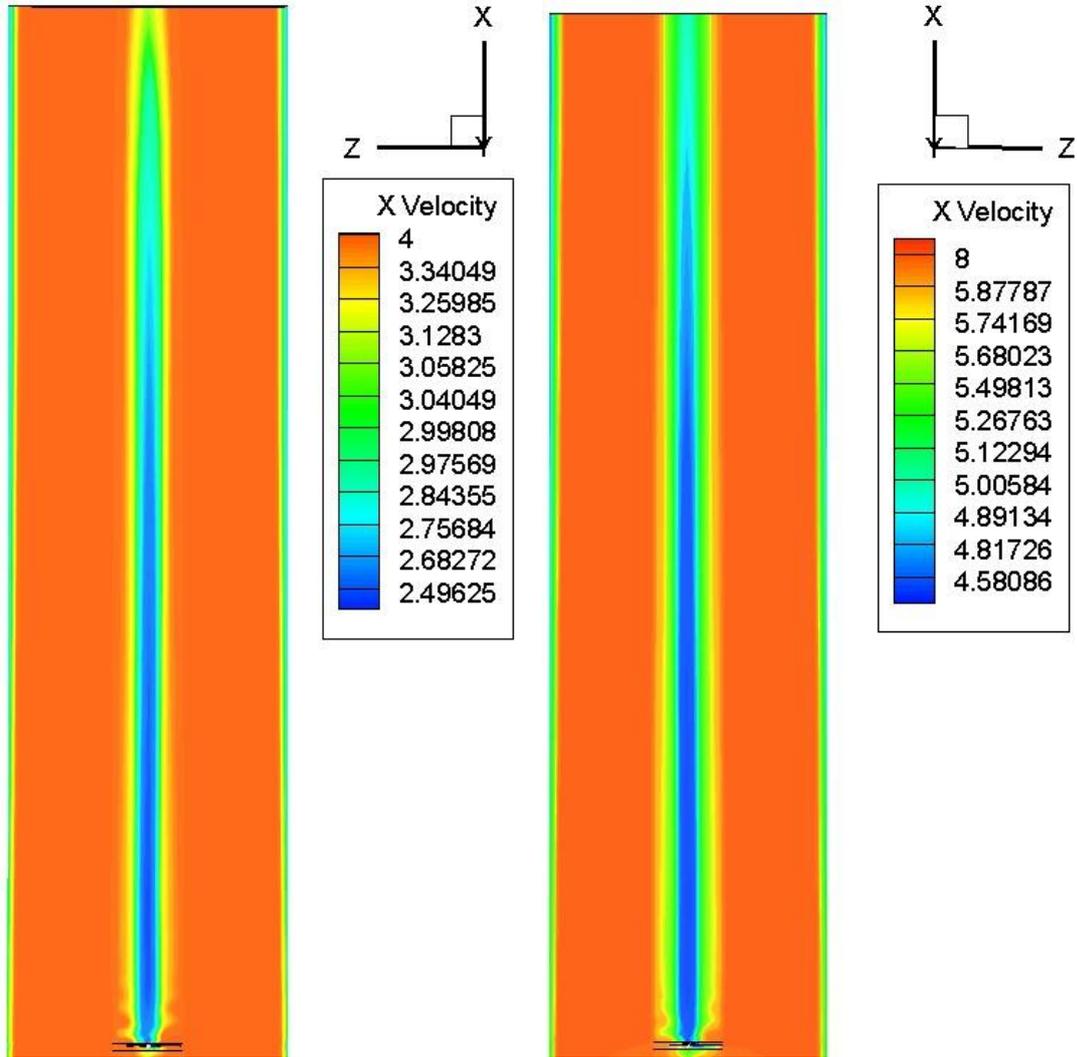
Figure 4-28 Wind turbine wake at 3.5 m/s   **Figure 4-29 Wind turbine wake at 6 m/s**
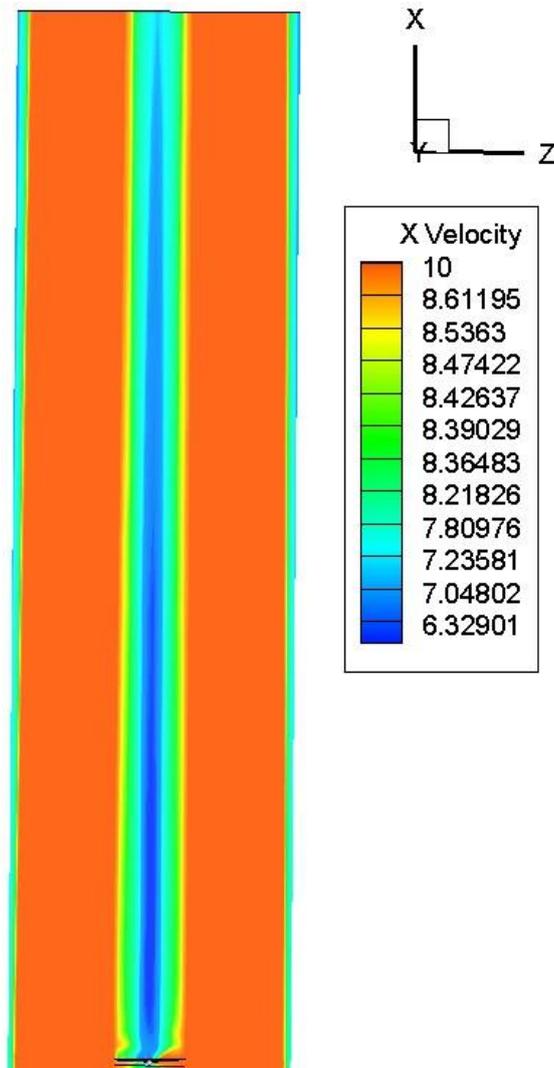
Figure 4-30 Wind turbine wake at 8.8 m/s

Figure 4-28 is the wind turbine wake at 3.5 m/s. it shows that in the wake region, the axial velocity is smaller than the ambient environment. The minimum axial velocity is located behind the hub which is the blue area. Far behind the wind turbine, the axial velocity in wind turbine wake is increased and becomes equal to the ambient velocity. Figure 4-29 is the wind turbine wake at 6 m/s. The wind turbine wake has a longer and wider low velocity region in comparison to Figure 4-28. Figure 4-30 is the wind turbine wake at 8.8 m/s, the wake expansion is more obvious than previous two figures. Three figures indicate that when wind speed increases, high rotational speed leads a longer wind turbine wake and more distinct velocity drop.

In a wind farm, if wind turbines are placed close to each other, then the wake interaction will cause a number of consequences: firstly, due to the decreasing of wind speed in wake, the output power of subsequent wind turbine will be reduced. Méchali, et al. (2007) demonstrate if wind turbines are placed in a row, the largest relative power drop is from the first turbine to the second turbine, which the second turbine may lose 20% to 30% output power. Secondly, the turbulence in the rotor wake increases causing turbulence loading on the downwind turbines which will consequently cause the material fatigue (Hau, 2006, p.117) and reduces the life time of the wind turbine.
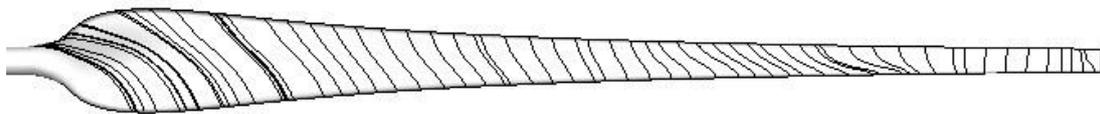
Figure 4-31 Streamline on suction side of blade at 3.5 m/s wind speed
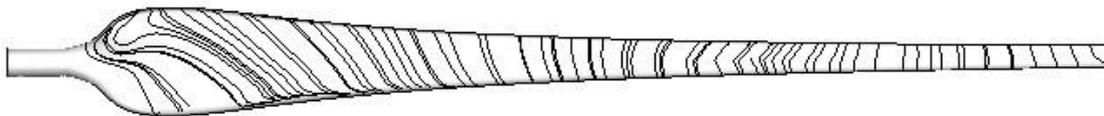
Figure 4-32 Streamline on suction side of blade at 6 m/s wind speed
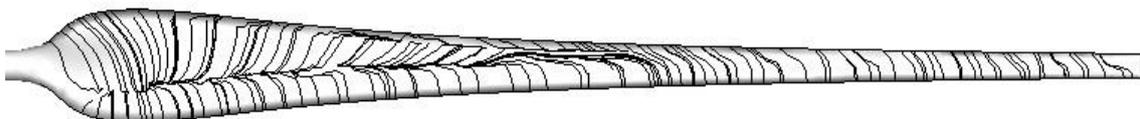
Figure 4-33 Streamline on suction side of blade at 8.8 m/s wind speed

A depiction of air flow on the blade surface is given by plotting the streamlines. Figures 4-31, 4-32 and 4-33 show the air flow can align with the blade under a low wind speeds. Air flow can attach the blade when wind speed are 3.5 and 6 m/s. Then, when wind speed reaches to 8.8 m/s, the air separation occurs from the root area and extends to the middle section of the blade. A separation line can be seen in Figure 4-33, but air flow still attaches to the blade outward section.

4.5 Comparisons of different blade geometries

The inspiration of innovated root design comes from Enercon E-70 (Figure 4-34) (71 m rotor diameter), which can produce 2300 kW power output under the nominal wind speeds. Rohden (2004) stated this new blade generates an increased yield of 12%-15% in comparsion with E-66 (70 m rotor diameter) wind turbine. In this section, different blade geometries will be compared for predicting the power output.

Figure 4-34 Enercon E-70

Wind speed (m/s)	Rotational speed (rpm)	Rotor design	Torque (Nm)	Mechanical power (kW)	C_P
3.5	60	Rectangular tip	106.290	0.666	0.407
		Innovated root	109.826	0.684	0.418 (+2.7%)
Wind speed (m/s)	Rotational speed (rpm)	Rotor design	Torque (Nm)	Mechanical power (kW)	C_P
6	102	Rectangular tip	331.097	3.536	0.429
		Innovated root	358.387	3.823	0.464 (+8.1%)
Wind speed (m/s)	Rotational speed (rpm)	Rotor design	Torque (Nm)	Mechanical power (kW)	C_P
8.8	150	Rectangular tip	727.086	11.421	0.439
		Innovated root	811.291	12.739	0.49 (+11.5%)

Table 4-4 Torque and mechanical power comparisons of different blade geometries

68

As seen in Table 4-4, innovated root has a significant effect on power increasing, especially under a high wind speed condition (8.8 m/s). This innovated root design allows 11.5 percent increase of the power coefficient.

4.6 Aerodynamic noise prediction

Mechanical and aerodynamic noises are the main sources of noise from wind turbines. Mechanical noise is generated mainly from gearbox and generator; it may also come from cooling fans and other auxiliary equipment (Burton, et al., 2001, p.531). Arakawa, et al. (2005, p.11) stated aerodynamic noise consists of low frequency and high frequency broadband noises. In this section, ANSYS-Fluent is used in order to predict the amount of noise generated when different tips are used in the design of wind turbine blades.

4.6.1 Near- to far-field aerodynamic noise predicting under the different wind speeds

In ANSYS-Fluent, the near- to far-field aerodynamic noise can be calculated by mounting receivers at different position and the setting has been introduced in section 3.5.1. The simulated results of aerodynamic noise of rectangular and tapered tip are shown in Tables 4-5 and 4-6.

Tip design	Wind speed	Rotational speed	Receiver 1 134 m	Receiver 2 90 m	Receiver 3 45 m	Receiver 4 0 m	Receiver 5 -70 m
Rectangular tip	3.5 m/s	60 rpm	26.62 dB	30.07 dB	36.08 dB	81.89 dB	32.06 dB
	6.0 m/s	102 rpm	30.89 dB	34.33 dB	40.29 dB	90.25 dB	36.2 dB
	8.8 m/s	150 rpm	38.2 dB	41.63 dB	47.58 dB	93.69 dB	43.47 dB

Table 4-5 Aerodynamic noise of rectangular tip from near- to far- field

Tip design	Wind speed	Rotational speed	Receiver 1 134 m	Receiver 2 90 m	Receiver 3 45 m	Receiver 4 0 m	Receiver 5 -70 m
Tapered tip	3.5 m/s	60 rpm	11.95 dB (-55.1%)	15.28 dB (-49.2%)	21.05 dB (-41.7%)	73.97 dB (-9.6%)	17.21 dB (-46.3%)
	6.0 m/s	102 rpm	20.77 dB (-32.8%)	24.21 dB (-29.5%)	30.23 dB (-25%)	83.13 dB (-7.9%)	26.25 dB (-27.5%)
	8.8 m/s	150 rpm	26.13 dB (-31.6%)	29.57 dB (-29%)	35.52 dB (-25.3%)	91.60 dB (-2.2%)	31.43 dB (-27.7%)

Table 4-6 Aerodynamic noise of tapered tip from near- to far-field

Receiver 5 was mounted at the upstream of the wind turbine and rest of them were installed under the downstream of the wind turbine. The location of receiver 4 is on the centre of wind turbine. Table 4-5 and Table 4-6 shows that the aerodynamics noise is increasing as the rotational speed increases. Tapered tip produces less aerodynamic noise than rectangular one and this phenomenon is more obvious under a low wind speed. When the wind speed reaches to 8.8 m/s, the fast rotational speed leads too much aerodynamic noise. The receiver 4 shows the noise generated by rectangular and tapered tip is over 90 dB. In the far-field area, receiver 5 shows tapered tip has a better performance for noise reduction. Experience (Burton, et al., 2001, p.339) suggests that the normal minimum spacing between turbines and residence is 400 m.

4.6.2 **Wind turbine aerodynamic noise**

In ANSYS-Fluent, wind turbine aerodynamic noise can be simulated by using RANS model, the simulated results are plotted from Figures 4-35 to 4-40.
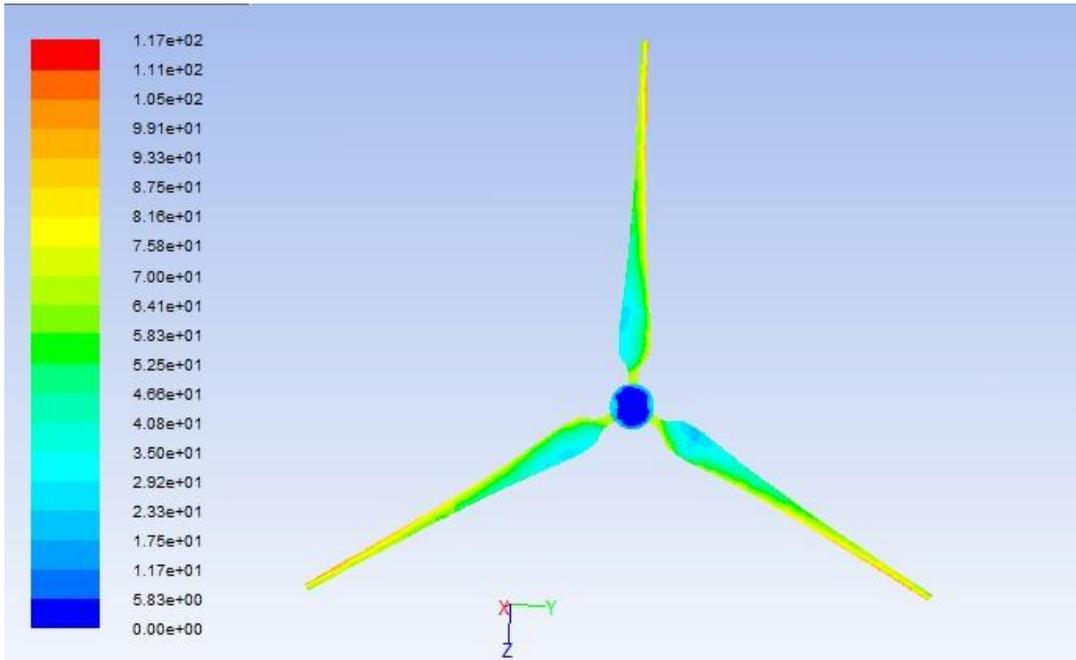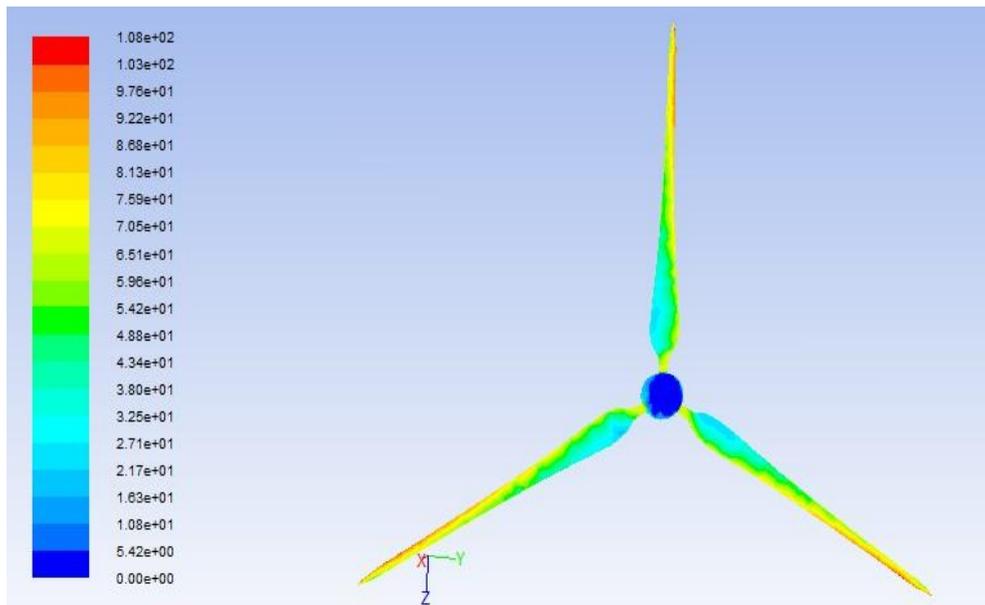
Contours of Acoustic Power Level (dB)
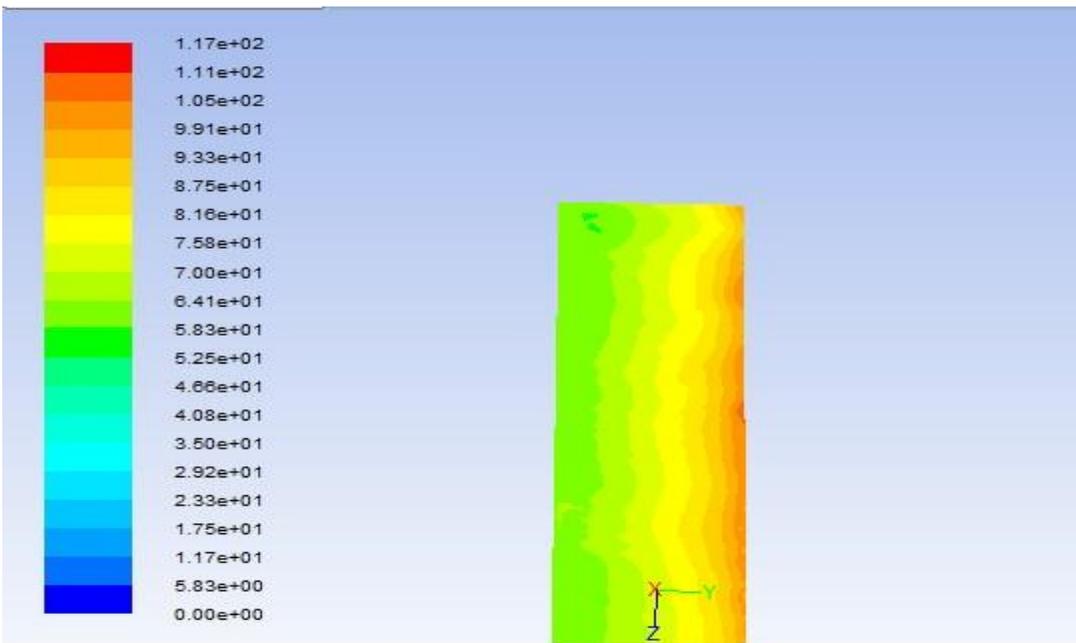
Contours of Acoustic Power Level (dB)

Figure 4-35 Acoustic power of rectangular tip at 3.5m/s

Contours of Acoustic Power Level (dB)

Contours of Acoustic Power Level (dB)

Figure 4-36 Acoustic power of tapered tip at 3.5m/s

Figures 4-35 and 4-36 indicate that when wind speed is 3.5 m/s, the maximum acoustic power is located at the leading edge of both blade tips. The maximum value of rectangular tip is 117dB and tapered tip is 108dB, from blade tip to the root area, the acoustic power value is decreased and the lowest value is at the hub area.
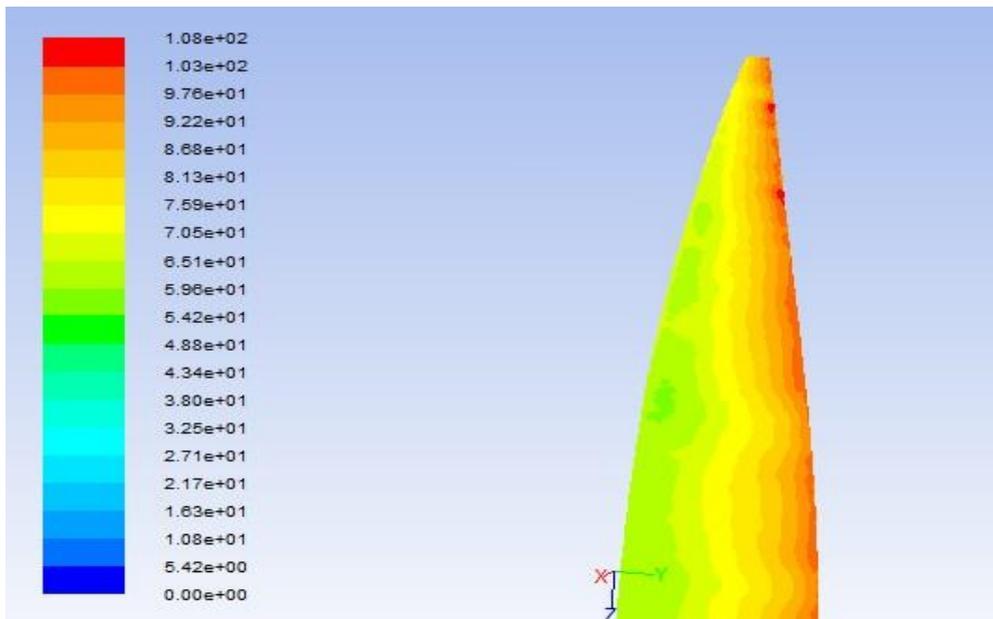
Contours of Acoustic Power Level (dB)

Contours of Acoustic Power Level (dB)

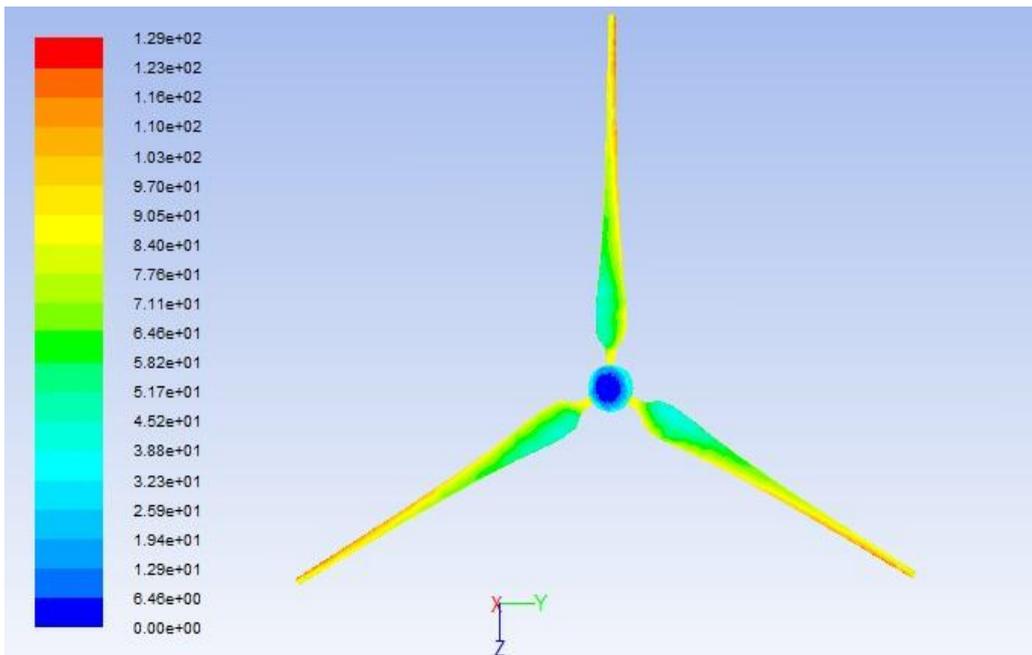**Figure 4-37 Acoustic power of rectangular tip at 6m/s**

Contours of Acoustic Power Level (dB)
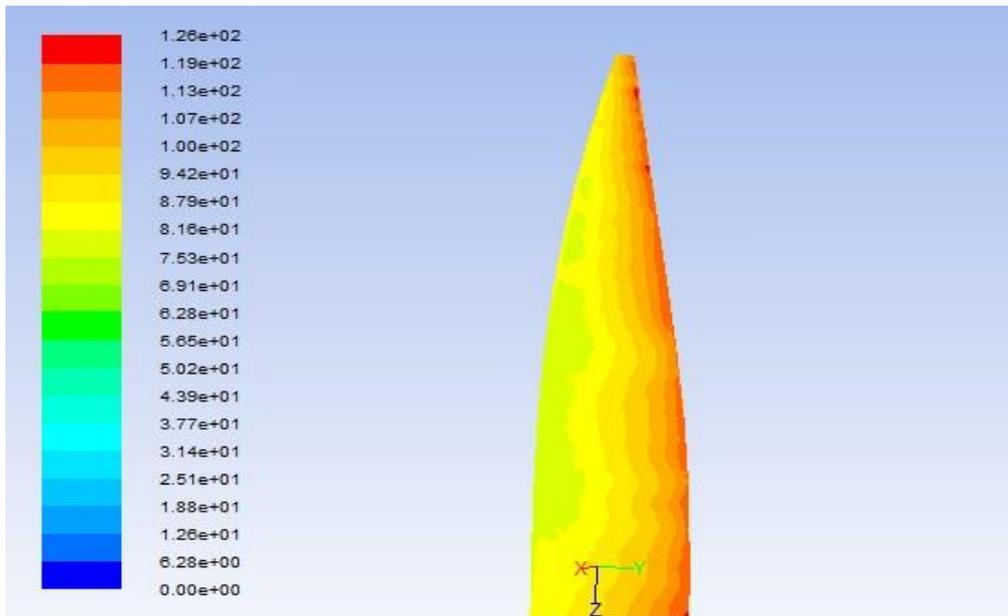
Contours of Acoustic Power Level (dB)

Figure 4-38 Acoustic power of tapered tip at 6m/s

Figures 4-37 and 4-38 show when wind speed is 6 m/s, the maximum acoustic power value of rectangular tip is 129dB and tapered tip is 126dB, as increasing the rotational speed, the low acoustic power area shrinks and concentrates at hub and blade root region.

74
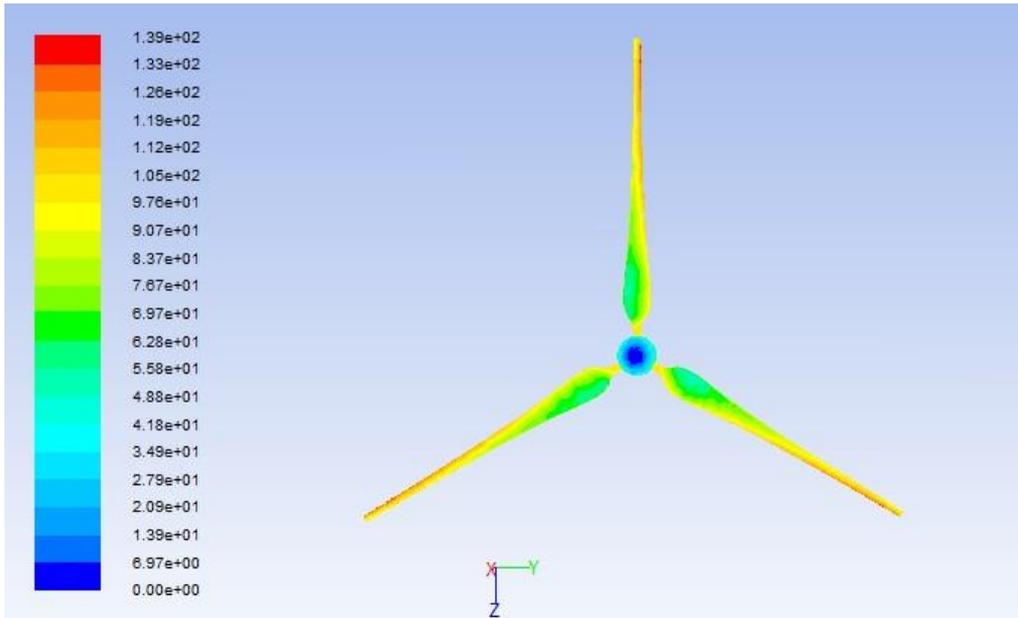
Contours of Acoustic Power Level (dB)

Contours of Acoustic Power Level (dB)

Figure 4-39 Acoustic power of rectangular tip at 8.8m/s

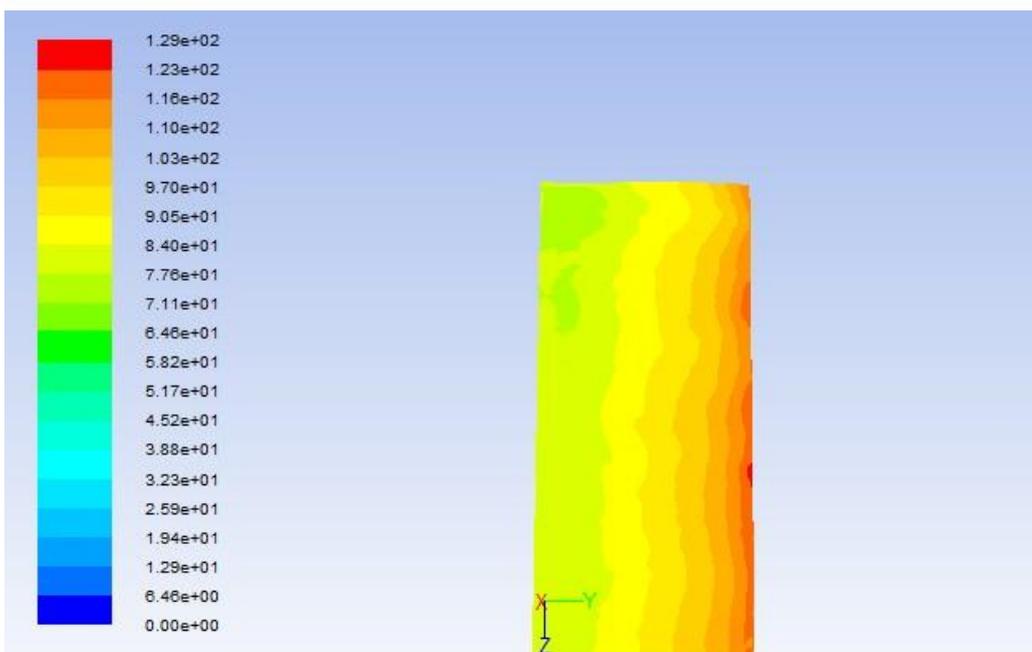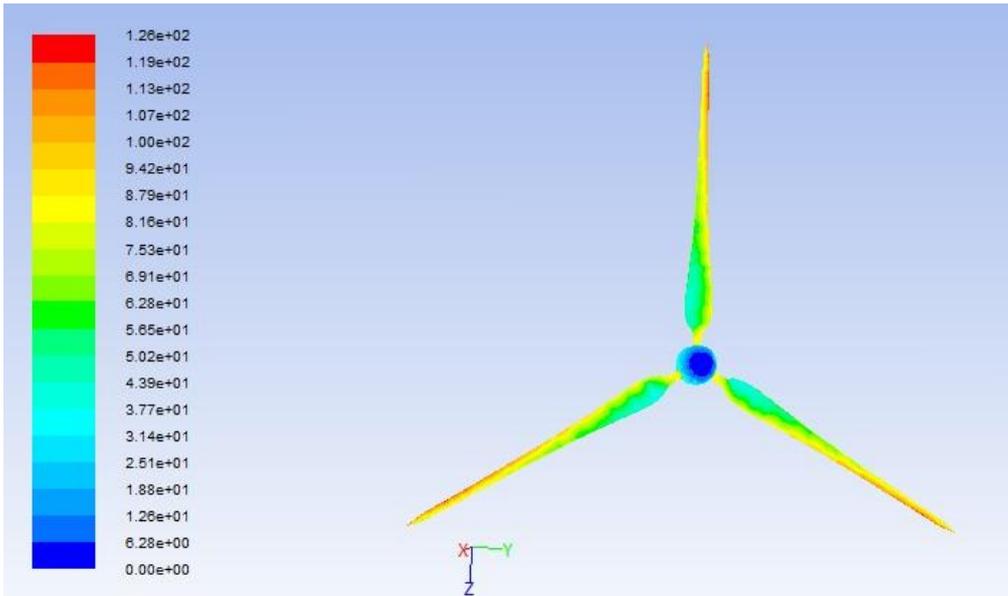Contours of Acoustic Power Level (dB)

Contours of Acoustic Power Level (dB)
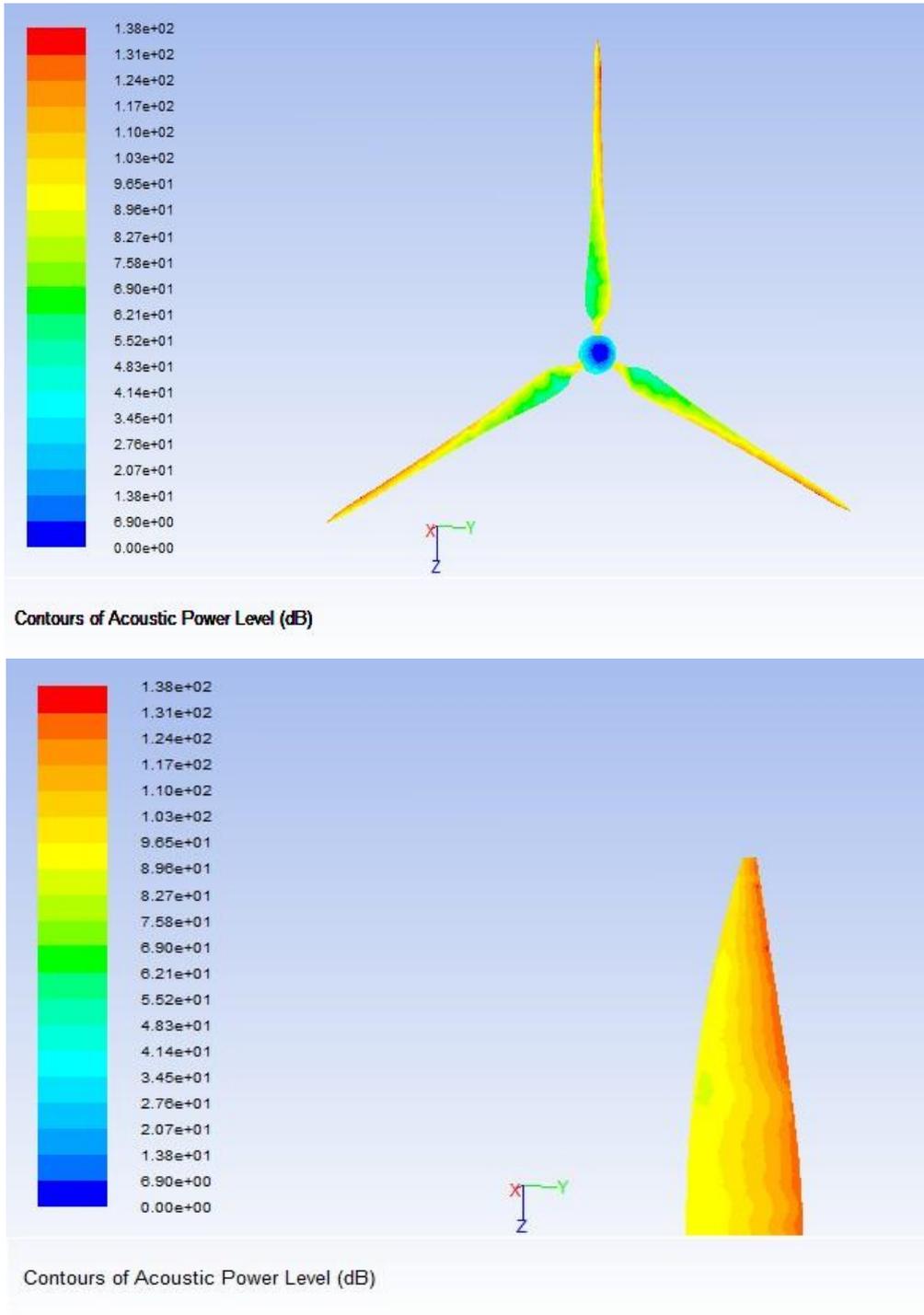
Figure 4-40 Acoustic power of tapered tip at 8.8m/s

Figures 4-39 and 4-40 show when wind speed reaches to 8.8 m/s, the maximum acoustic power value of rectangular tip is 139dB and tapered tip is 138dB. It is obvious that tapered tip has a better performance for noise reduction than rectangular tip, especially under a low wind speed condition.

Thus, increasing the wind speed, the noise generation of those two tips are almost the same.

4.7 Results summary
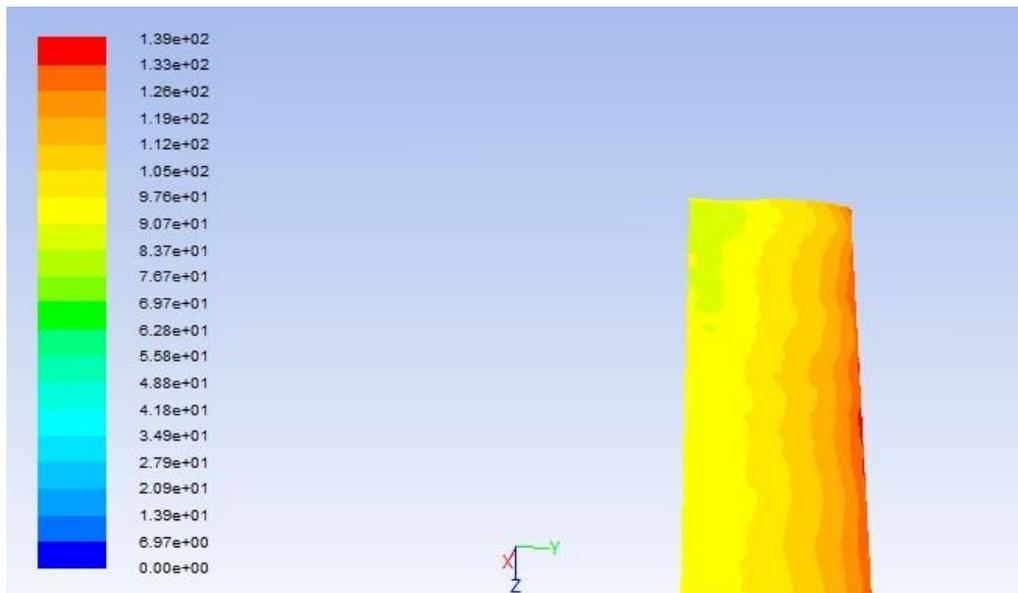
In two-dimensional aerofoil modelling, the comparison between the CFD results and experimental data shows ANSYS-Fluent is a reliable benchmark. Aerodynamic performances of different aerofoils have been compared. The simulated results demonstrate that the DU93 aerofoil has a better aerodynamic performance than the S809 aerofoil. In three-dimensional wind turbine modelling, the innovated root design gives a significant power output increase and tapered tip design has a better ability for noise reduction. Moreover, ANSYS-Fluent provides a better correlation with theoretical data for power output prediction. Based on its greater ability, simulations can be run under a wider range of wind speeds. According to the different wind speeds, an optimum rotational speed can be achieved to maintain the constant power output at high wind speed.

Chapter 5   Conclusion and future work

Based on the research work, the aims and objections of the research project have been achieved. The significant findings are summarized below.

5.1 Conclusions

- ANSYS-Fluent shows a good performance in calculating the lift, drag and moment coefficients of aerofoils when compare to the experimental data. Especially for low angles of attack. So this software has a good ability to predict the optimum and critical angle of attack.

- Using the second order SST k-ω turbulent model, ANSYS-Fluent shows a good agreement with the measured data for a variety of wind speeds (from 4 m/s to 8.8 m/s). According to the reliable results, the wind turbine power output can be predicted under a wider wind speeds range (from 3.5 m/s to 18 m/s). Therefore, when the wind speed increases, the optimum rotational speed can be estimated to maintain the constant power output. In ANSYS-Fluent, not only the torque magnitudes but also the thrusts can be calculated, but the accuracy is unknown as the lack of theoretical data of thrust.

- Wind turbine rotational effect can be simulated by using sliding mesh approach and the wake can be shown once the wind turbine rotates. The velocity drop and wake length have not been predicted precisely in the work, because the mesh gets coarser when it approaches towards the boundaries. The mesh density is difficult to control by using unstructured grid; at the same time, because the blade is twisted and chord length of the blade is varied along the wingspan, it is extremely difficult to mesh the wind turbine by using structured grid in GAMBIT.

- Near- to far- field aerodynamic noise can be simulated by using LES approach, this turbulent model gives a better physical representation of the eddy dynamics than RANS (Carcangiu, 2008, p.31). Due to the high requirement of mesh, LES methods need a longer time than RANS to run the simulation of this work.

5.2 Future work

- For aerofoil simulation, boundary layer should be refined at some angle of attack so that the accuracy of simulations can be improved. Moreover, it is worthwhile to try to use laminar and turbulent mixer model to see whether the accuracy of drag coefficient could be enhanced. Walter P. Wolfe and Stuart S. Ochs (1997) stated that this method highly depends on engineer's ability to accurately guess the transition location.

- The wake effect has been simulated previously. For the next step, two wind turbines can be mounted in a row to observe how the front wind turbine wake influences the downstream wind turbine and the difference of power output between two turbines can be calculated. Meanwhile, in order to create a real operation condition, the tower should be taken into account.

- Turbulent models have been shown to play an important role in CFD modelling of wind turbines. The next step; in order to simulate the wind turbine wake, a high performance computer should be employed to implement the DES and LES techniques.

- Total thrust acting on the blade can be calculated using ANSYS-Fluent, Using ANSYS 12.0 Workbench, the simulated result can be imported into the static structural analysis. Hence, the flap wise bending moment could be calculated.

References

Alexandros Makridis and John Chick, 2009, CFD Modeling of the wake interactions of two wind turbines on a Gaussian Hill, EACEW 5 Florence, Italy. 19th-23rd July 2009

Carlo Enrico Carcangiu, 2008, 'wind turbine functioning and aerodynamics', *CFD-RANS Study of Horizontal Axis Wind Turbines*, Italy

Chalothorn Thumthae and Tawit Chitsomboon. Optimal angle of attack for untwisted blade wind turbine. Renewable Energy, Volume 34, Issue 5, May 2009, Pages 1279-1284

Chalothorn Thumthae and Tawit Chitsomboon. Optimal Pitch for Untwisted Blade Horizontal Axis Wind Turbine. In: SEE (Sustainable Energy and Environment) 2006, The 2nd Joint International Conference. Bangkok, Thailand. 21-23 November 2006.

Chuichi Arakawa, Oliver Fleig, Makoto Iida and Masakazu Shimooka. Numerical Approach for Noise Reduction of Wind Turbine Tip with Earth Simulator, Journal of the Earth Simulator, Volume 2, March 2005, 11-33, pages 11-33

C.K Cheung and W.H Melbourne. Wind Tunnel Blockage Effects on a Circular Cylinder in Turbulent Flows. In: 7th Australasian Hydraulics and Fluid Mechanics Conference. Brisbane, Australia. 18-22 August 1980.

Deepark Sahini, B. Tech, 2004, Wind Tunnel Blockage Corrections, Texas Tech University, USA

Danmei Hu, Ouyand Hua, Zhaohui Du.,* 2005. A study on stall-delay for horizontal axis wind turbine. Renewable Energy. Volume 31, issue 6, pp. 821-836.

Dnynesh A. Digraskar, Simulation of flow over wind turbines, University of Massachusetts Amherst, 2010

Duque, EP et, al. (2000) Numerical prediction of wind turbine power and aerodynamic loads for the NREL PHASE II combined experiment rotor, *ALAA Paper No. 2000-0038*

Erich Hau, 2006 *Wind Turbines Fundamentals Technologies, Application, Economics,* German, Springer

Fluent Inc, 2006, '10. Modeling Flows with Rotating Reference Frame" *FLUENT 6.3 User's Guide* Fluent Inc.

Fluent Inc, 2006, '11. Modeling Flows Using Sliding and Deforming Meshes" *FLUENT 6.3 User's Guide* Fluent Inc.

Fluent Inc, 2006, "12.3.2 Transport Equation for the Spalart-Allmaras Models Theory" *FLUENT 6.3 User's Guide* Fluent Inc.

Fluent Inc, 2006, "12.4 Standard, RNG and Realizable k-ϵ Models Theory" *FLUENT 6.3 User's Guide* Fluent Inc.

Fluent Inc, 2006, "12.5 Standard and SST k-ω Models Theory" *FLUENT 6.3 User's Guide* Fluent Inc.

Fluent Inc, 2006, "12.7 Reynolds Stress Model (RSM) Theory" *FLUENT 6.3 User's Guide* Fluent Inc.

Fluent Inc, 2006, "21 Predicting Aerodynamically Generated Noise" *FLUENT 6.3 User's Guide* Fluent Inc.

Fluent Inc, 2006, "Modelling Flow-Induced (Aeroacoustic) Noise Problems Using Fluent

F. Massouh and I. Dobrev, 2007, Exploration of the vortex wake behind of wind turbine rotor, In: The Second Conference on Science of Making Torque from Wind, Denmark, 28-31 August 2007.

Golding, E.W.: The Generation of Electricity by Wind Power, E.&F.N Spon Ltd. New York, 1977

J.F. Manwell, J.G. McGowan & A.L. Rogers, 2002, 'Aerodynamics of Wind Turbine', *Wind Energy Explained-Theory Design and Application*, John Wiley & Sons Ltd, London

J.M. Jonkman,. 2003. Modeling of the UAE Wind Turbine for Refinement of FAST_AD. USA: DIANE publishing.

L. J. Vermeer, J. N. Sørensen, A. Crespo, 2003, Wind turbine wake aerodynamics, *Progress in Aerospace Sciences*, Volume 39, Issues 6-7, pp. 177-189

Maalawi KY, Badawy MTS. A direct method for evaluating performance of horizontal axis wind turbine. Renew Sustain Energy Rev 2001;5:175-90

Martin Méchali[1][*], Rebecca Barthelmie[2], Sten Frandsen[2], Leo Jensen[2], Pierre-Elouan Réthoré[2], 2004, Wake effects at Horns Rev and their influence on energy production,

Martin O.L. Hansen, 2008, 'Chapter 2 2-D Aerodynamics', *Aerodynamics of wind turbine Second Edition,* Earthscan, UK and USA.

Natalino Mandas, Fransesco Cambuli and Carlo Enrico Carcangiu, 2009, Numerical Prediction of Horizontal Axis Wind Turbine Flow, Italy.

P. Giguère and M.S. Selig,. 1999. Design of a Tapered and Twisted Blade for the NREL Combined Experiment Rotor. USA: National Renewable Energy Laboratory.

R. Lanzafame, M. Messina,. Fluid dynamics wind turbine design: Critical analysis, optimization and application of BEM theory. Renewable Energy, Volume 32, Issue 14, November 2007, Pages 2291-2305.

Rohden R. Revolutionary blade design. *Wind Blatt, The Enercon Magazine*, 03,2004

Sorensen N.N, Johansen J and Conway S, 2004, CFD computations of wind turbine blade loads during standstill operation, KNOW–BLADE Task 3.1, Technical Report R-1465, Riso National Laboratory Roskilde – DK

Tony Burton, David Sharpe, Nick Kenkins and Ervin Bossanyi,. 2001 *Wind Energy Handbook*. Chichester: John Wiley & Sons Ltd.

Varol A, Ilkilic C, Varol Y,. Increasing the efficiency of wind Turbine. J Wind Eng Ind Aerodyn 2001; 89:809-15

Vaughn Nelson,. 2009. Wind Energy: Renewable Energy and the Environment. New York: CRC Press.

Walter P. Wolfe and Stuart S. Ochs. CFD calculations of S809 aerodynamic characteristics, 16. American Society of Mechanical Engineers wind energy symposium, Reno, NV (United States). Jan 01 1997.

World Energy Report 2009. World Wind Energy Association. 9th World Wind Energy Conference & Exhibition Large-Scale Integration of Wind Power. March 2010.